Elise Eknes

Solid Solution Engineering of Hybrid Supramolecular Tetraethylammonium and Tetrabutylammonium Compounds

Master's thesis

NTNU
Norwegian University of Science and Technology
Faculty of Natural Sciences
Department of Materials Science and Engineering

NTNU
Kunnskap for en bedre verden

Elise Eknes

Solid Solution Engineering of Hybrid Supramolecular Tetraethylammonium and Tetrabutylammonium Compounds

Master's thesis in Industrial Chemistry and Biotechnology
Supervisor: Prof. Mari-Ann Einarsrud
Co-supervisor: Assoc. Prof. Julian Walker
July 2022

Norwegian University of Science and Technology
Faculty of Natural Sciences
Department of Materials Science and Engineering

NTNU
Norwegian University of
Science and Technology

Preface

This master's thesis is written as a part of *TMT4900 Material Science and Engineering, Master's Thesis* during the spring semester of 2022 at the Norwegian University of Science and Technology (NTNU), and is a continuation of the work conducted in relation to *TMT4500 Material Science and Engineering, Specialization Project* [1]. Experimental work is performed by Elise Eknes, under the supervision of Prof. Mari-Ann Einarsrud and Assoc. Prof. Julian Walker.

Acknowledgements

Abstract

Plastic crystals are supramolecular materials that undergo a phase transition to a mesophase with increasing temperatures, where the molecules or ions have short-range orientational disorder and long-range positional order. This transition is often accompanied by a large change in the enthalpy and entropy, meaning most plastic crystals have a large potential to store thermal energy in thermal energy storage systems. Such systems show great promise in preventing loss of excess heat to the environment, thereby increasing the energy efficiency of households and renewable technologies significantly. Tetraethylammonium and tetrabutylammonium bromotrichloroferrate(III) are both hybrid plastic crystals, that are comprised of different cations and the same anion, and go through this high entropy mesophase transition. By creating a solid solution between these two plastic crystals, the thermal properties can be adjusted by changing the cation. As a result, properties such as the phase transition temperature and enthalpy can be tuned to create thermal energy storage systems specified for a wide variety of applications. In this study, tetraethylammonium and tetrabutylammonium bromotrichloroferrate(III) were synthesised using a water-based evaporation crystallisation. Further, solid solution engineering between the two end member materials was utilized to create $TEA_xTBA_{1-x}FeBrCl_3$ materials. X-ray diffraction and differential scanning calorimetry were used to analyse how the crystal structure, phase transition temperature, enthalpy, and entropy change as a function of composition. Tetraethylammonium and tetrabutylammonium bromotrichloroferrate were synthesised with a yield of 96.4% and 87.6%, respectively. Materials of $TEA_xTBA_{1-x}FeBrCl_3$ with x = 0.05, 0.1, 0.15, 0.25, 0.50, and 0.75, were synthesised through an annealing process where stoichiometric mixtures of powders were heated to 240 °C. From X-ray diffraction measurements and Rietveld refinement, it was found that no clear solid solution formation occurs between the two end member materials at room temperature, as the presence of both $P6_3mc$ and $Pnna$ phases are observed in all compounds. However, the construction of an approximate phase diagram for the system using differential scanning calorimetry, show a miscible mesophase region at elevated temperatures for samples containing 5-15 mol% tetraethylammonium bromotrichloroferrate(III). For samples containing more than 25 mol% tetraethylammonium bromotrichloroferrate(III), on the other hand, one of the phases melts around 105 °C, creating a phase separation between the liquid and solid phase.

Sammendrag

Plastiske krystaller er supramolekylære materialer som gjennomgår en fasetransformasjon til en mesofase ved forhøyede temperaturer. I mesofasen har molekylene eller ionene rotasjonell frihet samtidig som de er begrenset til krystallgitteret. Denne fasetransformasjonen er som regel fulgt av en stor entalpi- og entropiendring, som betyr at mange plastiske krystaller har potensialet til å lagre store mengder termisk energi i systemer for termisk energilagring. Slike systemer kan forhindre tap av varme til omgivelsene og dermed øke energieffektiviteten til husholdninger og fornybare energiteknologier betraktelig. Tetraetylammonium og tetrabutylammonium bromotrikloroferrat(III) er hybride plastiske krystaller som går gjennom en fasetransformasjon til denne mesofasen. De består av ulike kationer, men samme anion. Ved å lage en fast løsning mellom disse to plastiske krystallene vil kationet endres, noe som kan føre til endringer i de termiske egenskapene. Dermed kan for eksempel fasetransformasjonstemperaturen og entropien endres for å skape termisk energilagringsystemer for mange ulike anvendelser. I denne studien ble tetraetylammonium og tetrabutylammonium bromotrikloroferrat(III) syntetisert med en vann-basert syntesemetode. Videre ble det forsøkt å lage en fast løsning mellom disse to forbindelsene for å syntetisere materialer av $TEA_xTBA_{1-x}FeBrCl_3$. Røntgendiffraksjon og differensiell skanningskalorimetri ble deretter benyttet for å analysere hvordan krystallstrukturen, fasetransformasjonstemperaturen, entalpien og entropien endres som en funksjon av komposisjon. Tetraetylammonium og tetrabutylammonium bromotrikloroferrat(III) ble syntetisert med et utbytte på henholdsvis 96.4% og 87.6%. Materialer av $TEA_xTBA_{1-x}FeBrCl_3$, med x = 0.05, 0.1, 0.15, 0.25, 0.50 og 0.75, ble syntetisert ved å varmebehandle støkiometriske blandinger av pulvere på 240 °C. Resultatene fra røntgendiffraksjonen viste at både *P6₃mc*- og *Pnna*-fasen er tilstede i alle materialene, og man kan konkludere med at det ikke dannes noen fast løsning mellom tetraetylammonium og tetrabutylammonium bromotrikloroferrat(III) ved romtemperatur. Et tilnærmet fasediagram for systemet ble konstruert med resultater fra differensiell skanningskalorimetri. Dette fasediagrammet viser at det derimot finnes en fast løsning i mesofasen ved forhøyede temperaturer for materialer som inneholder 5-15 mol% tetraetylammonium bromotrikloroferrat(III). For materialer som inneholder mer enn 25 mol% tetraetylammonium bromotrikloroferrat(III), smelter en av fasene rundt 105 °C. Dette fører til en faseseparasjon mellom den dannede væskefasen og den faste fasen.

Abbreviations

TES	Thermal energy storage
PC	Plastic crystal
$TEAFeBrCl_3$	Tetraethylammonium bromotrichloroferrate(III)
$TBAFeBrCl_3$	Tetrabutylammonium bromotrichloroferrate(III)
$TEA_xTBA_{1-x}FeBrCl_3$	Tetraethylammonium tetrabutylammonium bromotrichloroferrate(III)
TEA^+	Tetraethylammonium cation
TBA^+	Tetrabutylammonium cation
DSC	Differential scanning calorimetry
XRD	X-ray diffraction
CIF	Crystallographic information file
DTA	Differential thermal analysis
TG	Thermogravimetric
COD	Crystallographic open database
DI water	Deionized water
$TMA_xTEA_{1-x}FeBrCl_3$	Tetramethylammonium tetraethylammonium bromotrichloroferrate(III)
GOF	Goodness of fit
FWHM	Full width half maximum
SNBL	Swiss Norwegian Beam Lines
ESRF	European Synchrotron Radiation Facility

Table of Contents

1 Background

1.1 Motivation

Global warming is an immense challenge that today's society is facing, where CO_2 emissions from everyday technologies are contributing to the problem. According to the International Energy Agency, heating and cooling technologies account for more than 50% of today's CO_2 emissions globally, meaning there is a huge potential for increasing the sustainability of these technologies [2–4]. Over the years, heating systems have become more sustainable as renewable energy sources, such as solar, wind, and hydro, have gradually substituted fossil fuels. However, many technologies, including renewable energy technologies, produce excess heat at times where energy consumption is low, resulting in loss of valuable heat to the environment. If this excess heat can be captured and stored until needed, energy shortages can be reduced or prevented, and the energy efficiency of many households and technologies will increase significantly [2, 5, 6]. Thermal energy storage (TES) systems, where thermal energy is stored in a medium for later use, may be one solution to the challenges of energy loss and energy shortages [2, 7].

TES systems use materials that can absorb large amounts of latent heat and then release it at a later time, when the ambient temperature has decreased and the heat is needed. Consequently, TES systems can regulate the surrounding temperature. For example, heat provided from solar energy during the day can be stored in a TES system, and then released in the evening when the sun goes down, effectively making use of what would otherwise be excess heat, as shown in Figure 1.1 [2, 8]. To create such a TES system, materials that go through reversible endothermic phase transitions on heating within desired temperature ranges [2, 8], that are accompanied by a large entropy change and a temperature hysteresis on heating and cooling, are needed [2, 6, 9, 10]. The material will absorb latent heat during the endothermic reaction, and release the latent heat during the reversible exothermic reaction when the temperature is decreased [11]. Latent heat TES is a mechanism within TES that utilizes this [2, 8].
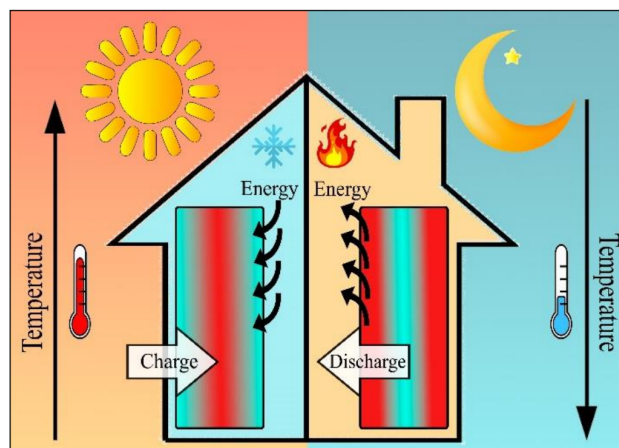
Figure 1.1: A domestic solar thermal energy storage system proposed by Beceiro [2]. Solar energy increases the TES material's temperature. Once the temperature reaches above the phase transition temperature, the material goes through a phase transition, and becomes charged with thermal energy. The surroundings cool down. Once the temperature decreases during the night, the material goes through the reverse phase transition, and discharge the stored energy. The surroundings heat up.

Hybrid plastic crystals (PCs) are comprised of molecular organic cations and inorganic anions. They fulfil the requirements for latent heat TES systems, making them an interesting group of materials for this application. PCs undergo a phase transition to a mesophase with increasing temperatures, where the molecules or ions have orientational disorder and positional order in the crystal lattice [12]. Due to the increased orientational disorder in the mesophase, mesophase transitions are usually accompanied by a large change in the enthalpy and entropy [12–14]. Thus, these materials have the potential to store large amounts of thermal energy, and are highly suitable for latent heat TES systems [2, 9]. Hybrid PCs have low processing temperatures [13] and are easily soluble in aqueous solutions [15], which can contribute to low production costs and easy recycling. This is beneficial for commercial use.

Tetraethylammonium and tetrabutylammonium bromotrichloroferrate(III), TEAFeBrCl$_3$ and TBAFeBrCl$_3$ respectively, are both hybrid PCs [16, 17]. Both compounds go through a mesophase transition at a temperature less than 200 °C, that is accompanied by a large enthalpy and entropy change, and a thermal hysteresis between heating and cooling [18, 19]. They therefore show promise as TES materials in medium temperature ranges, that is, from about 100 to 200 °C [2]. The inorganic anion in both compounds, which contains the Fe^{3+} transition metal, can increase the thermal stability of the compound. Additionally, functional properties such as piezoelectric and/or ferroelectric properties, can stem from the inorganic anion [2, 12, 13]. The organic cation, however, contributes to increased flexibility and response to different stimuli, such as temperature [2]. The organic molecule or ion in hybrid PCs include carbon and hydrogen atoms, which makes it possible to tune, for instance, the size, morphology, and symmetry of the PCs by changing the number of these atoms. As no new elements from the periodic table are added to tune the properties, the tuning is more sustainable compared to adding additional elements that may be limited resources, not environmentally friendly, or make recycling more difficult [20].

1.2   Aim

The aim of this master's thesis was to first synthesise hybrid organic-inorganic plastic crystals of tetraethylammonium and tetrabutylammonium bromotrichloroferrate(III) using a water-based evaporation crystallisation. Further, the aim was to utilize solid solution engineering between the two end members to obtain an understanding of the relationship between the composition of the TEA$_x$TBA$_{1-x}$FeBrCl$_3$ system, crystal structure, and thermodynamic properties. Previous studies [16–19, 21] have reported synthesis methods, structural data, and thermal properties of both end members. However, no research has been published on the solid solution formation between the two compounds.

To achieve the aim, compositions of the TEA$_x$TBA$_{1-x}$FeBrCl$_3$ system with x = 0, 0.05, 0.1, 0.15, 0.25, 0.5, 0.75, and 1 were synthesised to get an overview of the entire composition range. As the tetraethylammonium cation (TEA$^+$) is smaller than the tetrabutylammonium cation (TBA$^+$), it was hypothesised that TEA$^+$ was more likely to be soluble in the TBAFeBrCl$_3$-rich crystal structure. Thus, more compositions in the TBAFeBrCl$_3$-rich region of the solid solution system were synthesised. To assess if a solid solution engineering approach could be used to modify the entropy and phase transition temperature, differential scanning calorimetry (DSC) was used to analyse the compounds. This was coupled with a structural analysis using X-ray diffraction (XRD) to understand the structural origin of any observed changes.

2 Introduction

2.1 Crystallisation

The synthesis of the materials in this project involved the precipitation of supramolecular crystals from solutions. A brief introduction to the crystallisation from solutions is therefore necessary to understand the synthesis process used.

A crystalline solid has a high internal degree of regularity, meaning the long-range crystal structure can be represented by the unit cell. The unit cell holds all the symmetry elements of the crystal structure, and is the smallest repeating structural unit with translational symmetry. This long-range order results in a reduction of the free energy of the system by reducing the entropy [22–25]. The crystallisation process is a first order phase transition where atoms, molecules, or ions are transformed from a high free energy disordered state to a low free energy ordered state [22, 23, 25]. The driving force for the crystallisation is this reduction in the free energy [23].

For the crystallisation process to occur from a solution, the solution has to be supersaturated, meaning it is in a non-equilibrium state with the solid phase [23, 26]. Supersaturation can be achieved by decreasing the temperature of the solution, or by increasing the solution concentration above the solubility limit of the crystalline product, which can be achieved through evaporating the solvent [26]. Once supersaturation is reached, the system enters the metastable zone in Figure 2.1, where crystallisation is possible [23, 26].
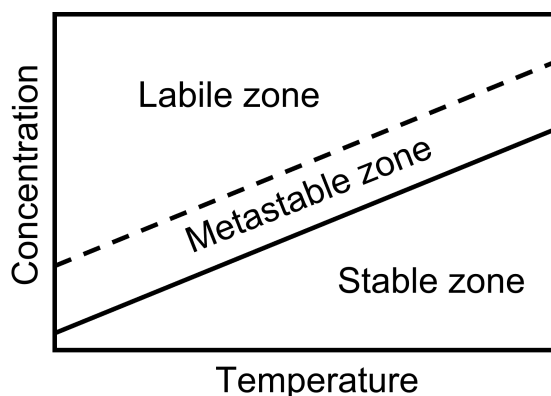
Figure 2.1: Solubility diagram showing the relationship between concentration, supersaturation, and temperature. The solubility curve is illustrated with a solid line, and the supersolubility curve with a dashed line. Stable, metastable, and labile zones are marked. The figure is obtained from Eknes [1], and was adapted from Bandyopadhyay [23].

The crystallisation process is divided into two steps, nucleation and growth, and the relationship between the two steps is illustrated in Figure 2.2 [27, 28]. During nucleation, the new crystal phase appears in the solution. When the supersaturation of the solution reaches a critical value, ions, atoms, or molecules are able to come together to form nuclei. Once the nuclei reach a critical size where they overcome the free energy barrier for nucleation, a reduction in the free energy occurs, and a stable crystal phase appears. The supersaturation is reduced, and consequent growth of nuclei becomes possible [23, 27–30]. When equilibrium conditions are reached, the growth process comes to an end [27, 28].

Figure 2.2: LaMer diagram showing the relationship between nucleation and growth. Prenucleation (I), nucleation (II) and growth (III) regions are shown. The critical value for nucleation, a_c, and the equilibrium conditions, a^*, are noted. The figure is obtained from Eknes [1], and was adapted from Bandyopadhyay [27].

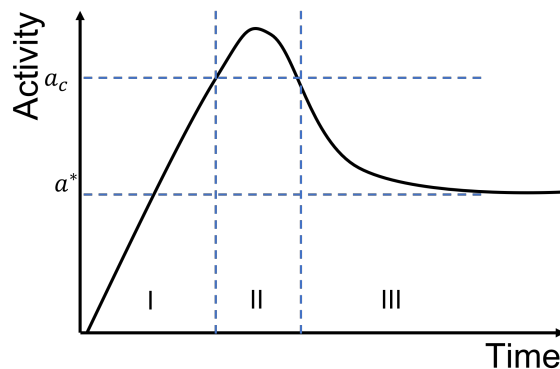The final crystal morphology and size depends on intrinsic factors, such as the crystal lattice, and external factors, such as supersaturation. The final morphology is the most thermodynamically stable one, meaning the one with the lowest surface energy [27, 31]. The driving force for both nucleation and growth is to lower the chemical potential of the system. Therefore, both stages of crystallisation depend on the degree of supersaturation [27, 28]. Multiple smaller and uniform crystals will result from a high nucleation rate, as the supersaturation will mainly contribute to the nucleation stage. Fewer larger crystals will result at a lower nucleation rate, as more supersaturation will contribute to the growth stage. The higher the degree of supersaturation, the higher the nucleation rate, and thereby the lower the growth rate [23]. As the degree of supersaturation varies, the growth mechanism changes. When the degree of supersaturation is increased, the resulting crystals change from monocrystalline with smooth faces to more polycrystalline crystals with rough surfaces [27].

2.2 Solid state reactions

A solid state reaction process was utilised to investigate the solid solubility in supramolecular crystals synthesised in this study. Solid state reactions involve the reaction of two or more chemical species that are in their solid state. For these reactions to occur, sufficient energy is needed to allow for mass transport, which is the solid state diffusion of atoms, ions, or molecules through the bulk or along the surface of the materials [32–34]. The driving force for this mass transport is usually a concentration gradient, which is described by Fick's first law for steady-state diffusion when the gradient is constant, and by Fick's second law for non-steady-state diffusion when the gradient changes over time [35, 36]. As the mass transport requires energy, these reactions are temperature dependent. The temperature dependence varies between materials and is described by the material specific diffusion coefficient [35]. How the diffusion coefficient varies with temperature is expressed with the Arrhenius equation, where the diffusion coefficient increases with increasing temperatures [35]. Consequently, solid state reactions are often performed by heating the reactants in an oven over a longer time period. Additionally, the chemical species need to be in close contact to react, so sufficient mixing and dispersion of the solids are necessary to achieve the desired solid state reaction [32–34].

2.3 Solid solutions

Solid solution formation is a proven approach in crystal chemistry for modifying key properties of material systems. Many physiochemical properties depend on the composition and structure of the material. Consequently, properties such as the phase transition temperature, enthalpy, and entropy can be tuned through solid solution engineering [37–39]. Hence, solid solution formation was the chosen approach for engineering the plastic crystal materials of this study.

A solid solution is a homogeneous crystalline phase containing at least two chemical compounds [40]. As substituent atoms, ions, or molecules are introduced in the crystalline phase, extrinsic defects are formed, where the substituents can occupy interstitial sites, or substitute atoms or ions in the crystal lattice. When the substituent concentration exceeds 0.1-1%, the material is called a solid solution rather than a doped material [37]. These substituents are dispersed randomly and uniformly in the crystalline solid [40]. Two main types of solid solutions exist, called substitutional and interstitial solid solutions [37, 40, 41]. In substitutional solid solutions the introduced substituents replace atoms or ions in the crystal lattice, and in interstitial solid solutions the introduced substituents occupy sites in the crystal lattice that are normally unoccupied [37, 41]. For a substitutional solid solution to form, the substituents should have similar size and charge as the atoms or ions in the host material. If the charge is different, other structural changes such as vacancies and interstitials are needed to maintain electroneutrality. A rule of thumb is that when the size difference between the atoms or ions is more than ∼30%, no substitutional solid solutions are expected to form [37]. However, this relationship is not well known for supramolecular compounds.

The solid solution can have a complete or partial range, with a partial range being the most common, as the two end member materials need to have the same crystal structure to form complete ranges. For partial ranges of solid solutions, only a limited concentration of the added substituents are soluble in the host material. When the solubility limit of the substituents in the host material is reached, phase separation will occur in the system, resulting in different crystallographic phases with different chemical compositions [37, 42].

2.4 Plastic crystals

Plastic crystals are supramolecular materials, which consist of molecular assemblies that are held together by weaker, non-covalent interactions, such as van der Waals forces or weaker ionic interactions [43]. At elevated temperatures these materials go through one or multiple, usually reversible, order-disorder solid-solid phase transition from an ordered crystal to a plastic crystal phase, called the mesophase. In the mesophase, the molecules have rotational freedom while long-range positional order is intact, resulting in a phase with characteristics from both a liquid and a crystalline solid. When the PCs are further heated to the melting temperature, they undergo a phase transition to a liquid phase. As the PCs in the mesophase have already obtained a high degree of freedom due to the orientational disorder, the mesophase transition is often accompanied by a larger entropy change than the entropy of fusion. Most of the thermal energy is therefore contributing to rotation of the molecules instead of breaking up the crystal lattice, resulting in high melting points for most PCs [12–14]. The phase transitions are illustrated in Figure 2.3.
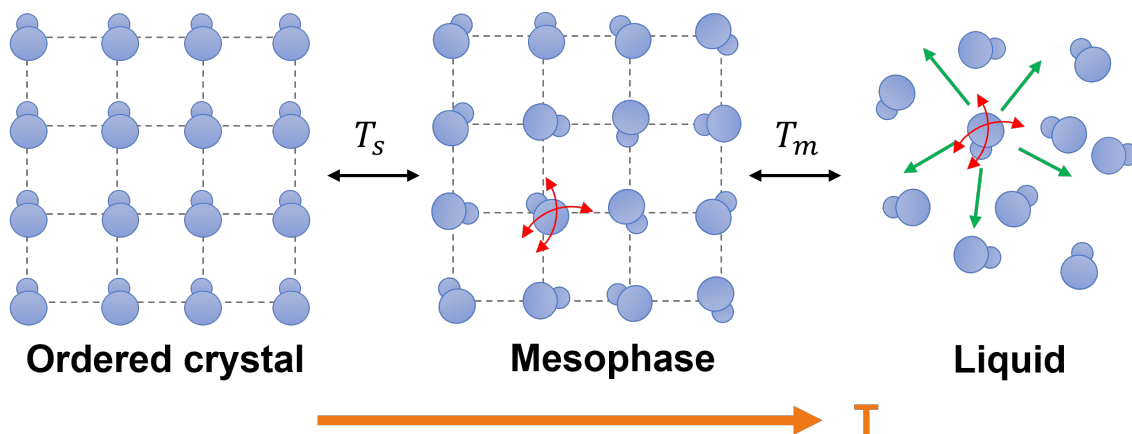
Figure 2.3: Plastic crystals go through a phase transition from an ordered crystal to a plastic crystal phase, called the mesophase, at increasing temperatures, T. When the melting temperature, T_m, is reached, the plastic crystals transition from the mesophase to a liquid. Molecules or ions are shown as blue figures, orientational disorder is indicated by the red arrows, translational movement is noted by green arrows, and the crystal lattice is shown with grey, dashed lines. The figure is obtained from Eknes [1], and was adapted from Das et al. [13].

The combination of mechanical plasticity and long-range order that PCs exhibit in the mesophase is rare in molecular materials, as they are usually brittle. This plasticity stems from the molecules occupying larger volumes when rotating, resulting in weaker intermolecular interactions and slip planes [12, 13]. Consequently, PCs are more easily formed into a wide variety of structures, such as thin films, compared to other crystalline materials [13]. The molecular assemblies PCs comprise of can have different geometries and chemical nature [13]. They are often globular, meaning they are either symmetrical around their centre or form a sphere when rotating [13, 14]. PCs are neutral as a whole, but the molecular assemblies can for example be ions, creating what is called ionic PCs [13]. Hybrid PCs comprise of an organic cation and an inorganic anion, thus belonging to the group of ionic PCs [12, 13]. The inorganic anion can contribute to increased thermal stability and functional properties, [2, 12, 13], and the organic cation can increase the flexibility and sensitivity to stimuli [2]. This combination of functional properties and increased sensitivity to stimuli opens up for use of hybrid PCs in multiple applications. They show promise as thermal energy storage materials, in cooling systems, as capacitors, in mechanical sensors, and as solid electrolytes, to mention a few [2, 12, 13].

2.5 The TEAFeBrCl$_3$ and TBAFeBrCl$_3$ systems

The system of tetraethylammonium and tetrabutylammonium bromotrichloroferrate(III), TEA$_x$TBA$_{1-x}$FeBrCl$_3$, was investigated. The cations and anion the two end member materials are comprised of, are illustrated in Figure 2.4. Both TEA$^+$ and TBA$^+$ are quaternary ammonium cations [44] that consist of the same atoms, meaning the difference between TEAFeBrCl$_3$ and TBAFeBrCl$_3$ is the length of the cation carbon chain. Thus, modifications of the composition of the TEA$_x$TBA$_{1-x}$FeBrCl$_3$ system can be achieved without adding additional elements from the periodic table. TEAFeBrCl$_3$ was chosen as the first end member as it fulfils the requirements for TES materials [9, 18]. The thermal stability of TBAFeBrCl$_3$ should be a little lower than for TEAFeBrCl$_3$, as thermal stability

decreases with the length of the carbon chain [45]. Thus, TBAFeBrCl$_3$ was chosen as the second end member, as a lowering of the mesophase transition temperature of TEAFeBrCl$_3$ is expected when combined with TBAFeBrCl$_3$.
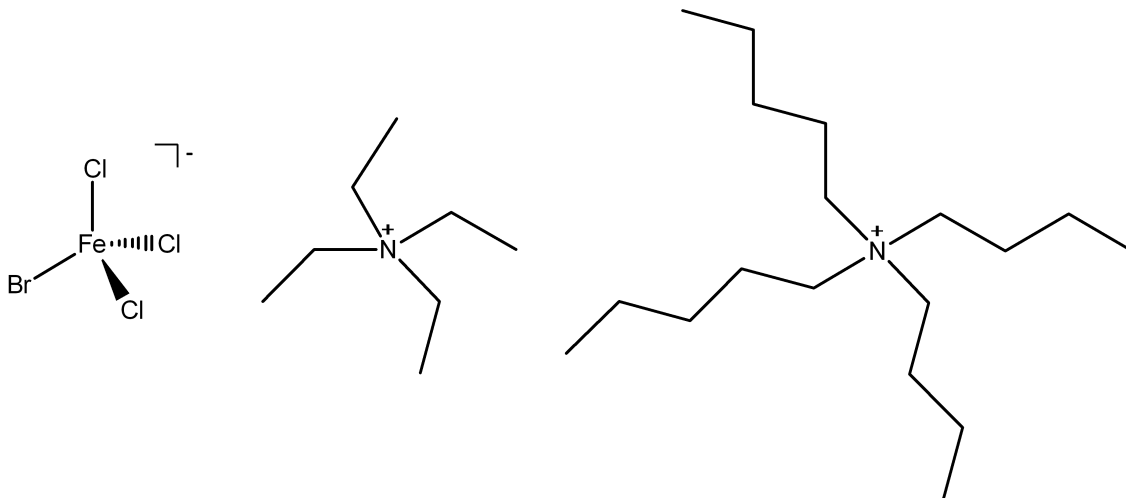

Figure 2.4: Schematic of the bromotrichloroferrate(III) anion (FeBrCl$_3^-$), tetraethylammonium cation (TEA$^+$), and tetrabutylammonium cation (TBA$^+$), that TEAFeBrCl$_3$ and TBAFeBrCl$_3$ are built up of. Adapted from Kruszynski et al. [17].

2.5.1 Tetraethylammonium bromotrichloroferrate(III)

Tetraethylammonium bromotrichloroferrate(III), $[(C_2H_5)_4N][FeBrCl_3]$, belongs to the group of organic-inorganic ionic plastic crystals, and is built up of the organic tetraethylammonium cation and the inorganic bromotrichloroferrate(III) anion [16]. At room temperature, this compound exhibits the hexagonal wurtzite-like structure [46] with the $P6_3mc$ space group (no. 186), shown in Figure 2.5, where a = 8.230 Å and c = 13.242 Å. In the structure, the cation is disordered around a $3m$ symmetry site, while the anion is arranged in an almost ideal tetrahedral coordination due to the Br-atom replacing one Cl-atom, resulting in a slight distortion [16, 17]. When heating the structure to its mesophase, Walker et al. [18] has found that the material acquires a high symmetry crystal structure which is approximated to the cubic $P\bar{4}3m$ symmetry (no. 215). Upon cooling to room temperature, the material returns to the $P6_3mc$ structure [18].
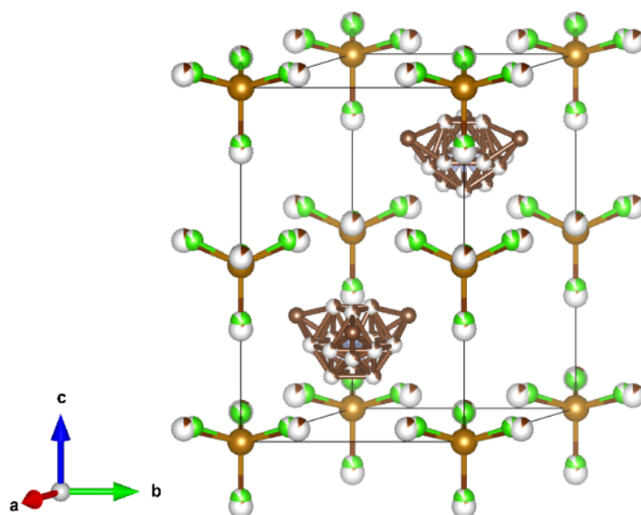
Figure 2.5: The hexagonal *P6₃mc* crystal structure of tetraethylammonium bromotrichloroferrate(III) constructed using structural data (CIF) from Evans et al. [16] and the VESTA software [47].

The thermal properties of TEAFeBrCl$_3$ have been studied by both Wyrzykowski et al. [21] and Walker et al. [18] using DSC, DTA, and TG analysis, resulting in a good understanding of the material's thermal behaviour in the temperature range of -15 to 800 °C. When analysing the compound using DSC between -15 to 200 °C, as shown in Figure 2.6, a phase transition from the solid phase to the mesophase is observed around 149 °C on heating. On cooling, the reverse transition takes place more rapidly around 105 °C, resulting in a hysteresis of 44 °C. Corresponding thermodynamic parameters are given in Table 2.1 [18]. Previous findings by Wyrzykowski et al. [21] support the discovery of a phase transition from the solid phase to the mesophase prior to decomposition. Two endothermic reactions are observed through DTA and TG analysis prior to decomposition of the material, where the first corresponds to a solid-state phase transition and the second to the melting of the material. The thermal data for this study are also given in Table 2.1. Decomposition of TEAFeBrCl$_3$ occurs in two main steps, where the first is rapid and takes place between 295 and 420 °C, and the second is slower and takes place between 420 and 750 °C. Both decomposition step one and two are accompanied by a mass loss, which from TG analysis is found to be 54% and 30% respectively [21].
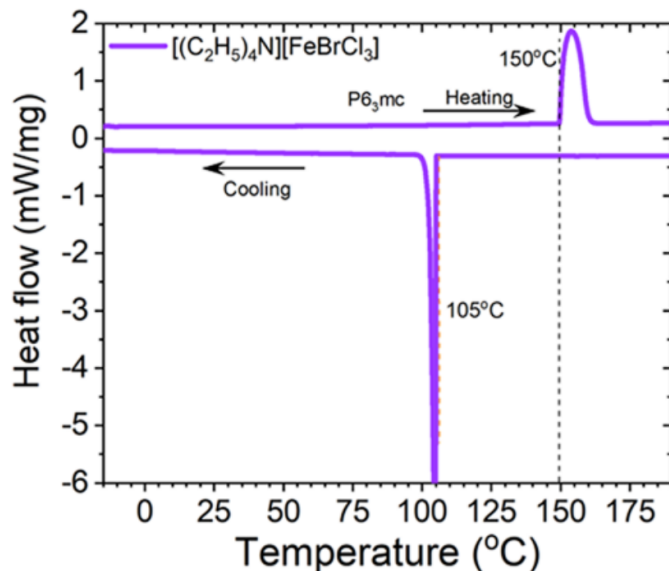
Figure 2.6: The DSC plot between -15 and 190 °C for tetraethylammonium bromotrichloroferrate(III), with the $P6_3mc$ symmetry, from Walker et al. [18]. The heating and cooling directions, and the onset temperatures for the phase transitions are labelled.

Table 2.1: Thermodynamic parameters of tetraethylammonium bromotrichloroferrate-(III). The data are from a DSC analysis in synthetic air by Walker et al.* [18], and from a DTA and TG analysis in argon by Wyrzykowski et al. [21].

Parameter	TEAFeBrCl$_3$
Peak onset, heating [°C]	149*
Heating ΔH [kJ/mol]	24.5*
Heating ΔS [J/Kmol]	62.2*
Heating FWHM [°C]	7.7*
Peak onset, cooling [°C]	105*
Cooling ΔH [kJ/mol]	24.4*
Cooling ΔS [J/Kmol]	64.8*
Cooling FWHM [°C]	1.4*
Solid-state phase transition [°C]	161
Melting point [°C]	281
Decomposition range 1 [°C]	295-420
Decomposition range 2 [°C]	420-750
Mass loss 1 [%]	54
Mass loss 2 [%]	30

2.5.2 Tetrabutylammonium bromotrichloroferrate(III)

Tetrabutylammonium bromotrichloroferrate(III), $[(n-C_4H_9)_4N][FeBrCl_3]$, is an organic-inorganic ionic plastic crystal that consists of an organic tetrabutylammonium cation and an inorganic bromotrichloroferrate(III) anion. At room temperature, the compound crystallises in the orthorhombic crystal structure with the *Pnna* space group (no. 52), where the lattice parameters are a = 18.5191 Å, b = 11.5864 Å, and c = 11.4957 Å [17]. An illustration of the structure is given in Figure 2.7 [48]. From the structure, the N-atom and the four attached n-butylammonium molecules form a slightly distorted

tetrahedron. The cations and anions are alternately packed in the crystal structure [17, 49]. Tetrabutylammonium tetrahalogenoferrates(III), $[(C_4H_9)_4N][FeBr_{4-n}Cl_n]$ (n = 0-4), are isostructural in the solid state [19, 49]. However, the thermal behaviour prior to decomposition is affected by the halogen ligands in the anion, and the structural changes with temperature may vary as a function of Br/Cl content [19].
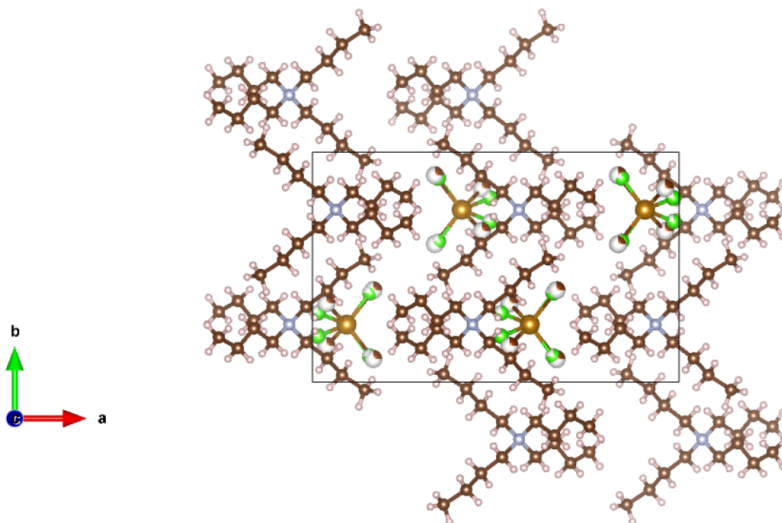

Figure 2.7: The orthorhombic *Pnna* crystal structure of tetrabutylammonium bromotrichloroferrate(III) constructed using structural data (CIF) by Kruszynski et al. [17] from the crystallographic open database (COD) entry 2208805 [48], and the VESTA software [47].

Wyrzykowski et al. [19] has studied the thermal decomposition of TBAFeBrCl$_3$ in argon from 20 to 800 °C, and an overview of the thermal characteristics is given in Table 2.2. When heating the compound and analysing it using DSC and DTA, two endothermic reactions are observed prior to decomposition of the compound. The first reaction occurs around 115 °C and the second reaction occurs around 133 °C, corresponding to a solid-state phase transition to the mesophase and the melting of the compound, respectively. At even higher temperatures, decomposition occurs in two steps, where the first is rapid and takes place between 255 and 410 °C, and the second is slower and takes place between 410 and 750 °C. From TG analysis, the first decomposition step results in a mass loss of 62% and the second step results in a mass loss of 22%. Upon cooling of the material and analysing it using DSC, two exothermic reactions are observed. The first reaction takes place around 109 °C, and is most likely due to supercooling of the compound, as the crystallisation of new nuclei is delayed upon recrystallisation. The second reaction takes place around 71 °C, and may be due to the phase transition from a metastable phase to the more stable crystalline phase. The DSC plot including thermodynamic parameters for the phase transitions is given in Figure 2.8 [19].

Table 2.2: Thermal characteristics of tetrabutylammonium bromotrichloroferrate(III) from Wyrzykowski et al. [19], from DTA, DSC, and TG analysis in argon.

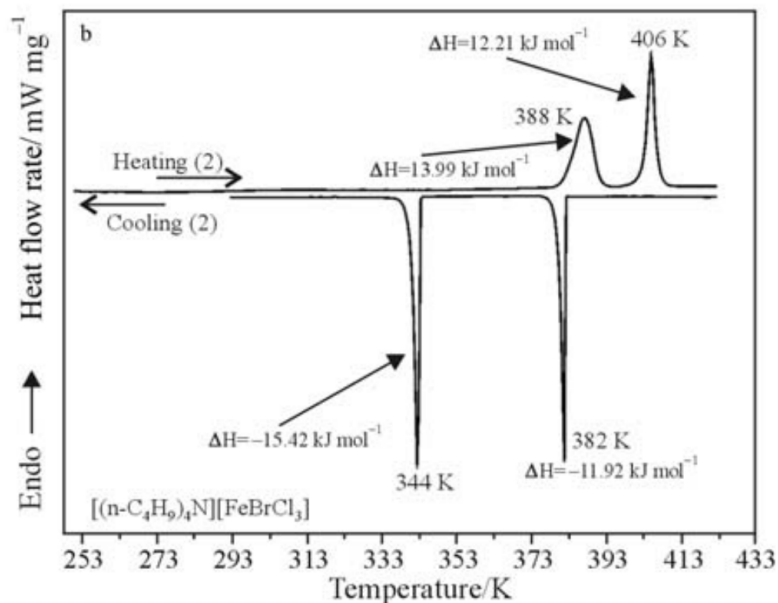| Parameter	TBAFeBrCl$_3$
Solid-state phase transition [°C]	115
Melting point [°C]	133
Decomposition range 1 [°C]	255-410
Decomposition range 2 [°C]	410-750
Mass loss 1 [%]	62
Mass loss 2 [%]	22

Figure 2.8: DSC plot for tetrabutylammonium bromotrichloroferrate(III) with repeated heating and cooling in argon by Wyrzykowski et al. [19]. The enthalpy, ΔH, and the temperature of the phase transitions are labelled.

2.5.3 TEA$_x$TBA$_{1-x}$FeBrCl$_3$ solid solution system

Both TEAFeBrCl$_3$ and TBAFeBrCl$_3$ go through a phase transition to the high entropy mesophase, and show great promise in applications such as TES and cooling systems [2, 6, 13]. The difference in the chain length of the cation result in the compounds having different structures and thermal properties [16–19, 21]. To create compounds with properties that are an average between these two compounds, solid solution engineering can be used. The resulting compound may have more optimized properties for wanted applications compared to the end members alone [39]. As TEAFeBrCl$_3$ and TBAFeBrCl$_3$ are both larger supramolecular materials with different crystal structures, a substitutional solid solution with a partial range is expected to form [37, 42].

2.6 Thermodynamic properties from differential scanning calorimetry

Differential scanning calorimetry is a thermal analysis technique useful for determining thermodynamic changes in materials as a function of temperature, and is therefore a useful tool for studying the $TEA_xTBA_{1-x}FeBrCl_3$ system. DSC works by measuring the difference between the heat flow rate to the sample and to the inert reference sample while both samples are subjected to the same temperature program [50, 51]. This difference in the heat flow rate is normally a consequence of the sample temperature being altered, which often indicates an alteration of the sample [50], for example through a chemical reaction, or a physical change such as vaporisation (liquid-to-gas), sublimation (solid-to-gas) or melting (solid-to-liquid) [51]. For power compensation DSC, the measured heat is compensated with electric energy by adjusting the Joule's heat. When a temperature difference occurs between the sample and the inert reference sample, the heating power is increased or decreased in order to keep the heat flow rate constant between the two samples [52, 53]. As a result, enthalpy changes are measured directly [53], and DSC becomes a helpful tool in studying thermodynamic and thermal properties of small samples in the mg-range. Today, DSCs are used for multiple applications, such as to characterise materials, study phase diagrams, determine sample purity, and to do kinetic investigations [50].

The resulting DSC plot shows the heat flow rate as a function of temperature, and an example is shown in Figure 2.6 for the plastic crystal $TEAFeBrCl_3$ [18]. The heat flow rate can be expressed as

$$\frac{dH}{dt} = C_p \frac{dT}{dt} + f(T,t), \tag{1}$$

where $\frac{dH}{dt}$ is the total heat flow rate, C_p is the heat capacity, $\frac{dT}{dt}$ is the heating rate, and $f(T,t)$ is the heat flow as a function of temperature and time, meaning it is due to kinetic processes such as evaporation and crystallisation. Generally, the heat flow rate can be expressed as the first term in equation (1) when no kinetic processes occur. However, if an exothermic or endothermic process is measured by, for example, a power compensation DSC instrument, the heat flow rate decreases or increases respectively, resulting in peaks in the DSC plot [51, 54]. As an endothermic reaction occurs, which requires energy, the heating power is increased to ensure a constant flow rate between the sample and reference, and a positive peak can be observed in the plot. The opposite is expected for exothermic reactions, that release energy [11]. The heat flow rate of these peaks can be expressed as the second term in equation (1), $f(T,t)$ [51, 54]. From the expression for the heat flow rate (1), the enthalpy of a phase transition can be obtain by integrating both sides with respect to time, and by performing an integration by substitution, the enthalpy can be expressed as a function of temperature

$$\Delta_{trs}H = \int_{t_1}^{t_2} f(T,t)\ dt = \int_{T_1}^{T_2} f(T,t)\ dT \cdot \frac{dt}{dT}\ [\frac{J}{g}]. \tag{2}$$

T_1 is the extrapolated onset temperature and T_2 is the extrapolated end temperature of the phase transition at time t_1 and t_2 respectively. To find these two temperatures, an interpolated baseline between where the temperature first deviates from the baseline and where the temperature reaches the final baseline is conducted. The temperatures can then be found at the intersection between this baseline, and the extrapolated ascending and descending slopes at half the amplitude of the peak [51]. When the enthalpy of the phase

transition and the extrapolated initial peak temperature are known, the entropy of the phase transition can be expressed as [55]

$$\Delta_{\mathrm{trs}}S = \frac{\Delta_{\mathrm{trs}}H}{T_1} \; [\frac{J}{gK}]. \tag{3}$$

When the enthalpy of melting is known, the percentage relative crystallinity of a compound can be calculated from the expression

$$\% \text{ Relative crystallinity} = \frac{\Delta H_m}{\Delta H_m^\circ} \cdot 100, \tag{4}$$

where ΔH_m is the enthalpy of melting for the studied compound, and ΔH_m° is the enthalpy of melting for the 100% crystalline version of the same sample [56].

DSC is useful for studying phase transitions, and is therefore a selected method to determine the phase diagrams of both one- and multi-component systems [51, 53, 57]. From the peaks in the DSC plot, information about the temperature at which phase transitions occur, and the type of reaction can be extracted. An example of how the DSC results can be connected to a binary phase diagram is given in Figure 2.9. For a given composition of the hypothetical alloy in the phase diagram, changes in the material, such as through melting or crystallisation, are indicated by peaks in the corresponding DSC curve [58].
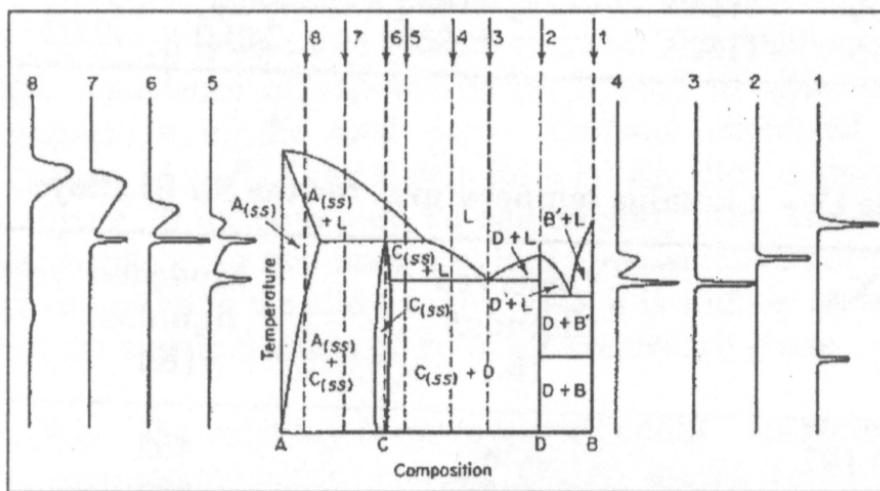

Figure 2.9: A phase diagram of the hypothetical binary system A-B with corresponding DSC curves at various alloy compositions, marked with dashed lines, from Kaye et al. [58] after Gutt and Majumdar.

Reversible or irreversible thermal changes can be determined with DSC. Reversible changes occur both on heating and cooling, while irreversible ones do not. These processes are also influenced by the kinetics of the changes, and can therefore be dependent on the heating rate. Even though a process is reversible, a hysteresis in the temperature between heating and cooling is common. This hysteresis can vary from a few degrees to some hundred degrees, depending on the material. Phase transitions where strong bonds are broken are often accompanied by a larger hysteresis than those where weaker bonds are broken [53].

For supramolecular materials, that are held together by weaker intermolecular forces [43], a smaller temperature hysteresis between the heating and cooling is expected.

From the expression of the heat flow rate in equation (1), DSC can find how the heat capacity of a material changes with temperature [51, 54]. A first-order or discontinuous phase transition is accompanied by a discontinuous change in the enthalpy, entropy, and volume, which are the first derivatives of the chemical potential with respect to temperature and pressure. As the transition takes place at a constant temperature, the heat capacity should be infinite at the transition temperature. However, this is not observed experimentally, which can be seen in Figure 2.10a. A second-order or continuous phase transition is, however, accompanied by a discontinuous change in the second derivatives of the chemical potential with respect to temperature and pressure. Therefore, a discontinuity in the heat capacity with temperature is expected, as illustrated in Figure 2.10b [59, 60]. A first-order and second-order phase transition will therefore be visible as sharper or broader peaks in the DSC plot, respectively.
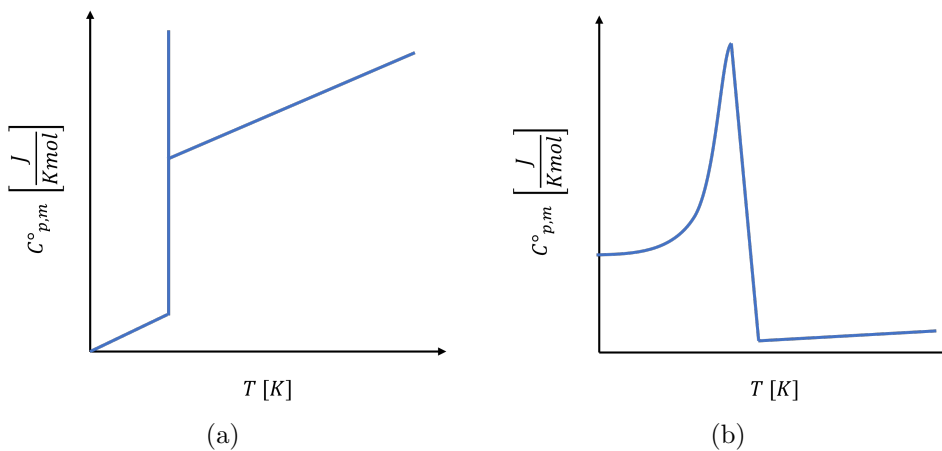

Figure 2.10: Heat capacity, C_p, as a function of temperature, T, for a (a) first-order phase transition and a (b) second-order phase transition. Adapted from Stølen et al. [59].

3 Experimental

3.1 Synthesis of tetraethylammonium and tetrabutylammonium bromotrichloroferrate(III)

Both tetraethylammonium and tetrabutylammonium bromotrichloroferrate(III), $[(C_2H_5)_4N][FeBrCl_3]$ and $[(n-C_4H_9)_4N][FeBrCl_3]$ respectively, were synthesised from an evaporation crystallisation. The chemicals used during the synthesis are listed in Table 3.1.

Table 3.1: Chemicals used during the synthesis of tetraethylammonium and tetrabutylammonium bromotrichloroferrate(III).

Chemical	Chemical formula	Manufacturer	Purity [%]
Iron(III) chloride hexahydrate	$FeCl_3 \cdot 6\,H_2O$	Sigma-Aldrich	99
Tetraethylammonium bromide	$[(C_2H_5)_4N]Br$	Sigma-Aldrich	99
Tetrabutylammonium bromide	$[(C_4H_9)_4N]Br$	Sigma-Aldrich	98
Deionized water	H_2O	NTNU	-

For the synthesis of TEAFeBrCl$_3$, shown in Figure 3.1, two precursor solutions were made by mixing iron(III) chloride hexahydrate (14.6649 g) and tetraethylammonium bromide (11.4052 g) with DI water (50 mL) in two separate beakers. The precursor solutions were stirred with a magnetic stirrer at 200 rpm for 15 min to ensure complete dissolution, before being transferred to a crystalliser and mixed at 200 rpm for 10 min. The crystalliser was covered with a sheet of paper with holes, and left on a hot plate at 40 °C in a fume hood for three days. The resulting crystals, named C-TEA, were collected, vacuum filtrated, and dried in a vacuum oven (BINDER - VD 23) at 80 °C for 4 h. The largest single crystals with a regular shape were separated from the rest of the crystals, and stored in a separate container.
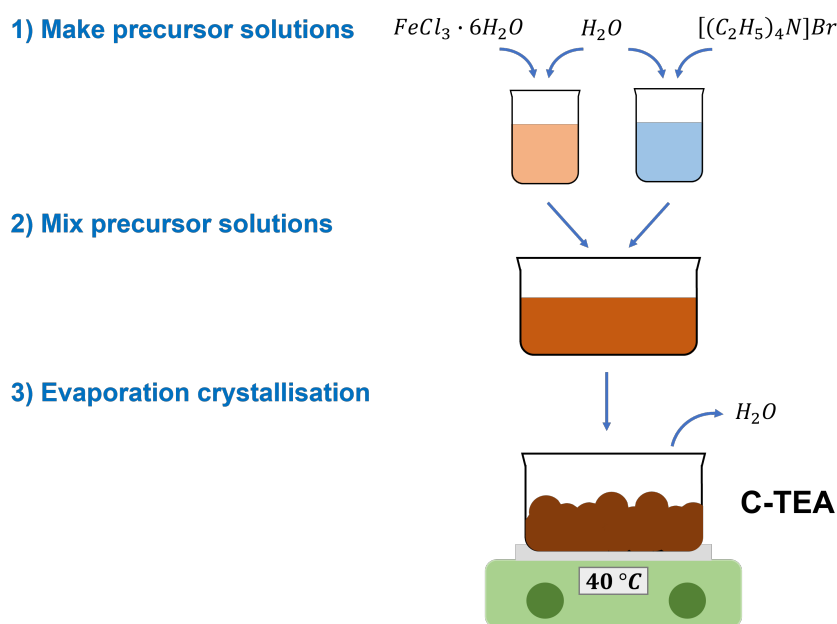

Figure 3.1: Flow chart over the experimental procedure for the synthesis of tetraethylammonium bromotrichloroferrate(III).

For the synthesis of TBAFeBrCl$_3$, shown in Figure 3.2, two precursor solutions were made by mixing iron(III) chloride hexahydrate (11.2666 g) and tetrabutylammonium bromide (13.5762 g) with DI water (50 mL) in two separate beakers. The precursor solutions were stirred with a magnetic stirrer at 200 rpm for 15 min to ensure complete dissolution, before being transferred to a crystalliser and mixed at 200 rpm for 10 min. When an instantaneous precipitate formed in the crystalliser, additional DI water (150 mL) was added while stirring the solution at 200 rpm and heating it to 40 °C for about 20 min to ensure full dissolution of the precipitate. The crystalliser was covered with a sheet of paper with holes, and left on a hot plate at 40 °C in a fume hood for three days. The crystals formed in the crystalliser, named C-TBA, were collected, vacuum filtrated, and dried in a vacuum oven (BINDER - VD 23) at 80 °C for 4 h. The largest single crystals with a regular shape were separated from the rest of the crystals, and stored in a separate container.
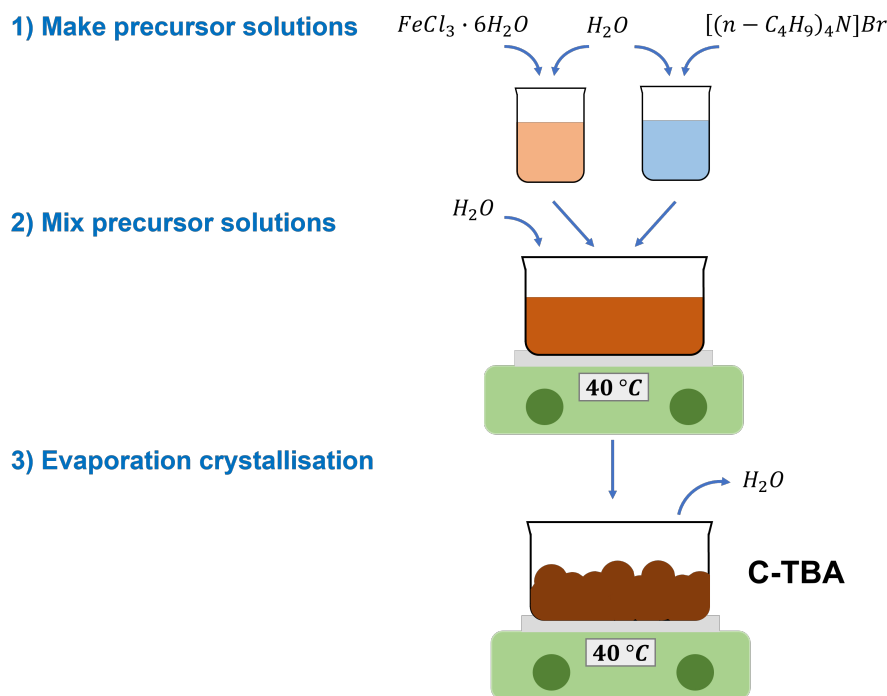

Figure 3.2: Flow chart over the experimental procedure for the synthesis of tetrabutylammonium bromotrichloroferrate(III).

3.2 Synthesis of TEA$_x$TBA$_{1-x}$FeBrCl$_3$ solid solutions

The synthesised crystals of TEAFeBrCl$_3$ (C-TEA) and TBAFeBrCl$_3$ (C-TBA), except the single crystals taken out, were separately ground to a fine powder using a mortar and pestle for about 10 min. To create crystal powder samples of TEA$_x$TBA$_{1-x}$FeBrCl$_3$ with x = 0.05, 0.1, 0.15, 0.25, 0.5, and 0.75, varying stoichiometric ratios of C-TEA and C-TBA were mixed thoroughly together. Afterwards, they were annealed in a calcination furnace (Nabertherm P330) to a temperature lower than the decomposition temperature of TBAFeBrCl$_3$, which is 255 °C in argon [19]. The samples were annealed at 240 °C or 220 °C for 2 h with a heating rate of approximately 9 °C/min and an uncontrolled cooling rate. An overview of the samples is given in Table 3.2.

Table 3.2: Overview of the samples of the $TEA_xTBA_{1-x}FeBrCl_3$ system, with x = 0, 0.05, 0.1, 0.15, 0.25, 0.5, 0.75, and 1. The annealing temperature varied between 240 °C and 220 °C, marked C1 and C2 respectively. The mol% of the tetraethylammonium cation is noted after the part indicating the annealing temperature. The amount, m, of $TEAFeBrCl_3$ (C-TEA) and $TBAFeBrCl_3$ (C-TBA) resulted in approximately 2 g of each sample.

Sample	Chemical formula	$m_{C\text{-}TEA}$ [g]	$m_{C\text{-}TBA}$ [g]
C-TBA	$TBAFeBrCl_3$	0	-
C2-TBA	$TBAFeBrCl_3$	0	0.4221
C2-5	$TEA_{0.05}TBA_{0.95}FeBrCl_3$	0.0777	1.9221
C2-10	$TEA_{0.1}TBA_{0.9}FeBrCl_3$	0.1576	1.8426
C2-15	$TEA_{0.15}TBA_{0.85}FeBrCl_3$	0.2388	1.7608
C1-25	$TEA_{0.25}TBA_{0.75}FeBrCl_3$	0.4080	1.5928
C2-25	$TEA_{0.25}TBA_{0.75}FeBrCl_3$	0.4079	1.5921
C1-50	$TEA_{0.5}TBA_{0.5}FeBrCl_3$	0.8683	1.1304
C2-50	$TEA_{0.5}TBA_{0.5}FeBrCl_3$	0.8688	1.1316
C1-75	$TEA_{0.75}TBA_{0.25}FeBrCl_3$	1.3939	0.6052
C2-75	$TEA_{0.75}TBA_{0.25}FeBrCl_3$	1.3948	0.6055
C-TEA	$TEAFeBrCl_3$	-	0

3.3 X-ray diffraction

A structural analysis of the samples in Table 3.2 was conducted using X-ray diffraction. The fine powder of plastic crystals was filled in Si-cavity 10 mm sample holders, and analysed using the Bruker D8 ADVANCE DaVinci instrument with CuKα radiation (1.5406 Å), a LynxEye™ SuperSpeed Detector, and a 90 position sample changer. X-ray diffractograms were recorded in the 2θ°-range of 10-75° for 120 min, using a fixed slit of 0.2°.

3.4 Rietveld refinement

The diffraction profiles of the samples described in Table 3.2 were fitted through a Rietveld refinement using DIFFRAC.SUITE TOPAS® [61, 62]. A crystallographic information file (CIF) for the $P6_3mc$ space group created by Walker [18] based on data from Evans et al. [16], and for the $Pnna$ space group from the COD file 2208805 [17, 48] were used as models. To determine the approximate lattice parameters, a Pawley fit was performed using hkl phases. Afterwards, a Rietveld refinement was conducted to determine the weight percentage of each phase present. The background polynomial order, sample displacement, scale, and lattice parameters were first refined. Then, a refinement of the isotropic temperature factor, $B_{eq.}$, and the preferred orientation was done. For the $P6_3mc$ and $Pnna$ structures, the preferred orientation of the (010) and (002), and (020) and (002) planes was taken into account, respectively.

3.5 Differential scanning calorimetry

Differential scanning calorimetry was performed on the samples described in Table 3.2, using the Netzsch DSC 214 Polyma instrument with aluminium crucibles (Concavus Pan Al, closed). The samples were subjected to three heating and cooling cycles between -25 and 200 °C with heating and cooling rates of 10 °C/min, and a dwell time of 10 min at the maximum and minimum temperatures. Measurements were conducted in synthetic air, and liquid nitrogen was used to control the heating rates.

Deconvolution of the DSC data into multiple single peaks was conducted using LIPRAS [63]. The background was modelled using a third order polynomial function, and single peaks were fitted to an asymmetric Gaussian profile function.

4 Results

4.1 Synthesis observations

In order to synthesise the various $TEA_xTBA_{1-x}FeBrCl_3$ compounds, the end member materials, $TEAFeBrCl_3$ and $TBAFeBrCl_3$, were first crystallised individually from solution as described in Section 3.1. An overview of the morphology, approximate size, and yield of the resulting crystals is given in Table 4.1, and photos of the crystals are given in Figure 4.1. The yield of $TEAFeBrCl_3$ crystals, named C-TEA, was 96.4% (19.3 g), and the yield of $TBAFeBrCl_3$ crystals, called C-TBA, was 87.6% (17.5 g).

Table 4.1: Approximate size, yield, and morphology of synthesised crystals of $TEAFeBrCl_3$ and $TBAFeBrCl_3$.

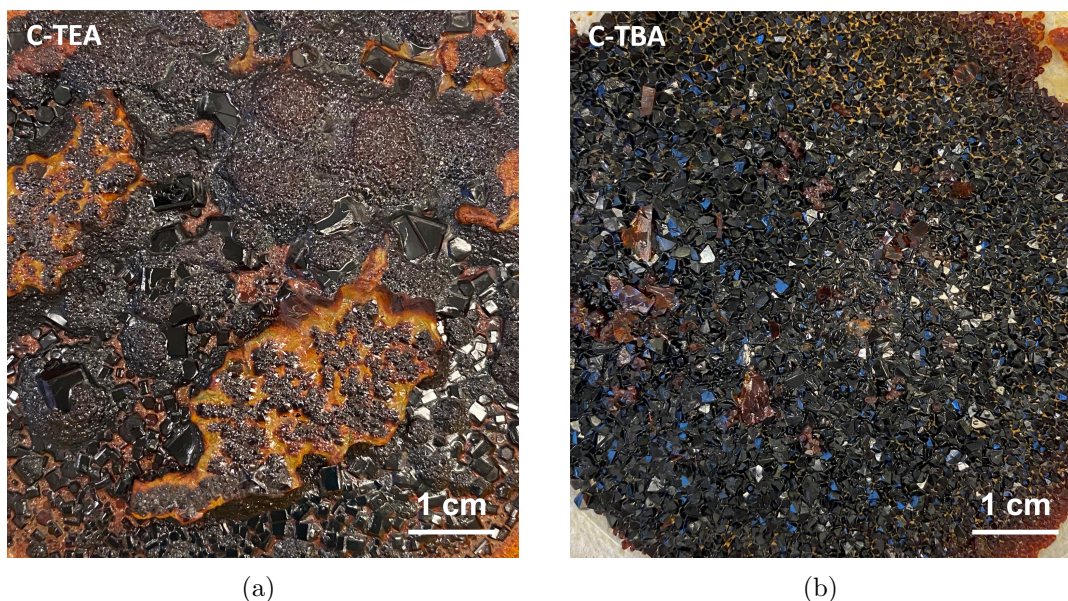| Sample	Size [mm]	Yield [%]	Morphology
C-TEA	$\sim$ 0.5-7	96.4	Dark orange with a hint of red, faceted single crystals, agglomerates, porous top layer of crystals
C-TBA	$\sim$ 0.5-2	87.6	Dark orange, faceted single crystals, agglomerates, flaky crystal sheets on top

Figure 4.1: Photos showing (a) C-TEA and (b) C-TBA crystals. The scale bars are approximate.

During the synthesis of $TEAFeBrCl_3$, no instantaneous precipitation occurred upon mixing equimolar amounts of tetraethylammonium bromide and iron(III) chloride hexahydrate in DI water, indicating that the solution was not supersaturated upon mixing. As the solution was left to crystallise at 40 °C, formation of $TEAFeBrCl_3$ crystals, named C-TEA, occurred after approximately three days. Figure 4.2 display how the crystallisation progressed. After about 48 h, precipitation of C-TEA crystals occurred at the bottom of the crystalliser and in the solution, as seen in Figure 4.2b. Some crystals were floating on the surface of the solution. Figure 4.2c shows that after about 72 h, almost all of

the solution had evaporated, and more crystals were crystallised. The resulting C-TEA crystals, shown in Figure 4.2d, included both faceted single crystals with a prominent hexagonal crystal symmetry, and agglomerates. The surface crystals formed a porous layer of smaller, agglomerated crystals on top of the rest of the crystals. This layer potentially hindered the growth of the bottom crystals, which ended up with an irregular surface. The size of the crystals varied, indicating multiple nucleation and growth stages during the crystallisation.
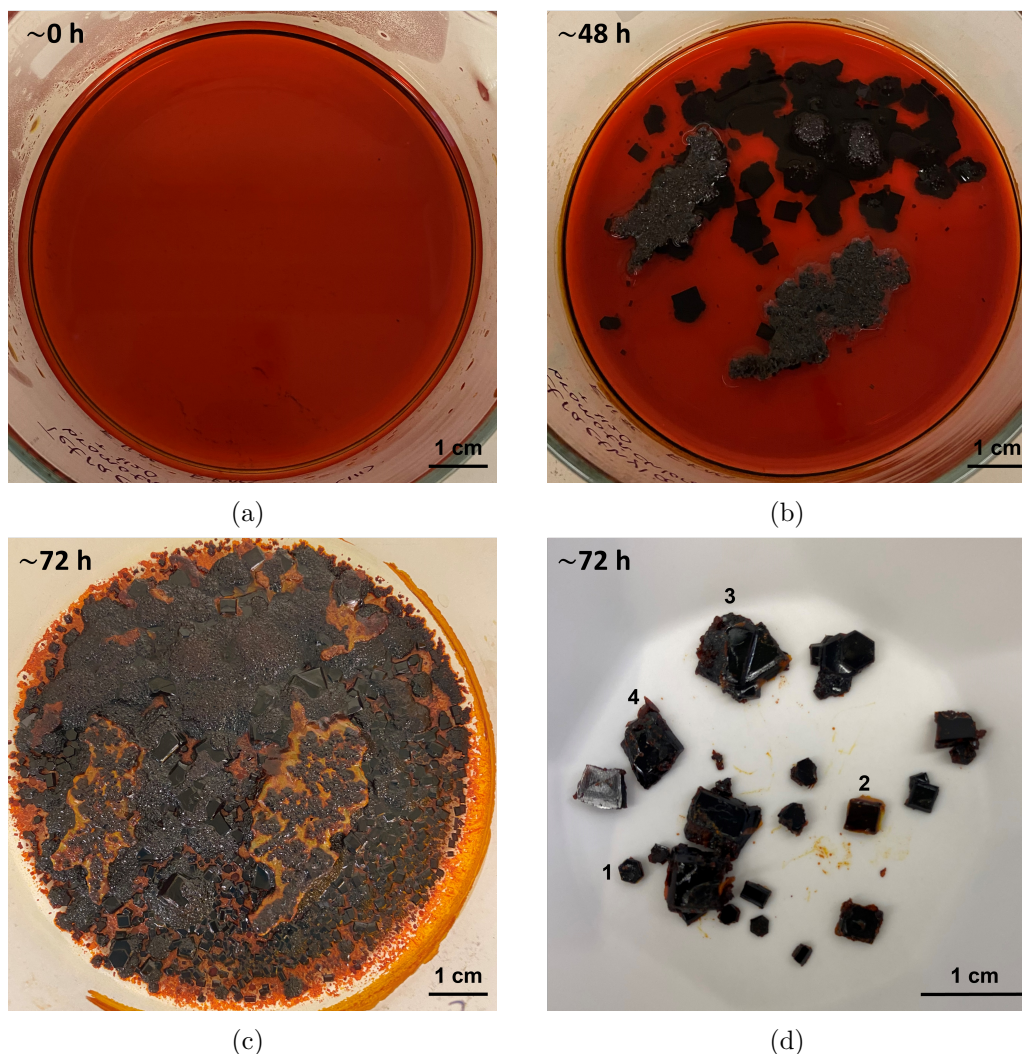

Figure 4.2: Photos showing how the crystallisation process of TEAFeBrCl$_3$ progressed over three days. (a) Solution after mixing the precursor solutions. (b) Crystals precipitated after ~ 48 h. (c) The final crystals after ~ 72 h. (d) Close-up of final crystals. Both faceted single crystals with a hexagonal symmetry, such as crystal 1 and 2, and agglomerates, such as crystal 3, resulted. Some of the hexagonal single crystals, like crystal 4, had an uneven surface. The scale bars are approximate.

For TBAFeBrCl$_3$, instantaneous precipitation occurred when the precursor solutions were mixed. The instantaneous precipitate can be seen in Figure 4.3a, and was a fine powder with a dark orange colour. Hence, TBAFeBrCl$_3$ seems to be less soluble in DI water compared to TEAFeBrCl$_3$. As a result, more DI water (150 mL) had to be added to dissolve the instantaneous precipitate. Final crystals of TBAFeBrCl$_3$, called C-TBA, were formed in three days when the solution was left to crystallise at 40 °C. Precipitation of

the C-TBA crystals was observed after approximately 24 h, as shown in Figure 4.3b. The solution looked murky with a fine powder, and a thin, flaky layer of crystals was observed on the surface of the solution. After about 48 h, smaller crystals had started to form at the bottom of the crystalliser, and the surface crystal sheets had grown larger. Most of the solution had evaporated after three days, as shown in Figure 4.3c, and the crystals had grown further. The bottom of the crystalliser was covered in a closely packed layer of smaller, faceted single crystals and agglomerates, which is shown in Figure 4.1b and 4.3c. The C-TBA crystals were more uniform in size than the C-TEA crystals. The orthorhombic crystal symmetry was not well defined for the final crystals imaged in Figure 4.3d. As the bottom crystal layer was densely packed, the growth might have been hindered in multiple directions, preventing a more regular final crystal morphology. The flaky surface crystals formed larger sheets at the surface of the solution.
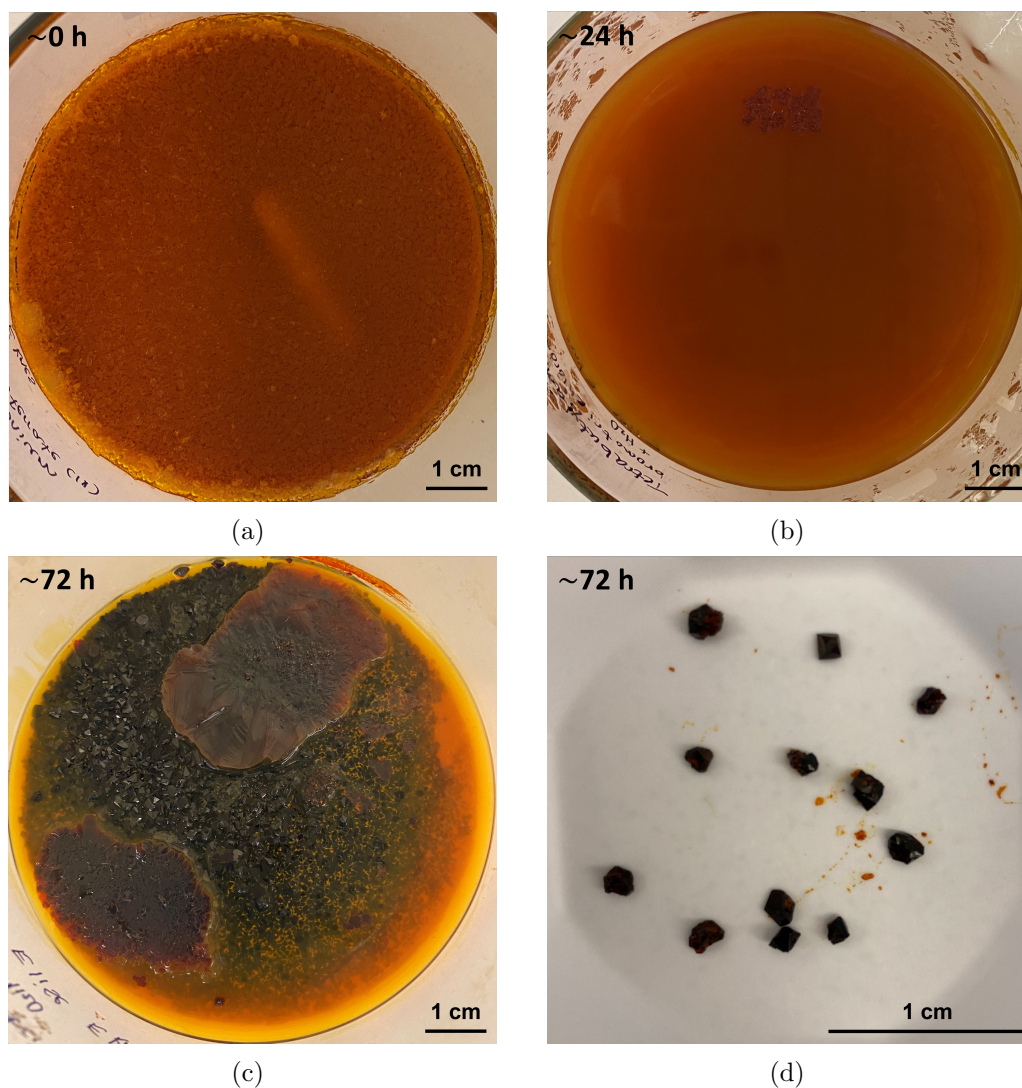

Figure 4.3: Photos showing how the crystallisation process of TBAFeBrCl$_3$ progressed over three days. (a) Instantaneous precipitate formed upon mixing the precursor solutions. The magnetic stirrer is still in the solution. (b) Crystals precipitated after $\sim$ 24 h. (c) The final crystals after $\sim$ 72 h. (d) Close-up of final crystals. The scale bars are approximate.

4.2 Effect of annealing temperature on the $TEA_xTBA_{1-x}FeBrCl_3$ system

Samples of $TEA_xTBA_{1-x}FeBrCl_3$ with x = 0.05, 0.1, 0.15, 0.25, 0.5, and 0.75, were prepared as described in Section 3.2. $TEA_xTBA_{1-x}FeBrCl_3$ samples with x = 0.25, 0.5, and 0.75, were first annealed at 240 °C for 2 h in an attempt to promote solid solution formation, as this had previously been done with success for the similar $TMA_xTEA_{1-x}FeBrCl_3$ system [64]. However, the calcination oven used for annealing overshot the temperature, resulting in a maximum temperature of about 264 °C, which is above the decomposition temperature of $TBAFeBrCl_3$ at 255 °C [19]. When looking at the mass loss during annealing for these samples, named C1 in Table 4.2, it was between 1.5-1.8%. Additionally, some residue can be seen at the sides of the glass containers in Figure 4.4a after annealing, indicating a volatile component in the sample. Therefore, to take into account the overshooting of the temperature by the calcination furnace, a new annealing temperature of 220 °C was set, which gave a maximum temperature of about 246 °C. The resulting mass loss after annealing for these samples, called C2 in Table 4.2, was reduced to 0.5-0.7%, and less residue can be seen at the sides of the containers in Figure 4.4b after annealing. One exception to this is the C2-TBA sample, that had a mass loss of about 1.3% at the lower annealing temperature.

Table 4.2: The yield and mass loss during annealing for samples of the $TEA_xTBA_{1-x}FeBrCl_3$ system with x = 0, 0.05, 0.1, 0.15, 0.25, 0.5, and 0.75. For samples with x = 0.25, 0.5 and 0.75, two batches were made and annealed at different temperatures, with batch 1 and 2 being annealed at 240 °C and 220 °C respectively.

Sample	Chemical formula	Yield [%]	Mass loss annealing [%]
C2-TBA	$TBAFeBrCl_3$	98.7	1.3
C2-5	$TEA_{0.05}TBA_{0.95}FeBrCl_3$	99.5	0.5
C2-10	$TEA_{0.1}TBA_{0.9}FeBrCl_3$	99.4	0.6
C2-15	$TEA_{0.15}TBA_{0.85}FeBrCl_3$	99.5	0.5
C1-25	$TEA_{0.25}TBA_{0.75}FeBrCl_3$	98.5	1.5
C1-50	$TEA_{0.5}TBA_{0.5}FeBrCl_3$	98.2	1.8
C1-75	$TEA_{0.75}TBA_{0.25}FeBrCl_3$	98.4	1.6
C2-25	$TEA_{0.25}TBA_{0.75}FeBrCl_3$	99.4	0.6
C2-50	$TEA_{0.5}TBA_{0.5}FeBrCl_3$	99.4	0.6
C2-75	$TEA_{0.75}TBA_{0.25}FeBrCl_3$	99.3	0.7

(a)   (b)
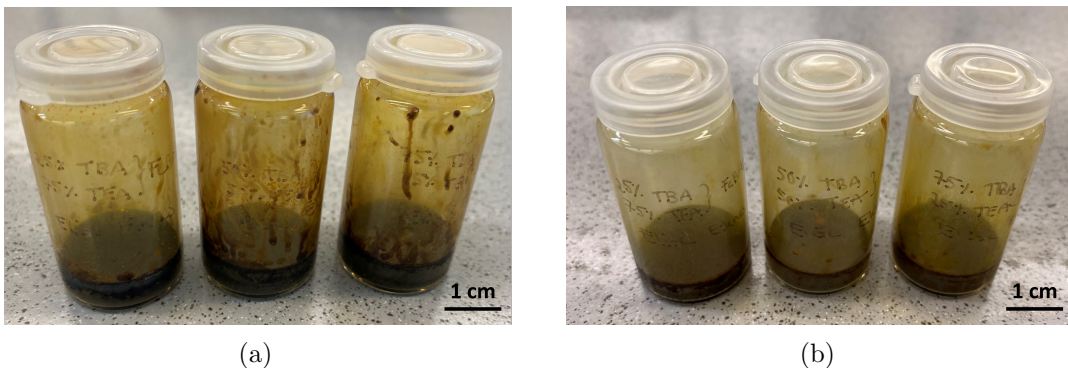
Figure 4.4: Photos showing how the residue on the sides of the containers looked after annealing at (a) 240 °C, with a maximum temperature of 264 °C, and (b) 220 °C, with a maximum temperature of 246 °C. More residue is visible in (a) compared to (b). The scale bars are approximate.

The samples developed a darker orange colour after annealing. The colour varied between samples with different compositions, as TEAFeBrCl$_3$ is more red than TBAFeBrCl$_3$. The samples annealed at 240 °C had a darker colour than those annealed at 220 °C, as shown in Figure 4.5 for the TEA$_{0.5}$TBA$_{0.5}$FeBrCl$_3$ sample. All samples went through a phase transition to the mesophase or a liquid during the annealing, as they looked as though they had flowed significantly to fit the geometry of the container.
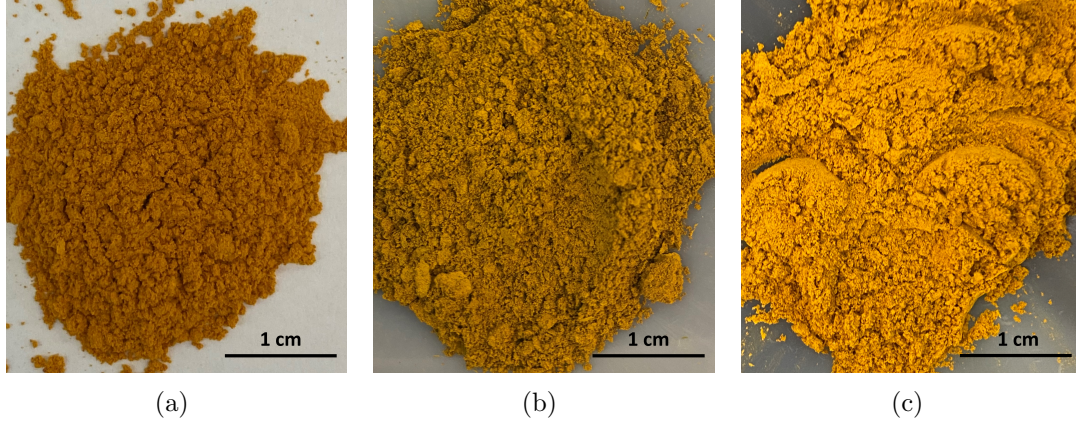

Figure 4.5: Photos showing the TEA$_{0.5}$TBA$_{0.5}$FeBrCl$_3$ sample (a) before annealing, (b) after annealing at 240 °C (C1-50), and (c) after annealing at 220 °C (C2-50). The scale bars are approximate.

To investigate if there was a structural difference between the samples annealed at 240 °C and 220 °C, XRD was used to analyse them. The resulting XRD diffractogram comparing C1-50 and C2-50 is given in Figure 4.6. The diffractograms are normalised by dividing the measured intensities for a sample by the maximum peak intensity of that sample. No large variations between the two diffractograms can be observed, indicating that the structure did not change significantly at the higher annealing temperature compared to the lower one. However, the higher intensity of the background relative to the peak intensity of C1-50, mostly visible between 10 and 20 2θ, could indicate the presence of more amorphous material in the sample annealed at 240 °C.
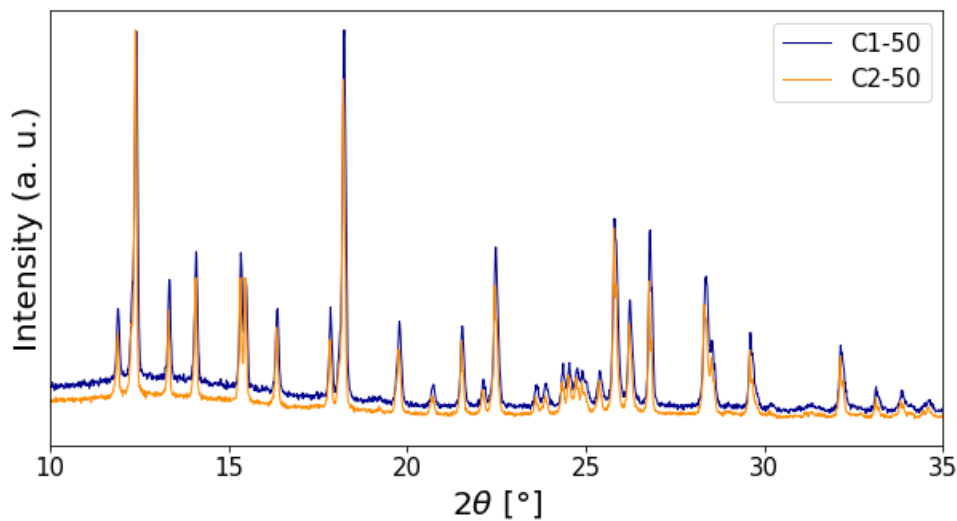

Figure 4.6: X-ray diffractograms of C1-50 and C2-50 samples, annealed at 240 °C and 220 °C, respectively. Both diffractograms are normalised, giving relative intensities.

4.3 Crystal structure of TEA$_x$TBA$_{1-x}$FeBrCl$_3$ materials

To obtain an understanding of how the crystal structure change as a function of composition in the TEA$_x$TBA$_{1-x}$FeBrCl$_3$ system, and to learn if any solid solution formation occurs between the two end members, XRD was used to analyse the different samples. In Figure 4.7, an overview of the X-ray diffractograms of the end members and the samples annealed at 220 °C is given. hkl-ticks and corresponding Miller indices from Rietveld refinement of the end members are also noted in the overview. Diffraction lines of both end members, C-TEA and C2-TBA, are present for all compounds, and no large shifts in the peak positions are observed. This indicates little to no solid solution formation between the end members for the materials analysed. The individual diffractograms of each sample including observed data, calculated fit from Rietveld refinement, difference between observed and calculated data, and hkl-ticks for the *P6$_3$mc* and *Pnna* phases are presented in Figures A.1-A.9 in Appendix A.

Results from the Rietveld refinement are shown in Table 4.3, which includes the weight percentage of the phase, lattice parameters, and goodness of fit (GOF) of both the *P6$_3$mc* and *Pnna* phase for the end members and the samples annealed at 220 °C.

Table 4.3: Parameters from Rietveld refinement of TEA$_x$TBA$_{1-x}$FeBrCl$_3$ compounds with x = 0, 0.05, 0.1, 0.15, 0.25, 0.5, 0.75, and 1. C2 indicates that the sample was annealed at 220 °C. For both the *P6$_3$mc* and *Pnna* phase, the weight percentage of the phase, lattice parameters, and goodness of fit are noted for each compound. A parenthesis is given around the first uncertain digit in TOPAS [61, 62].

| Sample	Phase [wt%]	a [Å]	b [Å]	c [Å]	GOF
P6$_3$mc phase					
C-TEA	100.000	8.2598 (4)	8.2598 (4)	13.3166 (7)	4.07
C2-75	57.4 (11)	8.2629 (2)	8.2629 (2)	13.3195 (4)	2.9
C2-50	36.5 (7)	8.2626 (2)	8.2626 (2)	13.3209 (6)	2.98
C2-25	15.5 (3)	8.2614 (2)	8.2614 (2)	13.3182 (5)	1.96
C2-15	9.3 (3)	8.2624 (3)	8.2624 (3)	13.3207 (7)	1.91
C2-10	8.4 (3)	8.2622 (5)	8.2622 (5)	13.3223 (16)	1.97
C2-5	4.8 (4)	8.2615 (8)	8.2615 (8)	13.3216 (18)	1.85
Pnna phase					
C2-75	42.6 (11)	18.494 (2)	11.5851 (11)	11.4778 (11)	2.9
C2-50	63.5 (7)	18.4976 (14)	11.5826 (7)	11.4767 (7)	2.98
C2-25	84.5 (3)	18.4970 (7)	11.5797 (4)	11.4756 (4)	1.96
C2-15	90.7 (3)	18.4964 (6)	11.5798 (3)	11.4765 (4)	1.91
C2-10	91.6 (3)	18.4969 (7)	11.5804 (4)	11.4771 (4)	1.97
C2-5	95.2 (4)	18.4947 (5)	11.5812 (3)	11.4756 (3)	1.85
C2-TBA	100.000	18.5021 (6)	11.5828 (4)	11.4782 (4)	1.73
C-TBA	100.000	18.4838 (11)	11.5708 (7)	11.4638 (7)	3.49
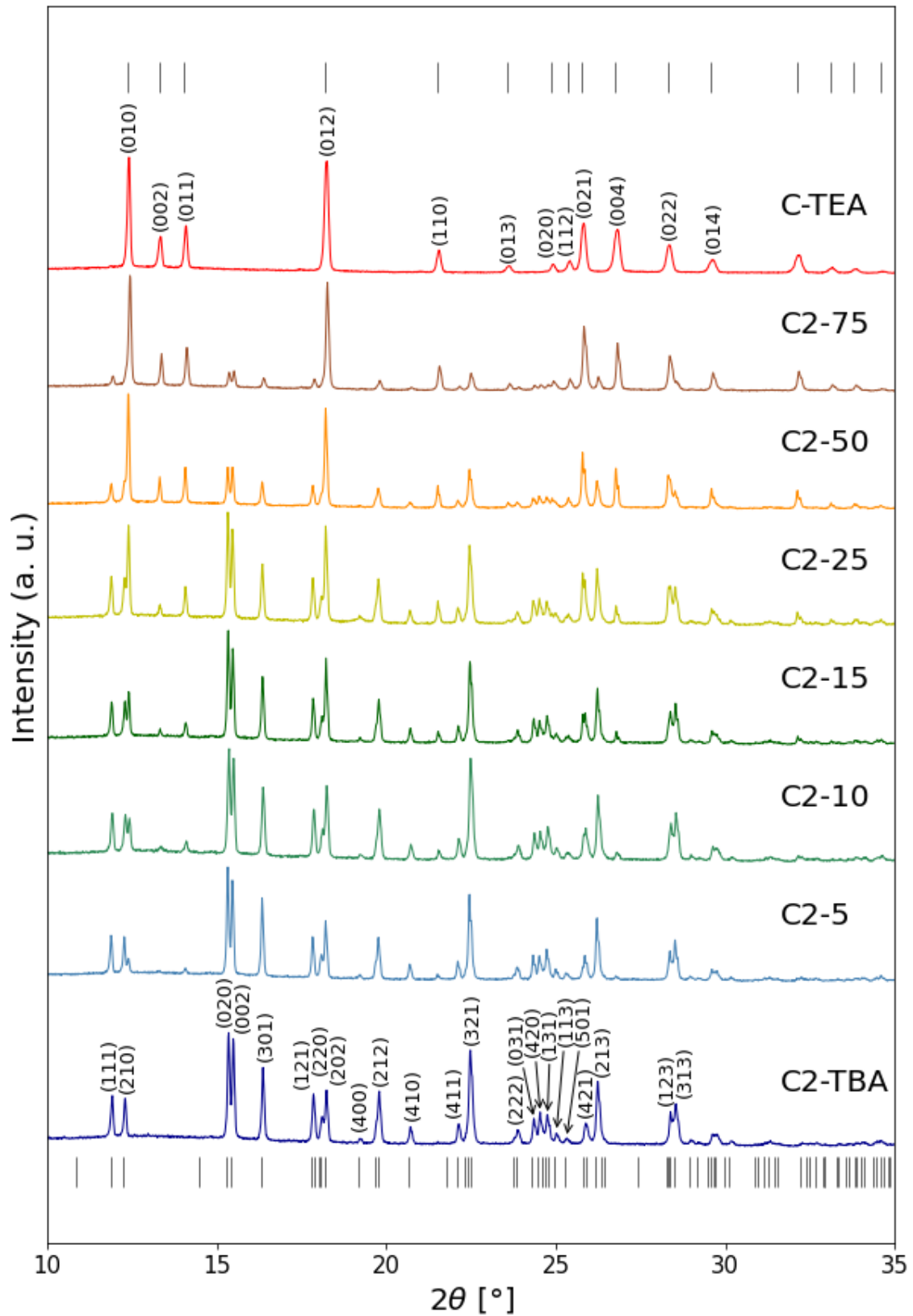
Figure 4.7: X-ray diffractograms of $TEA_xTBA_{1-x}FeBrCl_3$ compounds with x = 0, 0.05, 0.1, 0.15, 0.25, 0.5, 0.75, and 1. C2 indicates that the sample was annealed at 220 °C. hkl-ticks are shown in grey at the top and bottom, and correspond to diffraction lines of the $P6_3mc$ and $Pnna$ phases, respectively. Miller indices from Rietveld refinement are noted for the end member materials, C-TEA and C2-TBA. All the diffractograms are normalised, giving relative intensities.

Rietveld refinement of the end members revealed that TEAFeBrCl$_3$ has the *P6$_3$mc* space group, and that TBAFeBrCl$_3$ has the *Pnna* space group. Both end members contained no secondary phases. The resulting Rietveld refinement shows that both end member phases are present in all the analysed compositions in the TEA$_x$TBA$_{1-x}$FeBrCl$_3$ system, and the amount of each phase approximately corresponds to the amount of each end member in the compound, as near linear changes in the weight percentages are observed. For example, the more TEAFeBrCl$_3$ in the compound, the larger the weight percentage of the *P6$_3$mc* phase. This is illustrated in Figure 4.8. *Pnna* is the majority phase for the C2-50, C2-15, C2-10, and C2-5 samples, and *P6$_3$mc* is the majority phase for the C2-75 sample.
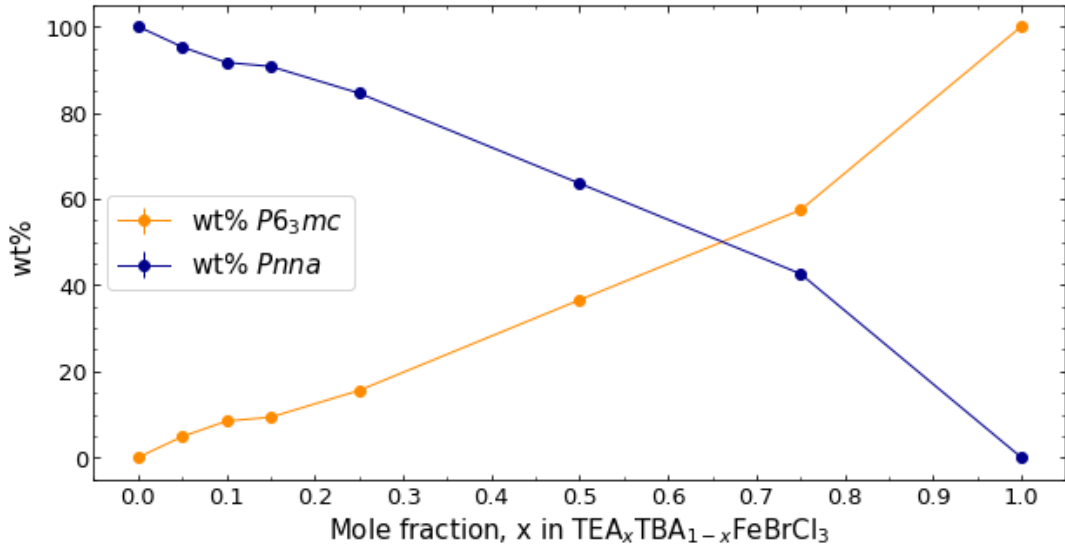

Figure 4.8: Weight percent of the *P6$_3$mc* and *Pnna* phases as a function of x in the TEA$_x$TBA$_{1-x}$FeBrCl$_3$ system. For x = 0, the values are for the C2-TBA sample. The values are retrieved from Rietveld refinement, and corresponding errors are estimated in TOPAS [61, 62]. The error bars are too small to be visible.

The variation in lattice parameters of the *P6$_3$mc* and *Pnna* phases as a function of composition was extracted from the Rietveld refinements, and the results are shown in Figure 4.9. Table B.1 in Appendix B present the lattice parameters and corresponding errors estimated in TOPAS [61, 62]. There are only small changes in the lattice parameters. For the *P6$_3$mc* phase, the lattice parameters, a and c, follow a similar trend. A slight increase in the lattice parameters can be seen between the C2-TBA and C2-5 sample, before a slight decrease is observed until the composition of C2-25 is reached. Afterwards, the lattice parameters increase again, before decreasing slightly at the higher mole fractions of TEAFeBrCl$_3$. In the *Pnna* phase, lattice parameters a and c follow a similar trend between the C2-TBA and C2-15 sample. The a and c lattice parameters decrease, increase, and decrease again. Lattice parameter b, on the other hand, decreases between the C2-TBA and C2-15 sample. As the mole fraction of TEAFeBrCl$_3$ increases from the C2-15 sample, lattice parameters b and c both increase slightly. Lattice parameter a decreases instead. The small changes in the lattice parameters indicate that the structures influence each other to some degree when mixed and annealed at 220 °C.
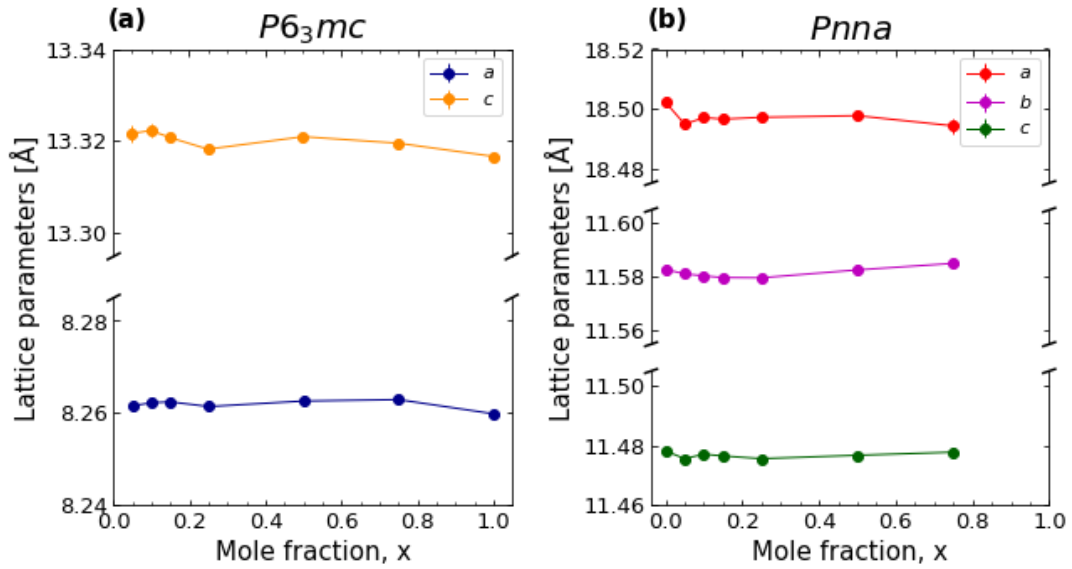
Figure 4.9: Lattice parameters of the *P6₃mc* and *Pnna* phases as a function of x in the TEA$_x$TBA$_{1-x}$FeBrCl$_3$ system. x is the mole fraction of TEAFeBrCl$_3$. For x = 0, the values are for the C2-TBA sample. The values are retrieved from Rietveld refinement, and corresponding errors are estimated in TOPAS [61, 62]. For most samples, the error bars are too small to be visible.

Figure 4.10 shows how the GOF-value in Table 4.3 changes as a function of composition, and can give an indication of the accuracy of the calculated fit from Rietveld refinement. The GOF is relatively large for samples containing a larger amount of TEAFeBrCl$_3$, such as sample C-TEA, C2-75, and C2-50, as a value close to 1 indicates a good fit. The individual diffractograms in Figures A.1-A.4 in Appendix A, show that the deviation between the observed and calculated data mostly stems from a mismatch between the intensities. This intensity mismatch may be related to imperfect atomic positions in the structural model, or preferred orientation of the packed TEAFeBrCl$_3$-powder.
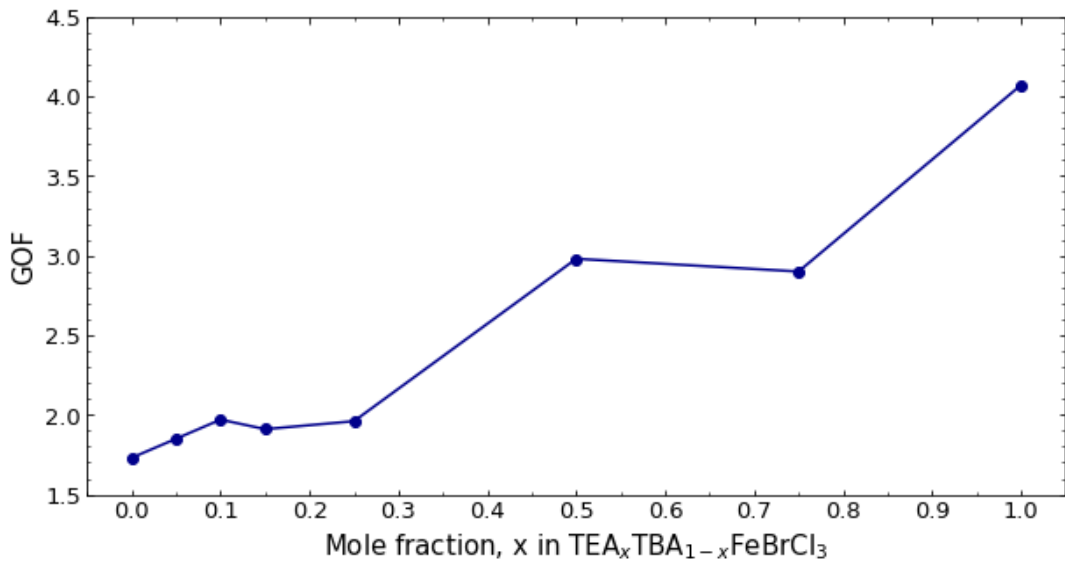

Figure 4.10: Goodness of fit from Rietveld refinement as a function of composition in the TEA$_x$TBA$_{1-x}$FeBrCl$_3$ system. For x = 0, the GOF-value is for the C2-TBA sample.

4.4 Thermodynamic properties of $TEA_xTBA_{1-x}FeBrCl_3$ materials

Differential scanning calorimetry was used to understand how the enthalpy, entropy, and phase transition temperatures change as a function of composition in the $TEA_xTBA_{1-x}FeBrCl_3$ system. The individual DSC results between -25 and 200 °C for the end members, C-TEA and C-TBA, are shown in Figures 4.11 and 4.12. Each peak represents a phase transition, and the onset temperature for these transitions is marked with a dashed, grey line. The corresponding temperature is noted in red on heating and in blue on cooling. C-TEA goes through an endothermic phase transition at 149 °C on heating, and the reverse exothermic reaction at 91 °C on cooling. A hysteresis of 58 °C for the onset temperature is therefore present. C-TBA goes through two endothermic phase transitions on heating, where the one at 111 °C corresponds to the mesophase transition, and the one at 129 °C corresponds to the melting. The reverse exothermic phase transitions are observed at 111 °C and 84 °C, meaning there is a hysteresis in the onset temperature for these transitions. The individual DSC results for the remaining samples, C2-TBA, C2-5, C2-10, C2-15, C2-25, C2-50, and C2-75, are found in Figures C.1-C.7 in Appendix C.

An overview of the DSC results for the second thermal cycle on heating and on cooling for all samples is shown in Figure 4.13 and 4.14, respectively. The onset temperature, end temperature, enthalpy, entropy, and full width half maximum (FWHM) were extracted for each transition. These values are presented in Table 4.4 on heating, and in Table 4.5 on cooling. The errors for the onset and end temperatures are estimated directly from the DSC curves on heating and cooling in Figure 4.13 and 4.14. The enthalpy and entropy errors are based on these estimated errors of the onset and end temperatures. The FWHM error is based on the error due to the sampling frequency. More details about the error estimates is given in Appendix D. The focus will be on the results on heating for this study, as larger variations in the peak position and shape were observed between thermal cycles on cooling compared to on heating.
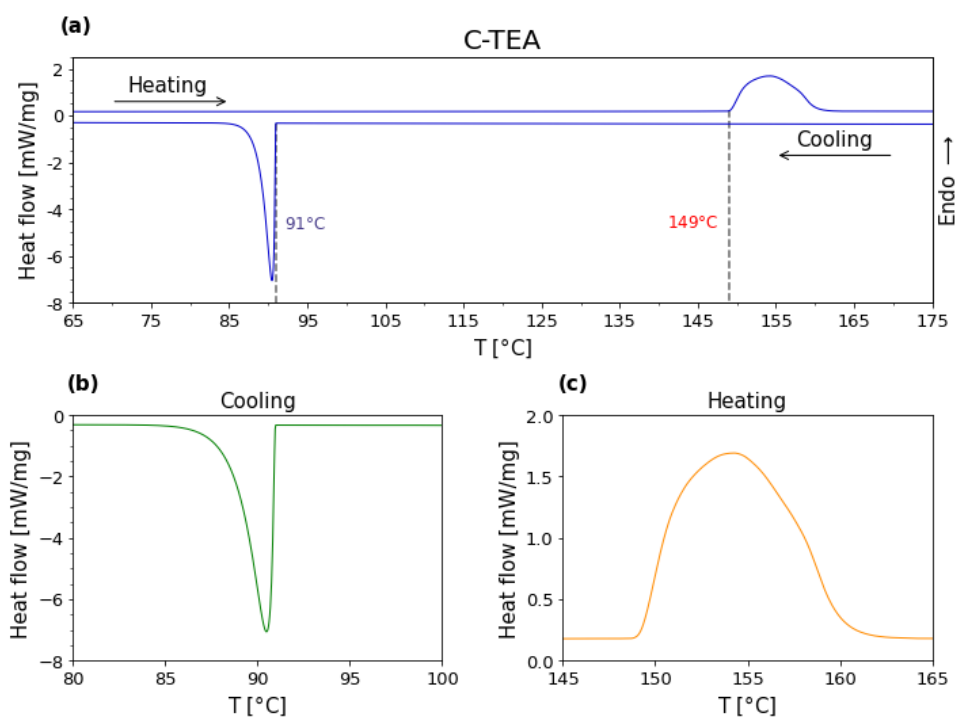
Figure 4.11: **(a)** DSC measurement of C-TEA crystals from 65 to 175 °C. The dashed, grey lines mark the onset temperature for the phase transition on heating and cooling. The temperatures are noted in red on heating and in blue on cooling. **(b)** Peak indicating a phase transition on cooling. **(c)** Peak indicating a phase transition on heating.
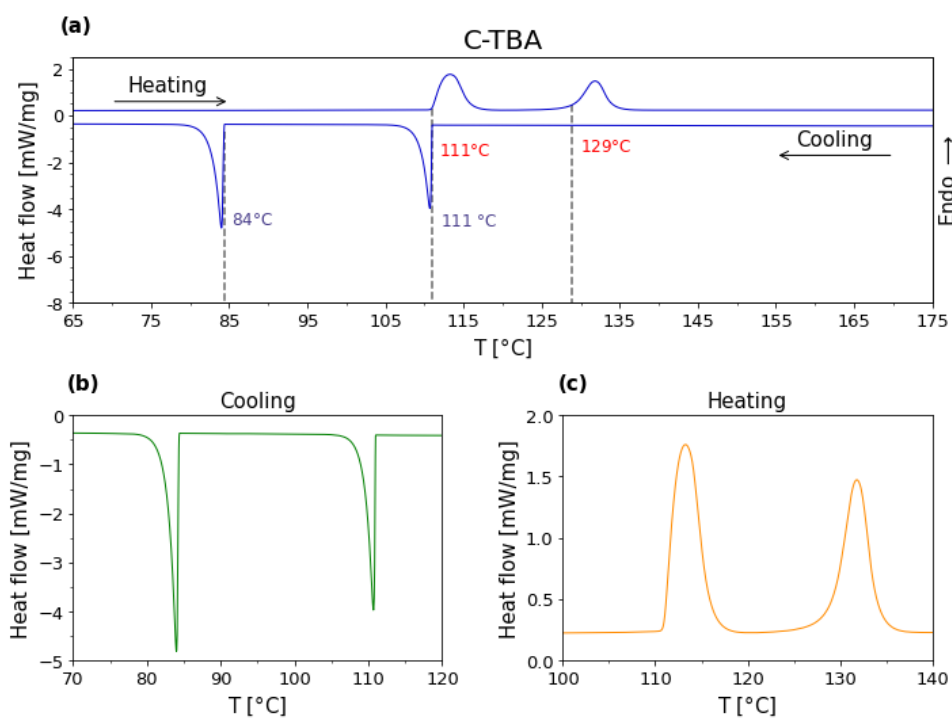
Figure 4.12: **(a)** DSC measurement of C-TBA crystals from 65 to 175 °C. The dashed, grey lines mark the onset temperature for the phase transition on heating and cooling. The temperatures are noted in red on heating and in blue on cooling. **(b)** Peaks indicating phase transitions on cooling. **(c)** Peaks indicating phase transitions on heating.

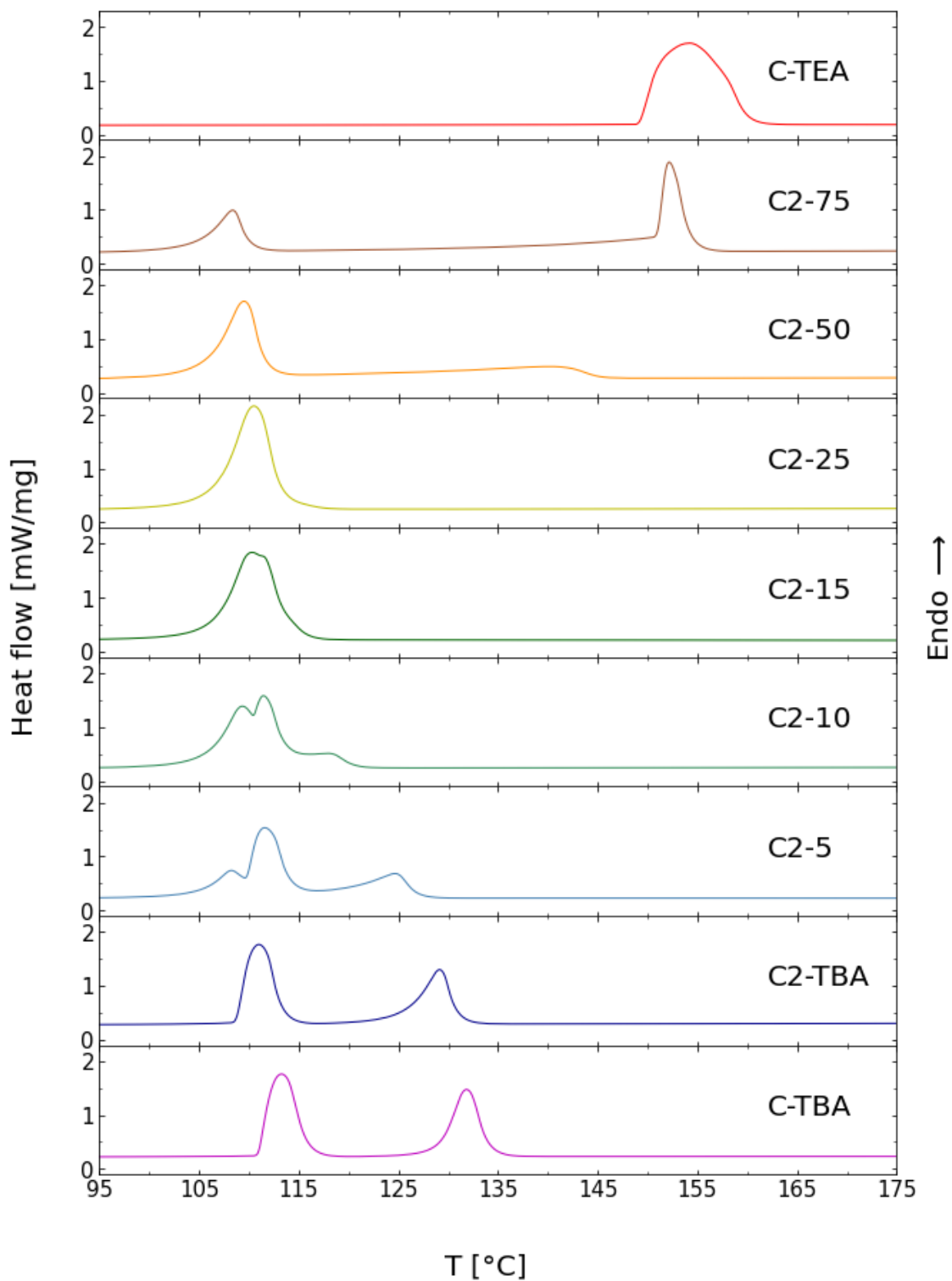Figure 4.13: DSC results on heating for the second thermal cycle between 95 and 175 °C. The results are given in a way that the amount of $TEAFeBrCl_3$ in the sample decreases down in the plot. Results for both the annealed and non-annealed samples of $TBAFeBrCl_3$ are shown.

Table 4.4: The onset temperature, end temperature, enthalpy, entropy, and FWHM for each phase transition found on heating during the second thermal cycle using DSC. For each sample, the peak number is given, where 1 is the first transition on heating, and 3 is the last. Deconvoluted peaks are marked with *. The estimated error for the onset and end temperatures, enthalpy, entropy, and FWHM are included.

| Sample	Peak no.	$T_{o, h}$ [°C]	$T_{e, h}$ [°C]	ΔH_h [$\frac{kJ}{mol}$]	ΔS_h [$\frac{J}{molK}$]	FWHM$_h$ [°C]
C-TEA	1	149 ± 0.5	160 ± 1	24.3 ± 2.6	57.5 ± 6.2	7.9 ± 0.07
C2-75	1	104 ± 1	110 ± 0.5	4.3 ± 0.9	11.3 ± 2.5	3.2 ± 0.07
	2*	122 ± 5	167 ± 5	11.6 ± 0.7	29.4 ± 2.2	18.5 ± 0.07
	3*	151 ± 0.5	155 ± 1	6.9 ± 2.0	16.2 ± 4.8	2.1 ± 0.07
C2-50	1*	105 ± 2	112 ± 1	11.6 ± 4.9	30.6 ± 13.2	4.1 ± 0.07
	2*	113 ± 5	145 ± 2	8.3 ± 3.5	21.4 ± 9.4	16.6 ± 0.07
C2-25	1	106 ± 1	113 ± 1	15.7 ± 3.6	41.4 ± 9.6	4.1 ± 0.07
C2-15	1*	104 ± 1	111 ± 0.5	6.5 ± 1.6	17.1 ± 4.3	3.6 ± 0.07
	2*	108 ± 1	113 ± 0.5	8.8 ± 3.1	23.1 ± 8.3	3.2 ± 0.07
	3*	110 ± 1	116 ± 0.5	4.6 ± 1.5	12.0 ± 4.1	3.6 ± 0.07
C2-10	1*	105 ± 1	111 ± 0.5	8.7 ± 2.1	22.9 ± 5.7	3.3 ± 0.07
	2*	110 ± 0.5	114 ± 1	6.5 ± 1.9	16.8 ± 5.1	2.2 ± 0.07
	3*	103 ± 5	121 ± 0.5	5.5 ± 1.4	14.7 ± 3.9	8.2 ± 0.07
C2-5	1*	104 ± 1	110 ± 1	3.5 ± 0.9	9.3 ± 2.4	3.1 ± 0.07
	2*	109 ± 0.5	115 ± 1	9.7 ± 1.8	25.3 ± 4.7	3.2 ± 0.07
	3*	114 ± 3	127 ± 0.5	6.5 ± 1.8	16.7 ± 4.8	6.1 ± 0.07
C2-TBA	1	109 ± 0.5	113 ± 1	12.2 ± 4.8	31.9 ± 12.5	3.2 ± 0.07
	2	125 ± 1	131 ± 1	6.5 ± 2.4	16.4 ± 6.0	3.1 ± 0.07
C-TBA	1	111 ± 0.5	116 ± 1	13.4 ± 4.1	34.8 ± 10.8	3.3 ± 0.07
	2	129 ± 1	134 ± 1	8.0 ± 3.1	19.9 ± 7.7	3.0 ± 0.07
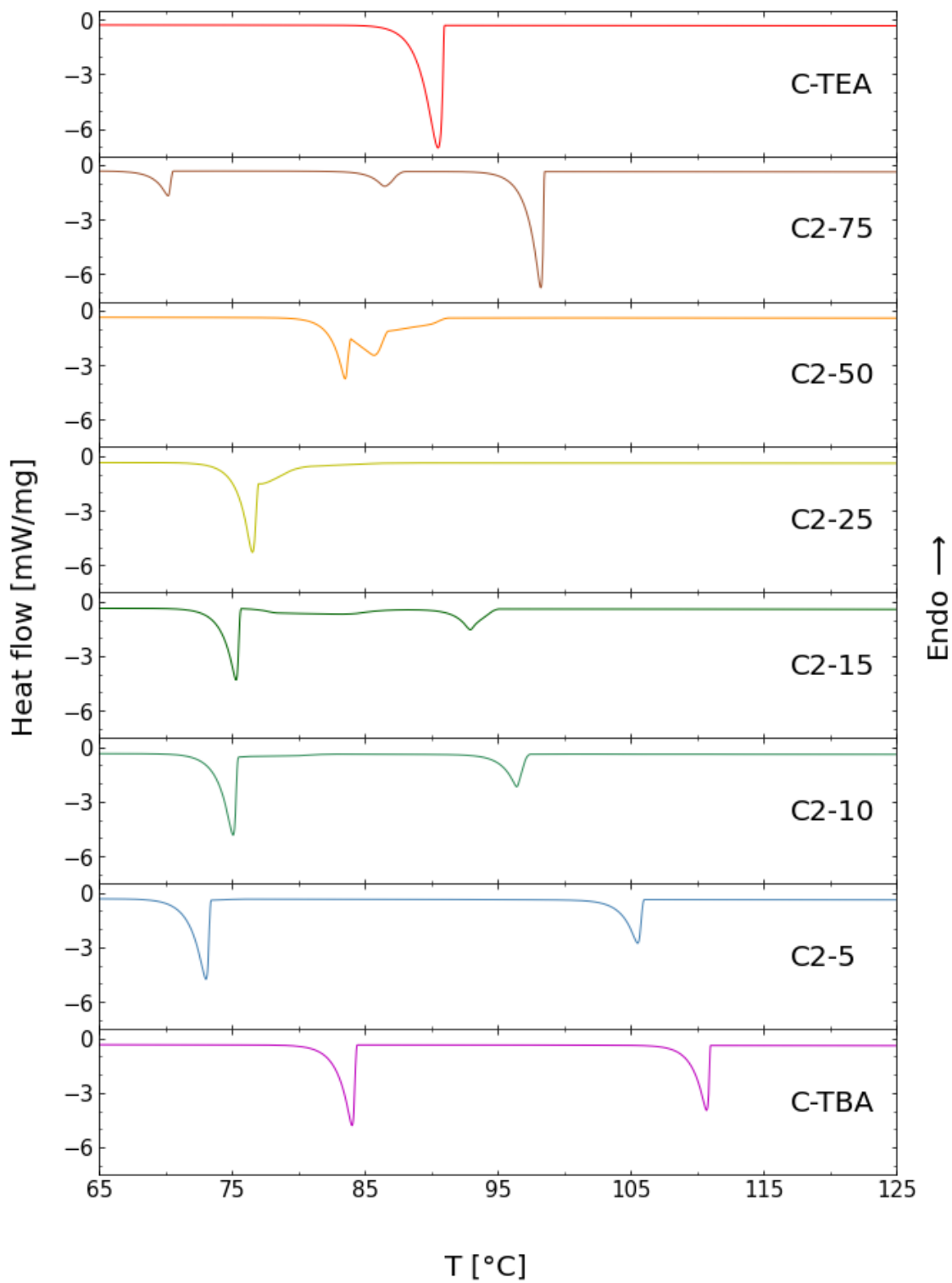
Figure 4.14: DSC results on cooling for the second heating cycle between 65 and 125 °C. The results are given in a way that the amount of $TEAFeBrCl_3$ in the sample decreases further down in the plot. Only the result for the sample of $TBAFeBrCl_3$ that is not annealed, C-TBA, is given, as the cooling was not controlled for the annealed C2-TBA sample.

Table 4.5: The onset temperature, end temperature, enthalpy, entropy, and FWHM for each phase transition found on cooling during the second thermal cycle using DSC. For each sample, the peak number is given, where 1 is the first transition on heating, and 4 is the last. Deconvoluted peaks are marked with *. Only the result for the sample of TBAFeBrCl$_3$ that is not annealed, C-TBA, is given, as the cooling was not controlled for the annealed C2-TBA sample. The estimated error for the onset and end temperatures, enthalpy, entropy, and FWHM are included.

Sample	Peak no.	$T_{o, c}$ [°C]	$T_{e, c}$ [°C]	ΔH_c [$\frac{kJ}{mol}$]	ΔS_c [$\frac{J}{molK}$]	FWHM$_c$ [°C]
C-TEA	1	91 ± 0.1	88 ± 0.5	-18.7 ± 8.1	-51.2 ± 22.2	1.5 ± 0.07
C2-75	1	98 ± 0.1	97 ± 0.5	-13.3 ± 7.2	-35.8 ± 19.3	0.9 ± 0.07
	2	88 ± 0.5	85 ± 0.5	-2.5 ± 1.7	-7.0 ± 4.6	1.6 ± 0.07
	3	70 ± 0.1	68 ± 0.5	-3.3 ± 1.8	-9.7 ± 5.2	1.0 ± 0.07
C2-50	1*	91 ± 0.5	84 ± 1	-2.4 ± 1.0	-6.6 ± 2.8	3.3 ± 0.07
	2*	90 ± 1	86 ± 0.5	-2.4 ± 1.5	-6.5 ± 4.2	2.5 ± 0.07
	3*	87 ± 0.5	82 ± 1	-10.8 ± 6.3	-29.9 ± 17.4	2.6 ± 0.07
	4*	84 ± 0.1	82 ± 0.5	-4.9 ± 3.3	-13.8 ± 9.1	0.9 ± 0.07
C2-25	1*	81 ± 1	74 ± 1	-8.9 ± 5.1	-25.1 ± 14.3	3.1 ± 0.07
	2*	77 ± 0.1	75 ± 0.5	-10.3 ± 5.6	-29.4 ± 16.0	1.0 ± 0.07
C2-15	1*	95 ± 0.5	91 ± 1	-4.3 ± 3.3	-11.8 ± 9.0	2.3 ± 0.07
	2*	88 ± 1	77 ± 1	-4.3 ± 1.4	-11.8 ± 3.9	6.5 ± 0.07
	3*	82 ± 1	77 ± 0.5	-1.3 ± 0.6	-3.6 ± 1.7	2.6 ± 0.07
	4*	76 ± 0.1	74 ± 0.5	-11.9 ± 5.1	-34.0 ± 14.7	0.9 ± 0.07
C2-10	1	97 ± 0.1	95 ± 0.5	-6.1 ± 2.1	-16.5 ± 5.7	1.2 ± 0.07
	2*	83 ± 2	66 ± 2	-3.3 ± 1.4	-9.2 ± 3.9	9.1 ± 0.07
	3*	75 ± 0.1	73 ± 0.5	-13.5 ± 6.0	-38.6 ± 17.1	1.0 ± 0.07
C2-5	1	106 ± 0.1	104 ± 0.5	-7.3 ± 3.2	-19.2 ± 8.4	1.3 ± 0.07
	2	73 ± 0.1	71 ± 0.5	-12.3 ± 5.8	-35.5 ± 16.6	1.1 ± 0.07
C-TBA	1	111 ± 0.1	109 ± 0.5	-10.6 ± 5.1	-27.5 ± 13.4	1.1 ± 0.07
	2	84 ± 0.1	82 ± 0.5	-13.8 ± 5.8	-38.7 ± 16.1	1.1 ± 0.07

For the DSC results for the second heating cycle in Figure 4.13, the three peaks associated with the mesophase transition of C-TEA, the mesophase transition of C-TBA, and the melting of C-TBA, are found at different temperatures when varying the stoichiometric ratio between the two end members. For samples in the TBAFeBrCl$_3$-rich region, C2-5, C2-10, and C2-15, it appears that the three peaks start to overlap more and more with increasing amounts of TEAFeBrCl$_3$. As the amount of TEAFeBrCl$_3$ reaches 25 mol%, only one peak can be observed, indicating either one phase transition or that the different transitions happen at approximately the same temperature. As the amount of TEAFeBrCl$_3$ increases further, a broader peak with a low intensity appears for the C2-50 and C2-75 samples. For the C2-75 sample, a sharp peak with a higher intensity also appears. Overlapping peaks were separated into single peaks using deconvolution, to be able to calculate values for each phase transition. An example of how this deconvolution was performed for the C2-10 sample is shown in Figure E.1 in Appendix E.

Figure 4.15 illustrates how the onset and end temperature for the phase transitions on heating in Table 4.4 change as a function of composition.
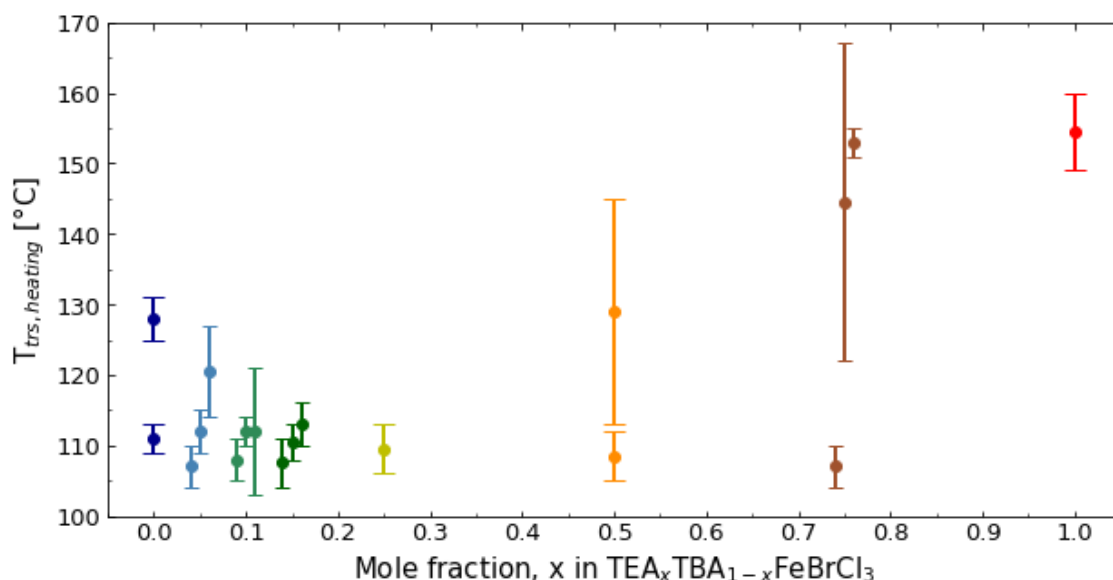
Figure 4.15: The onset and end temperature on heating for each phase transition as a function of composition for the $TEA_xTBA_{1-x}FeBrCl_3$ system. Each point represents a phase transition, where the lower bar is the onset temperature, and the upper bar is the end temperature. For samples with overlapping phase transitions, the values are separated by a small displacement along the x-axis, where the first transition is to the left and the last is to the right.

For the DSC results on cooling for the second thermal cycle in Figure 4.14, an equal number of peaks as seen on heating was expected for each sample. However, for multiple samples, there is either an increase or a decrease in the number of peaks on cooling compared to on heating. For sample C2-15 and C2-50, the DSC results even indicate that four peaks are present, making it difficult to establish which peak represents which phase transition. By comparing values in Table 4.4 and 4.5, one can see that the FWHM on cooling is generally smaller than on heating, indicating that the phase transitions on cooling take place more rapidly than on heating. A thermal hysteresis of a few degrees can be observed between the heating and cooling onset temperatures of each phase transition.

The three heating and cooling cycles measured by DSC between -25 and 200 °C for sample C2-10 and C2-50 are shown in Figure 4.16 and 4.17. On heating, the three cycles look quite similar for most samples. However, for some samples, such as sample C2-10, a difference in the shape of the peaks between the first and the second cycle is observed. On cooling, a shift in the onset temperature for phase transitions is commonly seen in all samples. For some samples, such as sample C2-50, a difference in the shape of the peaks can also be observed. This change in the peak shape between the first and second cycle on both heating and cooling may indicate that phase separation occurs due to the slow cooling rate during annealing of the samples in the calcination oven. The results for the other samples, except sample C2-TBA, are given in Figures F.1-F.6 in Appendix F.
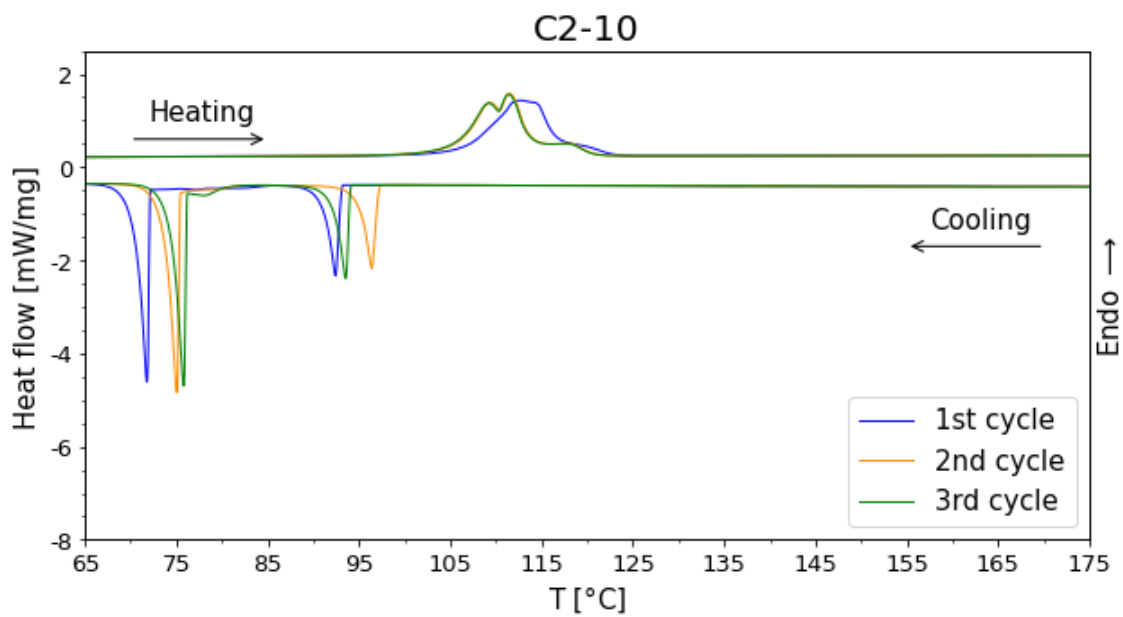
Figure 4.16: Heat flow as a function of temperature for three thermal cycles for the C2-10 sample, which contains 10 mol% TEAFeBrCl$_3$.
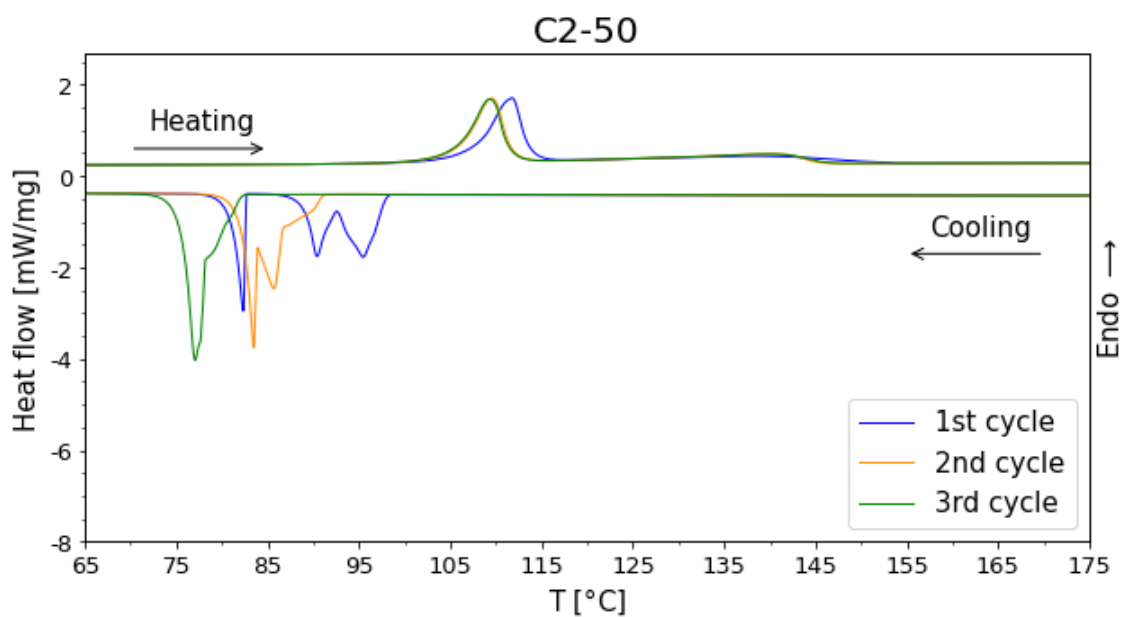

Figure 4.17: Heat flow as a function of temperature for three thermal cycles for the C2-50 sample, which contains 50 mol% TEAFeBrCl$_3$.

4.5 Effect of annealing on the crystal structure of TBAFeBrCl$_3$

Both samples of TBAFeBrCl$_3$, C-TBA and C2-TBA, were analysed using XRD to learn how the annealing at 220 °C for 2 h affected the crystal structure, and the results are shown in Figure 4.18. There is a change in the background intensity of the C2-TBA sample after annealing, especially at lower 2θ-values. This change in the background intensity may indicate that TBAFeBrCl$_3$ becomes less crystalline after annealing. However, it is not possible to calculate the amount of crystallinity with the XRD data shown here. A similar change in the background is observed for the samples in the TBAFeBrCl$_3$-rich region, which can be seen in Figures G.1-G.4 in Appendix G.
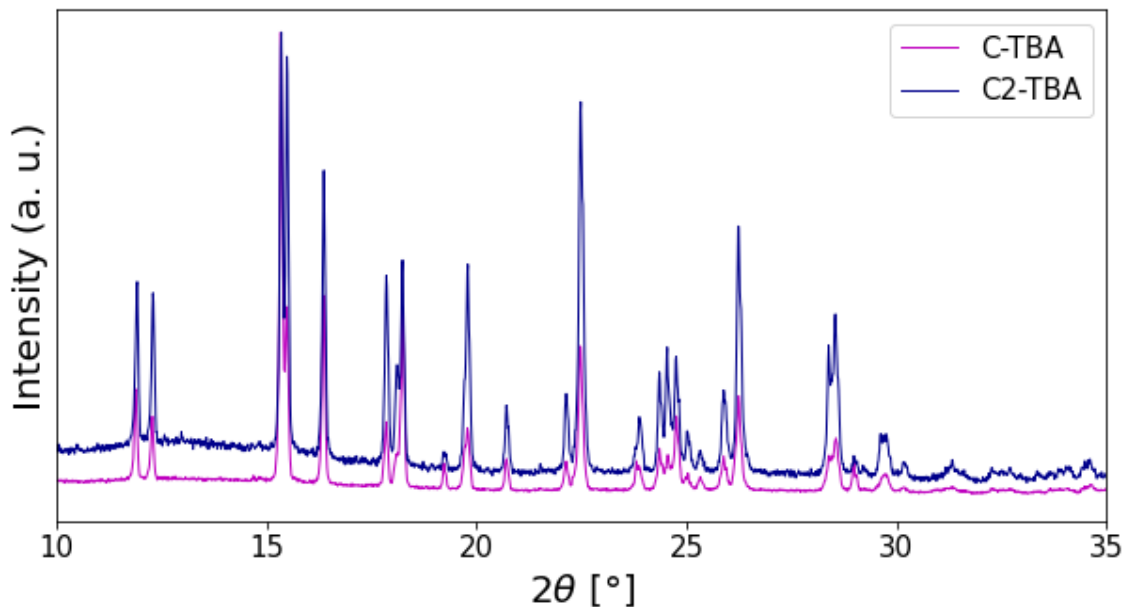

Figure 4.18: X-ray diffractograms of C-TBA and C2-TBA. Both samples are TBAFeBrCl$_3$, but only the C2 sample is annealed at 220 °C. Both diffractograms are normalised, giving relative intensities.

To confirm if the annealed TBAFeBrCl$_3$, C2-TBA, has a lower crystallinity than the as crystallised TBAFeBrCl$_3$, C-TBA, DSC was used to find the enthalpy of melting for C2-TBA and C-TBA in Figure 4.13, which is given in Table 4.4. The enthalpy of melting for the C-TBA compound is about 8.0 kJ/mol, and for the C2-TBA compound, it is about 6.5 kJ/mol. By assuming the C-TBA sample is 100% crystalline, equation (4) was used to calculate that the relative crystallinity of C-TBA is about 18.5% higher than for C2-TBA. Consequently, annealing of the TBAFeBrCl$_3$ compound results in some parts of the sample becoming amorphous. However, most of the sample remains crystalline, which is confirmed by the defined peaks in the diffractogram of sample C2-TBA. A similar difference in the intensity of the background was observed for compounds in the TBAFeBrCl$_3$-rich region, C2-5, C2-10, C2-15, and C2-25, and changes in the relative crystallinity may also be an explanation for these compounds.

5 Discussion

5.1 Crystal structure as a function of composition

The aim of increasing the understanding of the relationship between the composition of the $TEA_xTBA_{1-x}FeBrCl_3$ system and the crystal structure was achieved, and can be understood from the diffractograms in Figure 4.7. In this figure, the presence of diffraction lines belonging to both the $P6_3mc$ and $Pnna$ phase for all materials in the $TEA_xTBA_{1-x}FeBrCl_3$ system, and the almost unnoticeable shift in the peak positions, indicate little to no solid solution formation between the two end member materials. If a substitutional solid solution is formed between $TEAFeBrCl_3$ and $TBAFeBrCl_3$, it is expected that TEA^+ will substitute TBA^+, as TEA^+ is the smaller cation of the two [37, 42]. Thus, a larger cation is substituted by a smaller one, resulting in a compressed unit cell. When the lattice parameters decrease, the peak positions are shifted to higher 2θ-values [24, 65]. Therefore, the final diffractogram of a solid solution should mainly include diffraction lines from the solvent crystal structure [37, 42], which is expected to be $TBAFeBrCl_3$, with a slight shift in the peak positions due to the changes in the unit cell [24, 65]. As this is not observed for any of the samples in Figure 4.7, no clear solid solution formation occurs at room temperature. The results from Rietveld refinement of the $TEA_xTBA_{1-x}FeBrCl_3$ compounds in Table 4.3, supports the information retrieved from the X-ray diffractograms. Both end member material phases, $P6_3mc$ and $Pnna$, are present in all the analysed compositions in the $TEA_xTBA_{1-x}FeBrCl_3$ system, meaning no new crystallographic phases were observed in the system.

Even though no clear solid solution formation is observed between the two end member materials, there still might be some solubility of $TEAFeBrCl_3$ in $TBAFeBrCl_3$. However, it is difficult to quantify how much from the data retrieved during this project. In Figure 4.9, the small changes in the lattice parameters of the $P6_3mc$ and $Pnna$ phases as a function of composition may stem from this limited solubility of one end member material into the other. As the lattice parameters increase or decrease, the unit cell is expanded or compressed respectively, in the corresponding direction [24, 65].

The GOF-value varies as a function of composition, as shown in Figure 4.10. Figures A.1-A.4 in Appendix A show that there is a larger mismatch between the observed and calculated intensities for samples containing more $TEAFeBrCl_3$. Hence, this mismatch between the intensities is the explanation for the increase in the GOF-value. This intensity mismatch most likely stems from imperfect atomic positions in the structural model. The structural model for $TEAFeBrCl_3$ [16, 18] include atomic positions that are not suitable for refinement of atomic positions, making it difficult to decrease the GOF-value further. Thus, synchrotron data are needed to improve the structural model, which might result in a GOF-value closer to 1. In-situ powder XRD [66] have been conducted at the Swiss Norwegian Beam Lines (SNBL), beam line BM01, European Synchrotron Radiation Facility (ESRF), to analyse samples with varying composition in the $TEA_xTBA_{1-x}FeBrCl_3$ system. However, it was not part of the master's thesis to analyse synchrotron data. Another plausible explanation for the intensity mismatch is preferred orientation of the $TEAFeBrCl_3$-powder. When nonuniform particles are packed into a sample holder, the individual particles may have a preferred orientation in specific directions [67]. Non-random orientation of the particles result [68], and the intensity of diffraction lines corresponding to the preferred orientation directions will increase. For $TEAFeBrCl_3$, C-TEA, the intensity mismatch was the largest for the (010), (002), and (012) diffraction lines. To account for some of the preferred orientation during Rietveld

refinement, the preferred orientation of (010) and (002) was refined, but this was not enough to remove all of the intensity mismatch.

5.2 Thermodynamic properties as a function of composition

The aim of getting an understanding of the relationship between the composition of the $TEA_xTBA_{1-x}FeBrCl_3$ system and thermodynamic properties such as the phase transition temperature, enthalpy, and entropy, was achieved by analysing DSC results for the second heating cycle and synchrotron XRD data [66]. This will be presented by discussing the phase diagram of the system, the potential in thermal energy storage, and phase separation after annealing.

5.2.1 Constructing an approximate phase diagram

Based on the DSC data of the second heating cycle and the synchrotron XRD data [66], a phase diagram was constructed for the $TEA_xTBA_{1-x}FeBrCl_3$ system [51, 53, 57, 58], which has not been done before. Figure 5.1 illustrates this proposed phase diagram. The solid lines are estimated from the onset temperatures of the phase transitions, which are given in Table 4.4, and the dashed line is estimated from the literature value of the melting point of $TEAFeBrCl_3$ in argon at 281 °C [21].

Each peak in the DSC curves in Figure 4.13 represents a phase transition, and can therefore represent a new phase forming in the system. Hence, the first step to construct the phase diagram was to determine which phase transition corresponded to which peak in the DSC curves. In the temperature range analysed, which was -25 to 200 °C, $TEAFeBrCl_3$ goes through a mesophase transition, and $TBAFeBrCl_3$ goes through a mesophase transition and melting. Thus, it was originally believed that each peak in the DSC curves represented one of the three transitions the end members go through in the analysed temperature range. As some peaks overlap and the number of peaks vary between samples, it was difficult to determine what transition each peak represented from DSC data alone, and synchrotron XRD measurements [66] were used to determine the phase transitions.

At room temperature, XRD diffractograms of $TEA_xTBA_{1-x}FeBrCl_3$ samples with x = 0.05, 0.1, 0.15, 0.25, 0.5, and 0.75, showed little to no solid solution formation between the end member materials, resulting in phase separation between the $P6_3mc$ phase of $TEAFeBrCl_3$ and the $Pnna$ phase of $TBAFeBrCl_3$ in the lower part of the phase diagram. However, as each sample is heated during the DSC measurements, various phase transitions are observed.
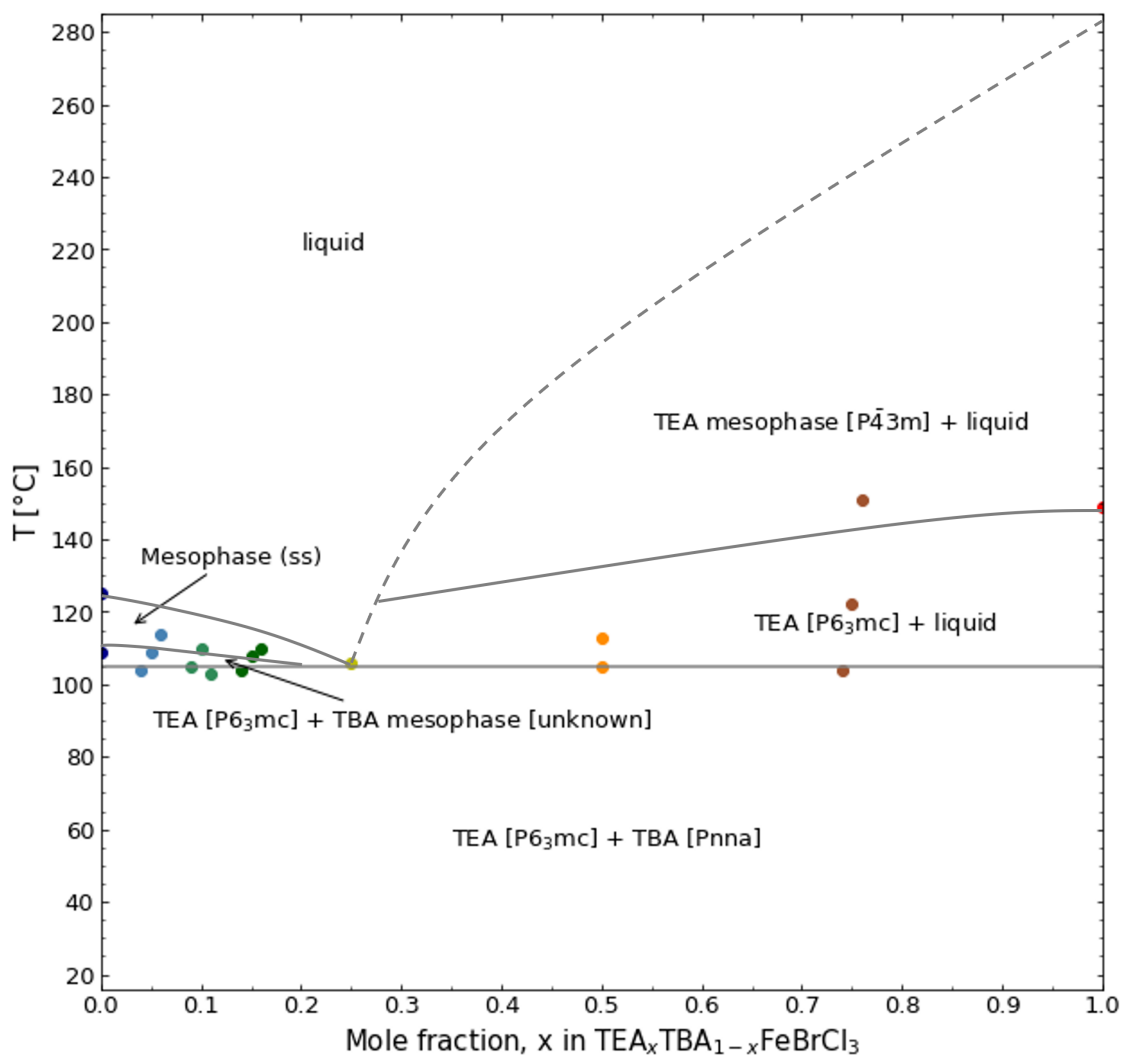
Figure 5.1: Phase diagram of the $TEA_xTBA_{1-x}FeBrCl_3$ system, estimated from the analysis of samples with x = 0, 0.05, 0.1, 0.15, 0.25, 0.5, 0.75, and 1. The onset temperatures of the phase transitions for samples with varying composition are marked as points, and the lines are drawn by hand to follow these approximately. The solid, grey lines are estimated from measurement data, and the dashed, grey line is estimated from the literature, where $TEAFeBrCl_3$ is found to melt at 281 °C in argon [21]. TEA and TBA indicate that the phase belongs to $TEAFeBrCl_3$ and $TBAFeBrCl_3$, respectively. The space group of the phase is given in brackets.

For samples in the $TBAFeBrCl_3$-rich region of the phase diagram, C2-5, C2-10, and C2-15, three overlapping peaks are observed in the DSC curves in Figure 4.13. Synchrotron XRD measurements [66] show that the first peak represents the mesophase transition of $TBAFeBrCl_3$, the second peak represents a transition to a miscible mesophase region, and the third peak represents the melting of the homogeneous mesophase. As the mesophase transition of $TBAFeBrCl_3$ occurs at a lower temperature that the other end member phase transitions [19, 21], and these three samples contain larger amounts of $TBAFeBrCl_3$ than $TEAFeBrCl_3$, it seems reasonable that this is the first phase transition. Most plastic crystal phases have a highly symmetric hexagonal or cubic crystal structure [13], and it is therefore likely that the mesophase of $TBAFeBrCl_3$ has the same cubic $P\bar{4}3m$ symmetry (no. 215) as the mesophase of $TEAFeBrCl_3$ [18]. The formation of a region of solubility

in the mesophase is the only region of solubility in the $TEA_xTBA_{1-x}FeBrCl_3$ system. When the temperature increases, the solid $P6_3mc$ phase of $TEAFeBrCl_3$ dissolve into the mesophase of $TBAFeBrCl_3$, thereby forming a solid solution. In the plastic crystal phase, the molecular assemblies are held together by weaker, non-covalent interactions [43]. Additionally, the local disorder and long-range order creates a phase that is in-between a liquid and a crystalline solid [12–14]. These characteristics of the mesophase may explain why solid solution formation is possible in this region, as the increased plasticity of the mesophase may allow the two structures to become miscible.

The sample containing 25 mol% $TEAFeBrCl_3$, C2-25, has one peak in the DSC curve in Figure 4.13. Synchrotron XRD measurements [66] show that this peak is related to direct melting of the sample on heating. In the phase diagram, this presents itself as a point similar to an eutectic melting point, where two solids are transformed directly into a liquid [57].

Samples with more than 25 mol% $TEAFeBrCl_3$, C2-50 and C2-75, go through two phase transitions on heating according to synchrotron XRD results [66], and these phase transitions are illustrated in the phase diagram. According to the DSC results in Figure 4.13, C2-75 goes through three phase transitions instead of two, but as the second peak in the DSC curve is really broad and difficult to define, it is not taken into account when drawing the lines in the final phase diagram. During the first phase transition, the $Pnna$ phase of $TBAFeBrCl_3$ melts and forms a liquid around the solid $P6_3mc$ phase of $TEAFeBrCl_3$. As there is no solubility between the solid and liquid phase, two phases result. For the second phase transition, the $P6_3mc$ phase of $TEAFeBrCl_3$ goes through a mesophase transition to the $P\bar{4}3m$ phase [18], which is also not soluble in the liquid phase. C2-50 and C2-75 contain large amounts of $TEAFeBrCl_3$, making the observed phase separations reasonable. The amount of liquid, which stems from $TBAFeBrCl_3$, was potentially too small for the solid and plastic crystal phase of $TEAFeBrCl_3$ to dissolve in it, thereby resulting in two phases.

5.2.2 Use of $TEA_xTBA_{1-x}FeBrCl_3$ materials in thermal energy storage

To determine if $TEA_xTBA_{1-x}FeBrCl_3$ materials are suitable for latent heat TES systems, the onset and end temperature, enthalpy, and entropy, for the second thermal cycle on heating and cooling in Table 4.4 and 4.5 respectively, and the phase diagram in Figure 5.1, can be studied. The main requirement for a latent heat TES material is that it goes through a reversible endothermic phase transition on heating within the temperature range of operation, that is accompanied by a large change in the enthalpy and entropy [2, 6, 8–10]. From the phase diagram, almost all the materials in the $TEA_xTBA_{1-x}FeBrCl_3$ system, except the one with x = 0.25, go through one or multiple reversible mesophase transitions on heating. These transitions are accompanied by a high enthalpy and entropy change, as shown in Table 4.4, which seems promising for TES systems. Additionally, by comparing the onset temperatures in Table 4.4 and 4.5, these transitions are accompanied by a temperature hysteresis between heating and cooling, which is desired for TES materials [2, 6, 9, 10]. Consequently, one would assume most of the $TEA_xTBA_{1-x}FeBrCl_3$ materials with varying compositions may be useful as latent heat TES materials. However, samples that include 25 mol% or more $TEAFeBrCl_3$ melt around 105 °C, which is not ideal for TES systems. Also, as little to no solid solution formation occurs between the two end member materials at room temperature, the possibility of tuning the thermal properties connected to the phase transitions is limited. Thus, the $TEA_xTBA_{1-x}FeBrCl_3$ materials are most likely not the next promising latent heat TES materials.

5.2.3 Phase separation after annealing

The peak shape of some samples, such as C2-10 and C2-50, varied between the first and second thermal cycle during DSC measurements, as shown in Figure 4.16 and 4.17. According to the constructed phase diagram in Figure 5.1, all samples in the $TEA_xTBA_{1-x}FeBrCl_3$ system will melt or become a mixture of a liquid and a mesophase at the annealing temperatures used to promote solid solution formation. The cooling rate after the annealing is very slow, resulting in equilibrium cooling, which allow the phases to crystallise separately, as enough time is spent at each temperature for the phase compositions to be adjusted [57]. When the samples are heated and cooled during the DSC measurements, the heating and cooling rates are 10 °C/min. Thus, the cooling rate during the DSC measurements is much faster than during annealing, and non-equilibrium cooling will most likely occur. The outer part of the sample will be cooled and crystallise first, and the inner part of the sample last. Hence, phase transitions will occur at other temperatures than what is expected in the phase diagram based on slower cooling rates, and non-equilibrium phases will exist at room temperature, that are not shown in this phase diagram based on slower cooling rates [57, 69, 70]. The difference between the first and second thermal cycle during DSC measurements is most likely due to the variation in the cooling rate of the sample, as this parameter affects the composition of the end product and at which temperature phase transitions will occur. However, moisture and non-evaporated solvent may also influence the first thermal cycle. The results of the third thermal cycle are more similar to the second cycle. This may be due to the cooling rates being the same between these cycles, or the removal of moisture and non-evaporated solvent through evaporation.

5.3 Suggestions as to why solid solution formation did not occur at room temperature

To investigate the reason as to why the two end member materials did not form solid solutions, the molecular size of the TEA^+ and TBA^+ cations were reviewed in VESTA [47] using the CIF file for the $P6_3mc$ phase of $TEAFeBrCl_3$ [16], and for the $Pnna$ phase of $TBAFeBrCl_3$ [17, 48]. By assuming that the bond angles and the shape of the molecule is rigid, and that the cation is spherical, the cation size can be estimated. An approximate cation radius of 2.54 Å was found for TEA^+, and 5.09 Å for TBA^+. This gives a size difference of about 50% between the two cations. A rule of thumb is that when the size difference between the ions is more than ~30%, no substitutional solid solutions are expected to form [37]. As the size difference estimated from VESTA is larger than this, the size difference between TEA^+ and TBA^+ is a plausible explanation as to why little to no solid solution formation occurs at room temperature.

The values of the cation radius estimated from VESTA may be inaccurate, and the size difference between the two cations may be smaller than the calculated value above. In the literature, TEA^+ has an ionic radii of 3.85 Å [71], which is about 51.6 % larger than the value from VESTA (2.54 Å). No literature value for the ionic radii of TBA^+ was found, making it difficult to calculate the ionic size difference based on more accurate values. Even though the ionic size difference may not be as large as about 50%, this is still the most likely reason as to why little to no solid solution formation occurred between the two end member materials.

5.4   Synthesis observations

The aim of synthesising hybrid organic-inorganic plastic crystals of tetraethylammonium and tetrabutylammonium bromotrichloroferrate(III) using a water-based evaporation crystallisation was achieved, with a yield of 96.4% for the TEAFeBrCl$_3$ crystals, and 87.6% for the TBAFeBrCl$_3$ crystals.

The high yield of TEAFeBrCl$_3$ and TBAFeBrCl$_3$ is most likely a result of using evaporation crystallisation. During this method, the precursor solution is left in one container until almost all the solvent has evaporated and crystals have precipitated. Consequently, loss of product related to, for instance, changing the container during the synthesis, is minimised. Non-evaporated solvent or impurities may have contributed to the yield being higher than it is in reality, but it is difficult to quantify how much each contribute to the final yield. By vacuum filtrating and drying the final crystals, the contribution of non-evaporated solvent to the yield should be minimised [26]. However, the final crystals were not washed. When washing crystals, surface impurities are removed, but the crystals can dissolve in the washing liquid [26]. Thus, the final yield may include some surface impurities, but no crystal product was lost to washing.

An explanation as to why the yield of TEAFeBrCl$_3$ was about 9% higher than for TBAFeBrCl$_3$, may be that more of the solution had evaporated from the crystalliser with TEAFeBrCl$_3$ compared to the one with TBAFeBrCl$_3$. Consequently, more precursor solution was removed from the TBAFeBrCl$_3$ crystals during vacuum filtration. Nucleation and growth of crystals from solution will continue until equilibrium conditions are reached for the supersaturation [27, 28]. Hence, further nucleation and growth of TBAFeBrCl$_3$ was most likely hindered when some precursor solution was filtered away. To ensure minimal loss of product, more of the solvent should be left to evaporate before vacuum filtration. However, it can be difficult to work with crystals that are all dried up, and some loss of precursor solution is thereby expected. The decanted precursor solution can be left to crystallise further, thereby ensuring more product.

While the evaporation crystallisation process for both TEAFeBrCl$_3$ and TBAFeBrCl$_3$ was slow and took place over several days, it was not controlled enough to maintain a low degree of supersaturation. The high nucleation rate due to the high degree of supersaturation resulted in the formation of mostly smaller crystals instead of larger monocrystals [23, 27].

5.5   Effect of annealing temperature

For TEA$_x$TBA$_{1-x}$FeBrCl$_3$ samples with x = 0.25, 0.5, and 0.75, a larger mass loss and more residue on the sides of the containers were observed when annealing at 240 °C compared to at 220 °C. The higher mass loss at 240 °C may indicate some degradation of the compounds. The thermal stability of a compound decreases when increasing the length of the carbon chain [45], meaning if any degradation occurred, TBAFeBrCl$_3$ will start to degrade before TEAFeBrCl$_3$. This is confirmed by Wyrzykowski et al. [19, 21], that found the decomposition temperature of TEAFeBrCl$_3$ and TBAFeBrCl$_3$ in argon to be 295 °C and 255 °C, respectively. Hence, the overshooting of the annealing temperature to 264 °C when it was set to 240 °C most likely made the decomposition of TBAFeBrCl$_3$ possible.

As amorphous materials have a more irregular arrangement of atoms, ions, or molecules than crystalline materials, broader and less defined peaks are expected in XRD

diffractograms of less crystalline materials [72]. Both $TEA_{0.5}TBA_{0.5}FeBrCl_3$ annealed at 240 °C and 220 °C are mainly crystalline, as sharp peaks are observed. Additionally, the peak positions do not change much between the two materials, meaning no secondary phases or significant structural changes are formed during the different annealing temperatures [65, 73]. However, the higher background intensity for the $TEA_{0.5}TBA_{0.5}FeBrCl_3$ compound annealed at 240 °C may indicate that the compound becomes less crystalline at the higher annealing temperature, as this adjustment in the intensity can stem from broadening of the peaks [72].

Even though the mass loss and residue on the glass containers at 220 °C was less than at 240 °C, these observations are still made at the lower annealing temperature. When comparing the phase transition temperature for the mesophase transition of $TEAFeBrCl_3$, Walker et al. [18] found that this transition occurs at 149 °C in synthetic air, and Wyrzykowski et al. [21] found it occurs at 161 °C in argon. Thus, the thermal properties can vary in different environments. When the $TEA_xTBA_{1-x}FeBrCl_3$ samples were annealed in air, the oven overshot the temperature to about 246 °C. The decomposition temperature of 255 °C for $TBAFeBrCl_3$ is determined in argon [19], and is most likely lower in air than in the inert atmosphere. Therefore, some degradation may have occurred at the lower annealing temperature as well, but more degradation was observed for the higher annealing temperature.

By comparing the XRD diffractograms of the non-annealed and annealed $TBAFeBrCl_3$ in Figure 4.18, a difference in the background intensity is observed, with the annealed $TBAFeBrCl_3$ having a higher background intensity than the non-annealed. From DSC measurements, it was found that the annealed sample is about 18.5% less crystalline than the non-annealed one, which supports that some degradation of $TBAFeBrCl_3$ occurs at the lower annealing temperature.

Even though the annealed $TBAFeBrCl_3$ is less crystalline, this sample has a lower GOF-value of 1.73 than the non-annealed $TBAFeBrCl_3$, which has a GOF-value of 3.49. In Figure A.9 and A.8, the difference in the GOF-value looks like it stems from an intensity mismatch between calculated and measured XRD data, which is larger for the non-annealed sample. This intensity mismatch may be due to imperfect atomic positions in the structural model [17, 48], making it difficult to fit the structure during Rietveld refinement. As the annealed $TBAFeBrCl_3$ has a better fit, this sample is most likely more similar to the structural model than the non-annealed $TBAFeBrCl_3$. Therefore, synchrotron data are needed to improve the structural model of $TBAFeBrCl_3$, which might result in a lower GOF-value for the non-annealed sample. Preferred orientation of the packed $TBAFeBrCl_3$-powder can also be an explanation of the intensity mismatch. When $TBAFeBrCl_3$ is annealed and crushed into a fine powder for a second time, the preferred orientation of the packed powder may decrease as the particles become more uniform, thereby resulting in a lower GOF-value for the annealed sample.

6   Conclusion

The end member materials, TEAFeBrCl$_3$ and TBAFeBrCl$_3$, were synthesised from a water-based evaporation crystallisation with a yield of 96.4% and 87.6%, respectively. The resulting crystals were mostly small in size, which indicates a high nucleation rate during the crystallisation process. A synthesis route for materials with a composition of TEA$_x$TBA$_{1-x}$FeBrCl$_3$, with x = 0.05, 0.1, 0.15, 0.25, 0.50, and 0.75, was developed. During the annealing process, TBAFeBrCl$_3$ most likely degraded, as DSC measurements show a reduction in the crystallinity of 18.5% after annealing, and XRD measurements show changes in the intensity of the background.

According to XRD measurements and Rietveld refinement of TEA$_x$TBA$_{1-x}$FeBrCl$_3$ compounds, no clear solid solution formation occurs at room temperature, as both *P6$_3$mc* and *Pnna* phases are present in all compounds. While no solid solution formed, small changes in the lattice parameters can be observed as a function of mole fraction TEAFeBrCl$_3$, which indicates some solubility of one end member material into the other. The most likely reason why little to no solid solution formation occurred between the two end members materials, is that the size difference between TEA$^+$ and TBA$^+$ is too large to favour substitutional solid solution formation.

A proposed phase diagram was constructed from values retrieved from DSC measurements, with the help of in-situ XRD synchrotron measurements [66] to determine the phase composition. It was confirmed that no solid solution occurred at room temperature, resulting in phase separation. Even though this is the case, changes in the phase transition temperature, enthalpy, and entropy are observed on heating the compounds, indicating some relationship between these values and the ratio of each end member. In the TBAFeBrCl$_3$-rich region, with less than 25 mol% TEAFeBrCl$_3$, a region of solubility is observed in the mesophase. For samples with more than 25 mol% TEAFeBrCl$_3$, on the other hand, TBAFeBrCl$_3$ melts directly, creating a liquid TBAFeBrCl$_3$ phase and a solid TEAFeBrCl$_3$ phase. Due to this melting, TEA$_x$TBA$_{1-x}$FeBrCl$_3$ materials are not that promising as TES materials. However, this system still shows interesting properties, such as the miscible mesophase region, that would be fascinating to study further to get a better understanding of how composition affects the mesophase in plastic crystal systems. Maybe this miscible region will be useful in some future applications.

7 Further work

To further increase the knowledge about how the crystal structure and thermodynamic properties change as a function of composition for the $TEA_xTBA_{1-x}FeBrCl_3$ materials, more compounds in the system can be synthesised and analysed using the same methods as described in this project. It would be especially interesting to analyse more compounds in the $TBAFeBrCl_3$-rich region, to better understand the solid solution formation of the mesophase, as how the composition affects the mesophase in plastic crystals is not clearly understood yet. Additionally, by analysing multiple compounds with more than 25 mol% $TEAFeBrCl_3$, the right side of the phase diagram can be more accurately represented. By subjecting the samples to a maximum temperature above the melting temperature of $TEAFeBrCl_3$ during DSC measurements, one can draw the dashed line in the phase diagram based on measurement data instead of literature values.

In-situ X-ray diffraction synchrotron measurements [66] have been conducted on the $TEA_xTBA_{1-x}FeBrCl_3$ materials, but as it was not part of this master's thesis to analyse the data, they should be analysed in detail in the future. As a result, a better understanding of how the crystal structure change as a function of temperature can be achieved. Consequently, the crystal structure and space group of each phase presented in the constructed phase diagram of the system can be found. Additionally, it would be interesting to press polycrystalline samples of the $TEA_xTBA_{1-x}FeBrCl_3$ materials and measure electrical properties, such as dielectric and ferroelectric, to better understand the functional properties of these materials, which may open up for possible applications.

While it would be interesting to study the $TEA_xTBA_{1-x}FeBrCl_3$ materials further, they would probably not help in the further development of many applications, such as TES systems. These materials form little to no solid solutions at room temperature, making large changes in properties such as the phase transition temperature, enthalpy, and entropy difficult, which may prevent sufficient tuning of properties for use in specific TES applications. Also, the $TBAFeBrCl_3$ end member has a low melting temperature, and this melting temperature seems to influence the melting point of samples with varying compositions in the system. This makes it difficult to continue research of $TEA_xTBA_{1-x}FeBrCl_3$ materials for TES applications, as melting is generally not desired. Hence, systems with end member materials with higher melting points and solid solution formation should be studied instead. Hopefully, these systems also have a region of solubility in the mesophase that would be interesting to look further into. By studying multiple systems with this region, one may be able to understand why and how it appears. Ultimately, determining whether and how it can be exploited in applications.

Bibliography

[1] E. Eknes, 'Engineering plastic crystal ferroics for energy applications', *Material Science Specialization Project, NTNU*, pp. 9–11, 2021.

[2] J. S. Beceiro, 'Hybrid organic-inorganic materials with phase transitions for solid-state cooling and solar thermal energy storage', *Doctoral Thesis, Universidade Da Coruña*, pp. 1–40, 2021.

[3] IEA. 'Heating'. (2022), [Online]. Available: https : / / www . iea . org / fuels - and - technologies/heating (visited on 26th Apr. 2022).

[4] IEA. 'Cooling'. (2022), [Online]. Available: https : / / www . iea . org / fuels - and - technologies/cooling (visited on 26th Apr. 2022).

[5] C. Bussar, P. Stöcker, Z. Cai, L. Moraes Jr, D. Magnor, P. Wiernes, N. v. Bracht, A. Moser and D. U. Sauer, 'Large-scale integration of renewable energies and impact on storage demand in a european renewable power system of 2050—sensitivity study', *Journal of Energy Storage*, vol. 6, pp. 1–10, 2016. DOI: 10.1016/j.est.2016.02.004.

[6] J. Walker, 'Hybrid molecular materials for sustainable thermal energy storage (molytherm)', *Unpublished work, NTNU*, 2022.

[7] I. Dincer and M. Rosen, *Thermal Energy Storage for Sustainable Energy Consumption: Fundamentals, Case Studies and Design*, H. Ö. Paksoy, Ed. Dordrecht: Springer, 2007, ch. 2: Energetic, Exergetic, Environmental and Sustainability Aspects of Thermal Energy Storage Systems.

[8] R. A. Huggins, *Energy Storage: Fundamentals, Materials and Applications*. Switzerland: Springer, 2016, ch. 3: Thermal Energy Storage. DOI: 10.1007/978-3-319-21239-5.

[9] S. D. Sharma and K. Sagara, 'Latent heat storage materials and systems: A review', *Taylor and Francis*, vol. 2, no. 1, pp. 1–56, 2005. DOI: 10.1081/GE-200051299.

[10] E. Moreles, G. Huelsz and G. Barrios, 'Hysteresis effects on the thermal performance of building envelope pcm-walls', *Building Simulations*, vol. 11, no. 3, pp. 519–531, 2018. DOI: 10.1007/s12273-017-0426-4.

[11] M. Helbæk and S. Kjelstrup, *Fysikalsk kjemi*. Bergen: Fagbokforlaget Vigmostad & Bjærke AS, 2009, ch. 2.4.2: Prosesser ved konstant trykk, entalpi.

[12] J. Harada, 'Plastic/ferroelectric molecular crystals: Ferroelectric performance in bulk polycrystalline forms', *APL Materials*, vol. 9, no. 2, 2021. DOI: 10.1063/5.0039066.

[13] S. Das, A. Mondal and C. M. Reddy, 'Harnessing molecular rotations in plastic crystals: A holistic view for crystal engineering of adaptive soft materials', *Chemical Society Reviews*, vol. 49, no. 24, pp. 8878–8896, 2020. DOI: 10.1039/d0cs00475h.

[14] J. Timmermans, 'Plastic crystals: A historical review', *Journal of Physics and Chemistry of Solids*, vol. 18, no. 1, pp. 1–8, 1961. DOI: 10.1016/0022-3697(61)90076-2.

[15] S. Scherrer, 'Synthesis, structure and properties of the organic-inorganic plastic crystal solid solution system $[(CH_2CH_3)_4N]_x[(CH_3)_4N]_{1-x}[FeBrCl_3.]$', *Master's Thesis, der Technischen Universität Wien*, pp. 26–27, 2020.

[16] D. J. Evans, A. Hills, D. L. Hughes and G. J. Leigh, 'Structures of tetraethylammonium tetrachloroferrate(iii) and the mixed halide iron(iii) complex, $[NEt_4][FeBrCl_3]$', *Acta Crystallographica Section C Crystal Structure Communications*, vol. 46, no. 10, pp. 1818–1821, 1990. DOI: 10.1107/s0108270190001135.

[17] R. Kruszynski and D. Wyrzykowski, 'Tetrabutylammonium bromotrichloro-ferrate(iii)', *Acta Crystallographica Section E: Structure Reports Online*, vol. 62, no. 5, pp. 994–996, 2006. DOI: 10.1107/S1600536806012402.

[18] J. Walker, K. P. Marshall, J. Salgado-Beceiro, B. A. D. Williamson, N. S. Løndal, S. Castro-Garcia, M. S. Andújar, S. M. Selbach, D. Chernyshov and M.-A. Einarsrud, 'Mesophase transitions in $[(C_2H_5)_4N][FeBrCl_3]$ and $[(CH_3)_4N][FeBrCl_3]$ ferroic plastic crystals', *Chemistry of Materials*, vol. 34, no. 6, pp. 2585–2598, 2022. DOI: 10.1021/acs.chemmater.1c03778.

[19] D. Wyrzykowski, T. Maniecki, M. Gazda, E. Õ. Stycze and Z. Warnke, 'Thermal properties of tetrabutylammonium bromotrichloro-, tribromochloro- and tetrabromoferrates(iii)', *Journal of Thermal Analysis and Calorimetry*, vol. 90, no. 3, pp. 893–897, 2007. DOI: 10.1007/s10973-006-8207-9.

[20] A. H. King, 'Our elemental footprint', *Nature Materials*, vol. 18, pp. 408–409, 2019. DOI: 10.1038/s41563-019-0334-3.

[21] D. Wyrzykowski, A. Pattek-Janczyk, T. Maniecki, K. Zaremba and Z. Warnke, 'Thermal properties of tetraethylammonium tetrachloro-, bromotrichloro-and tribromochloroferrates(iii)', *Journal of Thermal Analysis and Calorimetry*, vol. 91, no. 1, pp. 279–284, 2008. DOI: 10.1007/s10973-006-8269-8.

[22] J. W. Mullin, *Crystallization*. Oxford: Butterworth-Heinemann, 2001, ch. 1: The crystalline state.

[23] S. Bandyopadhyay, *Fabrication and application of nanomaterials*. USA: McGraw-Hill Education, 2019, ch. 2: Nucleation.

[24] A. R. West, *Solid State Chemistry and its Applications*. United Kingdom: John Wiley & Sons Ltd, 2014, ch. 1: Crystal Structures and Crystal Chemistry.

[25] R. J. D. Tilley, *Understanding Solids: The Science of Materials*. United Kingdom: John Wiley & Sons Ltd, 2013, ch. 3.2.2: Crystalline solid.

[26] J. W. Mullin, *Crystallization*. Oxford: Butterworth-Heinemann, 2001, ch. 3: Solutions and solubility.

[27] S. Bandyopadhyay, *Fabrication and application of nanomaterials*. USA: McGraw-Hill Education, 2019, ch. 3: Crystal growth.

[28] G. Cao and Y. Wang, *Nanostructures and Nanomaterials: Synthesis, Properties, and Applications*. Singapore: World Scientific Publishing Co. Pte. Ltd., 2011, ch. 3.2.2: Subsequent growth of nuclei.

[29] J. W. Mullin, *Crystallization*. Oxford: Butterworth-Heinemann, 2001, ch. 5: Nucleation.

[30] J. W. Mullin, *Crystallization*. Oxford: Butterworth-Heinemann, 2001, ch. 6: Crystal growth.

[31] G. Cao and Y. Wang, *Nanostructures and Nanomaterials: Synthesis, Properties, and Applications*. Singapore: World Scientific Publishing Co. Pte. Ltd., 2011, ch. 2.2: Surface energy.

[32] D. W. Richerdson and W. E. Lee, *Modern Ceramic Engineering; Properties, Processing and Use in Design*. Boca Raton, FL: CRC Press, 2018, ch. 9.3.3: Solid-Solid Reactions.

[33] A. R. West, *Solid State Chemistry and its Applications*. United Kingdom: John Wiley & Sons Ltd, 2014, ch. 4.2: Solid State Reaction or Shake'n Bake Methods.

[34] R. Ropp, *Solid state chemistry*. Amsterdam: Elsevier, 2003, ch. 4: Mechanisms and Reactions in the Solid State.

[35] R. J. D. Tilley, *Understanding Solids: The Science of Materials*. United Kingdom: John Wiley & Sons Ltd, 2013, ch. 7: Diffusion and ionic conductivity.

[36] J. William D. Callister and R. David G., *Materials Science and Engineering SI Version*. China: John Wiley & Sons Ltd, 2015, ch. 7: Diffusion.

[37] A. R. West, *Solid State Chemistry and its Applications*. United Kingdom: John Wiley & Sons Ltd, 2014, ch. 2.3: Solid Solutions.

[38] D. W. Richerdson and W. E. Lee, *Modern Ceramic Engineering; Properties, Processing and Use in Design*. Boca Raton, FL: CRC Press, 2018, ch. 6.1.5.1: Solid Solution.

[39] M. Lusi, 'Engineering crystal properties through solid solutions', *Crystal Growth and Design*, vol. 18, no. 6, pp. 3704–3712, 2018. DOI: 10.1021/acs.cgd.7b01643.

[40] J. William D. Callister and R. David G., *Materials Science and Engineering SI Version*. China: John Wiley & Sons Ltd, 2015, ch. 6.4: Impurities in solids.

[41] R. J. D. Tilley, *Understanding Solids: The Science of Materials*. United Kingdom: John Wiley & Sons Ltd, 2013, ch. 3.4: Point defects.

[42] D. W. Richerdson and W. E. Lee, *Modern Ceramic Engineering; Properties, Processing and Use in Design*. Boca Raton, FL: CRC Press, 2018, ch. 5.2.2: Crystal Chemical Substitution.

[43] L. F. Lindoy and I. M. Atkinson, *Self-Assembly in Supramolecular systems*. Cambridge: The Royal Society of Chemistry, 2000, ch. 1: Self-assembly: What Does it Mean?

[44] T. W. G. Solomons, C. B. Fryhle and S. A. Snyder, *Solomons' Organic Chemistry*. Singapore: John Wiley & Sons Ltd, 2016, ch. 20.2: Physical Properties and Structure of Amines.

[45] S. Yoshida and H. Ishida, 'The effect of chain length on the thermal stability of 2-alkylimidazoles on copper and 2-alkylimidazolato copper(ii) complexes', *Applications of Surface Science*, vol. 20, no. 4, pp. 497–511, 1985. DOI: 10.1016/0378-5963(85)90170-9.

[46] J. Walker, K. Marshall, B. Williamson, S. Scherrer, I. Holch, D. Chernyshov, T. Bayer, S. M. Selbach, T. Rojac and M.-A. Einarsrud, 'Electromechanical properties of hexagonal tetraethylammonium bromotrichloroferrite(iii) plastic crystals', *Unpublished work, NTNU*, 2022.

[47] K. Momma and F. Izumi, 'Vesta 3 for three-dimensional visualization of crystal, volumetric and morphology data', *Journal of Applied Crystallography*, vol. 44, pp. 1272–1276, 2011. DOI: 10.1107/S0021889811038970.

[48] R. Kruszynski and D. Wyrzykowski. 'Crystallographic open database: Information card for entry 2208805'. (2006), [Online]. Available: http://www.crystallography.net/cod/2208805.html (visited on 6th Apr. 2022).

[49] D. Wyrzykowski, R. Kruszyński, U. Kucharska and Z. Warnke, 'Structural and physicochemical characteristics of tetrabutylammonium tetrahalogenoferrates(iii), $[(C_4H_9)_4N][FeBr_{4-n}Cl_n]$', *Zeitschrift fur Anorganische und Allgemeine Chemie*, vol. 632, no. 4, pp. 624–628, 2006. DOI: 10.1002/zaac.200500472.

[50] G. Höhne, W. F. Hemminger and H. J. Flammersheim, *Differential scanning calorimetry*. Berlin: Springer, 2003, ch. 1: Introduction.

[51] M. Sorai, *Comprehensive handbook of calorimetry and thermal analysis*. Chichester: Wiley, 2004, ch. 2.3: Principles and methods of thermal analysis.

[52] G. Höhne, W. F. Hemminger and H. J. Flammersheim, *Differential scanning calorimetry*. Berlin: Springer, 2003, ch. 2.2: Power Compensation DSC.

[53] A. R. West, *Solid State Chemistry and its Applications*. United Kingdom: John Wiley & Sons Ltd, 2014, ch. 6.4: Thermal Analysis (TA).

[54] L. C. Thomas, 'Modulated dsc® paper #8 use of quasi-isothermal mode for improved understanding of structure change', *TA Instruments*, p. 1, 2005. [Online]. Available: http://www.tainstruments.com/pdf/literature/TP_013_MDSC_num_8_Quasi-Isothermal_Mode_for_Improved_Understanding_of_Structure_Change%5C%20.pdf (visited on 4th Apr. 2022).

[55] M. Helbæk and S. Kjelstrup, *Fysikalsk kjemi*. Bergen: Fagbokforlaget Vigmostad & Bjærke AS, 2009, ch. 3.1: Tolkning av begrepet entropi på mikroskopisk nivå.

[56] S. Chapi, R. S and D. H, 'Enhanced electrochemical, structural, optical, thermal stability and ionic conductivity of (peo/pvp) polymer blend electrolyte for electrochemical applications', *Inonics*, vol. 22, no. 6, pp. 803–814, 2015. DOI: 10.1007/s11581-015-1600-2.

[57] J. William D. Callister and R. David G., *Materials Science and Engineering SI Version*. China: John Wiley & Sons Ltd, 2015, ch. 11: Phase diagrams.

[58] M. Kaye, K. Jaansalu and W. T. Thompson, 'Phase equilibrium in metallic systems', *Canadian Metallurgical Quarterly*, vol. 42, no. 4, pp. 393–410, 2003. DOI: 10.1179/cmq.2003.42.4.393.

[59] S. Stølen and T. Grande, *Chemical Thermodynamics of Materials: Macroscopic and Microscopic Aspects*. New York: John Wiley & Sons Ltd, 2004, ch. 2.1: Phases, phase transitions and phase diagrams.

[60] R. J. D. Tilley, *Understanding Solids: The Science of Materials*. United Kingdom: John Wiley & Sons Ltd, 2013, ch. 8: Phase transformations and reactions.

[61] J. Perl, J. Shin, J. Schumann, B. Faddegon and H. Paganetti, 'TOPAS: An innovative proton Monte Carlo platform for research and clinical applications', *Medical Physics*, vol. 39, p. 6818, 2012. DOI: 10.1118/1.4758060.

[62] B. Faddegon, J. Ramos-Mendez, J. Schuemann, A. McNamara, J. Shin, J. Perl and P. H., 'The TOPAS Tool for Particle Simulation, a Monte Carlo Simulation Tool for Physics, Biology and Clinical Research', *Physica Medica*, 2020. DOI: 10.1016/j.ejmp.2020.03.019.

[63] G. Esteves, K. Ramos, C. M. Fancher and J. L. Jones, 'Lipras: Line-profile analysis software', 2017. DOI: 10.13140/RG.2.2.29970.25282/3.

[64] I. E. Holck, 'Synthesis and characterisation of the plastic crystal solid solution systems $[(CH_3)_4N]_x[(CH_3CH_2)_4N]_{1-x}[FeBrCl_3]$ (x = 0.7 - 1)', *Master's thesis in Nanotechnology, NTNU*, p. 19, 2021.

[65] N. Kasi and M. Kakudo, *X-Ray Diffraction by Macromolecules*. Berlin: Kodansha Ltd. and Springer, 2005, ch. 4.1: The Bragg Diffraction Condition.

[66] E. EKNES, J. G. BEN, J. WALKER and K. MARSHALL, *Structural origins of barocaloric properties in hybrid plastic crystals*, en, 2025. DOI: 10.15151/ESRF-ES-753367664. [Online]. Available: https://doi.esrf.fr/10.15151/ESRF-ES-753367664.

[67] N. Kasi and M. Kakudo, *X-Ray Diffraction by Macromolecules*. Berlin: Kodansha Ltd. and Springer, 2005, ch. 8.5.1: Qualitative identification using poly crystal diffraction data (unoriented X-ray diagrams).

[68] N. Kasi and M. Kakudo, *X-Ray Diffraction by Macromolecules*. Berlin: Kodansha Ltd. and Springer, 2005, ch. 8.7.1: Measurement of crystallinity.

[69] J. William D. Callister and R. David G., *Materials Science and Engineering SI Version*. China: John Wiley & Sons Ltd, 2015, ch. 17.6: Heat Treatment of Steels.

[70] J. William D. Callister and R. David G., *Materials Science and Engineering SI Version*. China: John Wiley & Sons Ltd, 2015, ch. 12.4: Metastable Versus Equilibrium States.

[71] D. H. Aue, H. M. Webb and M. T. Bowers, 'A thermodynamic analysis of solvation effects on the basicities of alkylamines. an electrostatic analysis of substituent effects', *Journal of the American Chemical Society*, vol. 98, no. 2, pp. 318–329, 1976. DOI: 10.1021/ja00418a002.

[72] N. Kasi and M. Kakudo, *X-Ray Diffraction by Macromolecules*. Berlin: Kodansha Ltd. and Springer, 2005, ch. 2.8: Scattering of X-rays by Amorphous Solids.

[73] N. Kasi and M. Kakudo, *X-Ray Diffraction by Macromolecules*. Berlin: Kodansha Ltd. and Springer, 2005, ch. 2.9: Scattering of X-rays by Crystals.

Appendix

A Individual diffractograms including Rietveld refinement

The individual diffractogram of major diffraction lines for each material of the $TEA_xTBA_{1-x}FeBrCl_3$ system. The observed data, calculated fit from Rietveld refinement, difference between observed and calculated data, and hkl-ticks for the $P6_3mc$ and $Pnna$ phase are presented in Figures A.1-A.9.
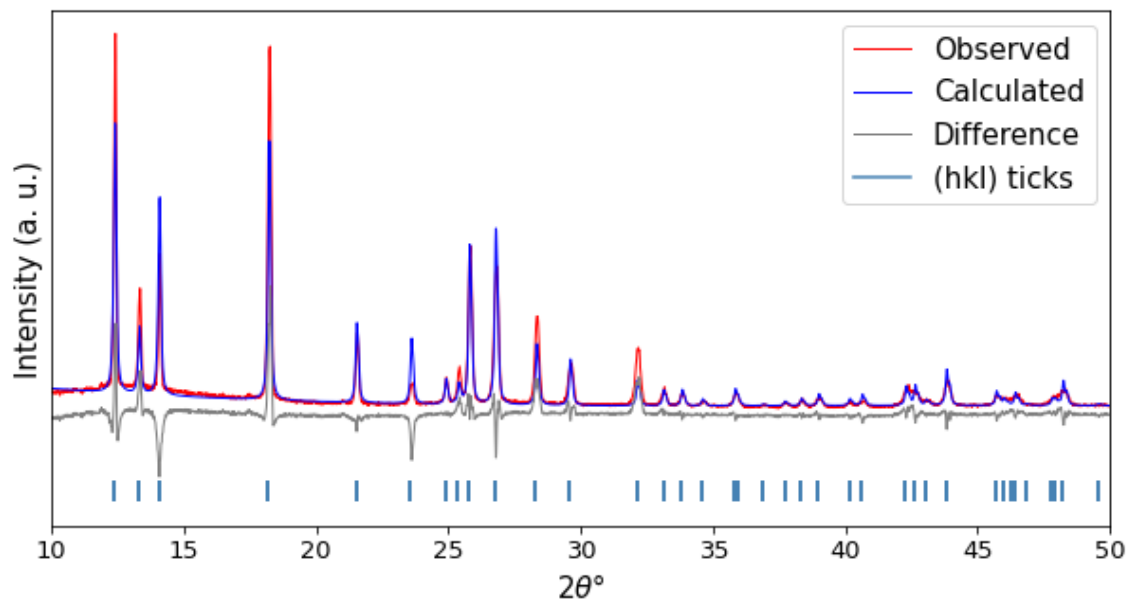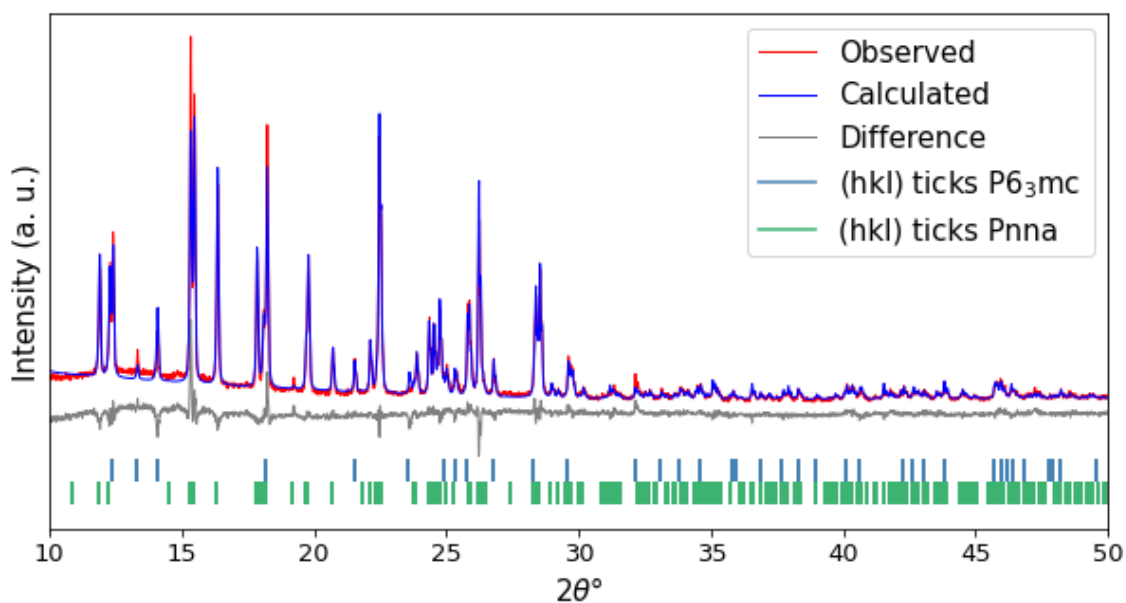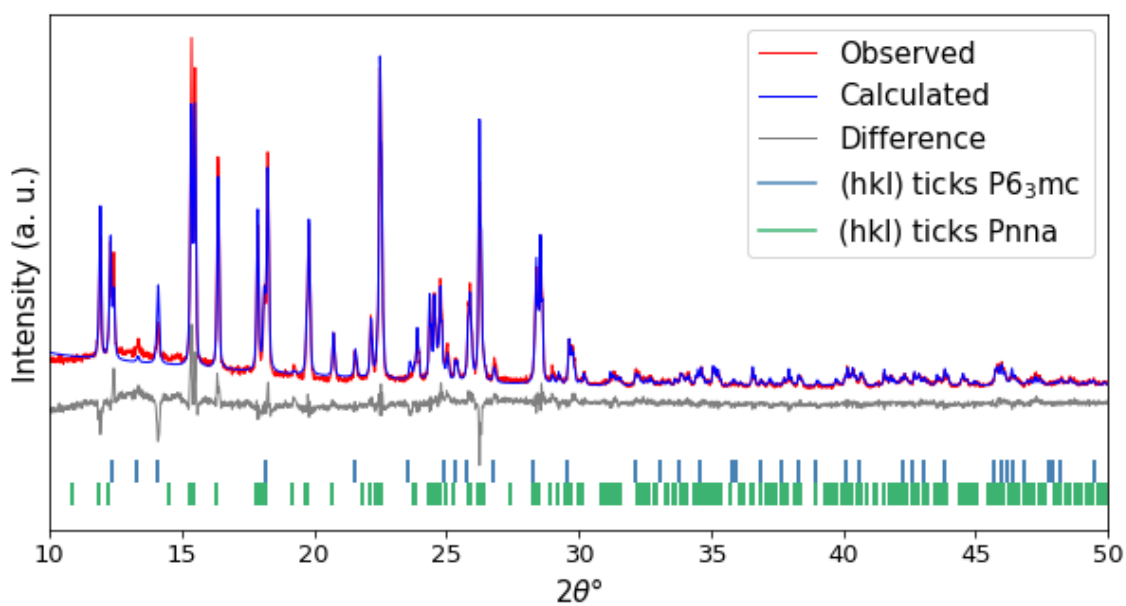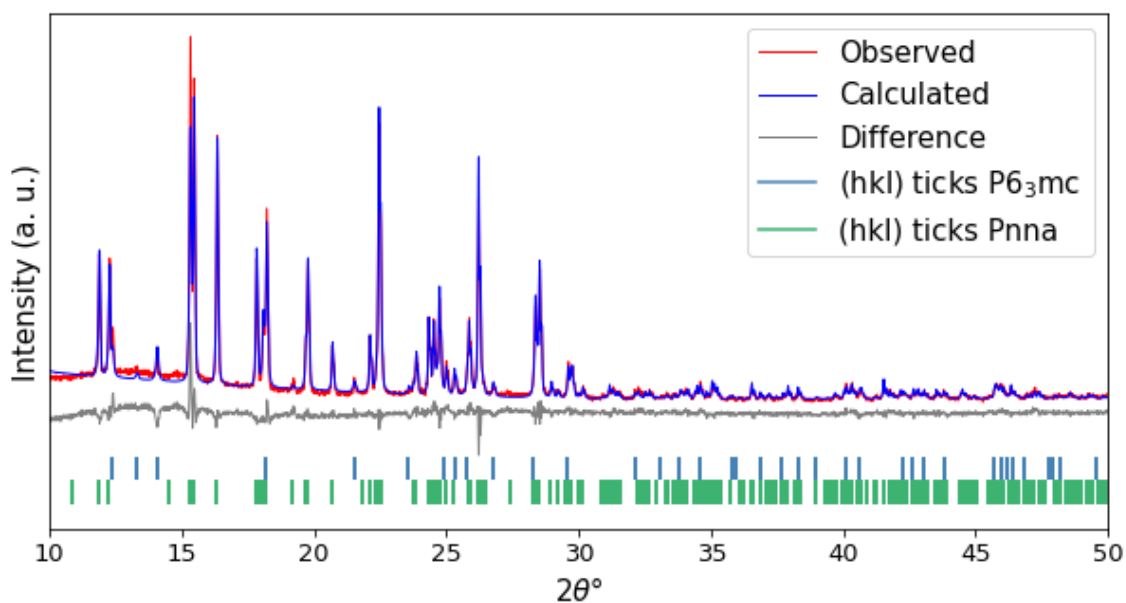

Figure A.1: X-ray diffractogram of C-TEA crystals showing the observed data from XRD, calculated fit from Rietveld refinement, difference between observed and calculated data, and hkl-ticks for the $P6_3mc$ phase.
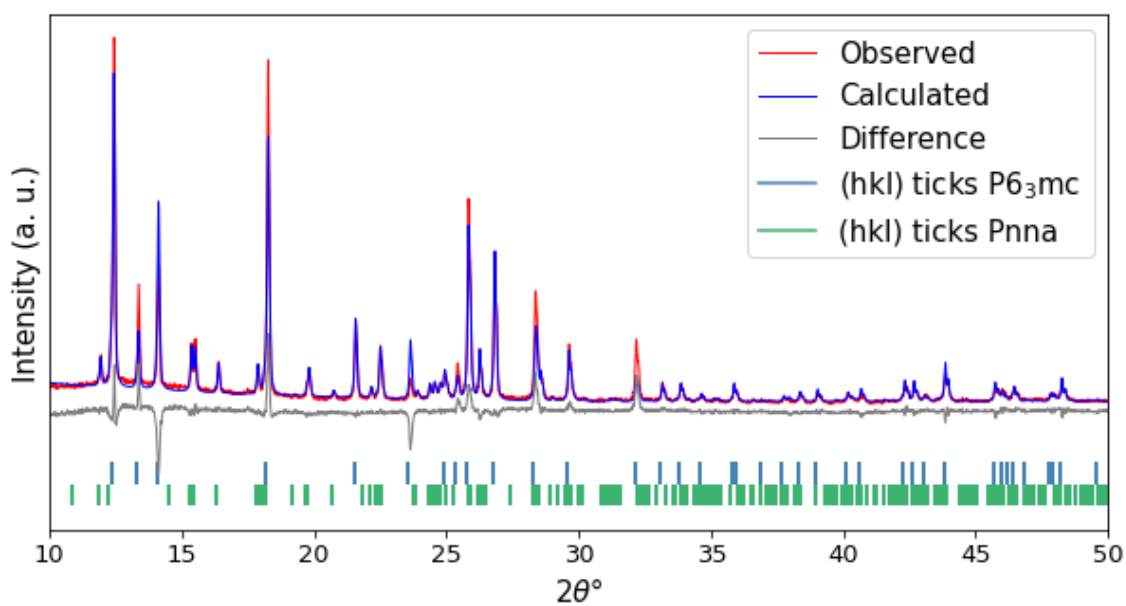
Figure A.2: X-ray diffractogram of C2-75 crystals showing the observed data from XRD, calculated fit from Rietveld refinement, difference between observed and calculated data, and hkl-ticks for the $P6_3mc$ and $Pnna$ phase.
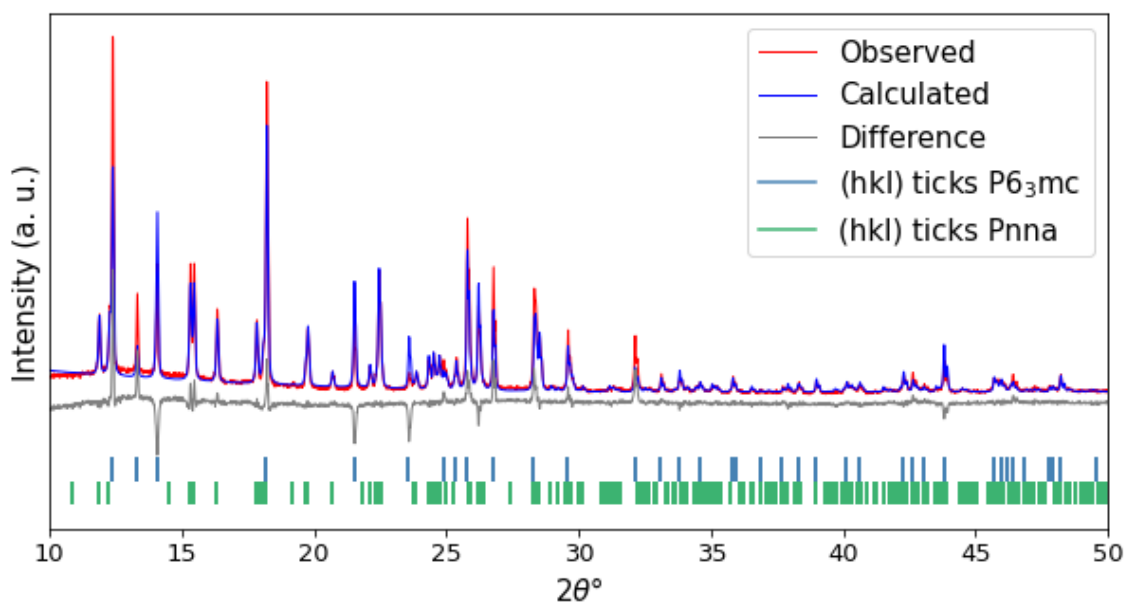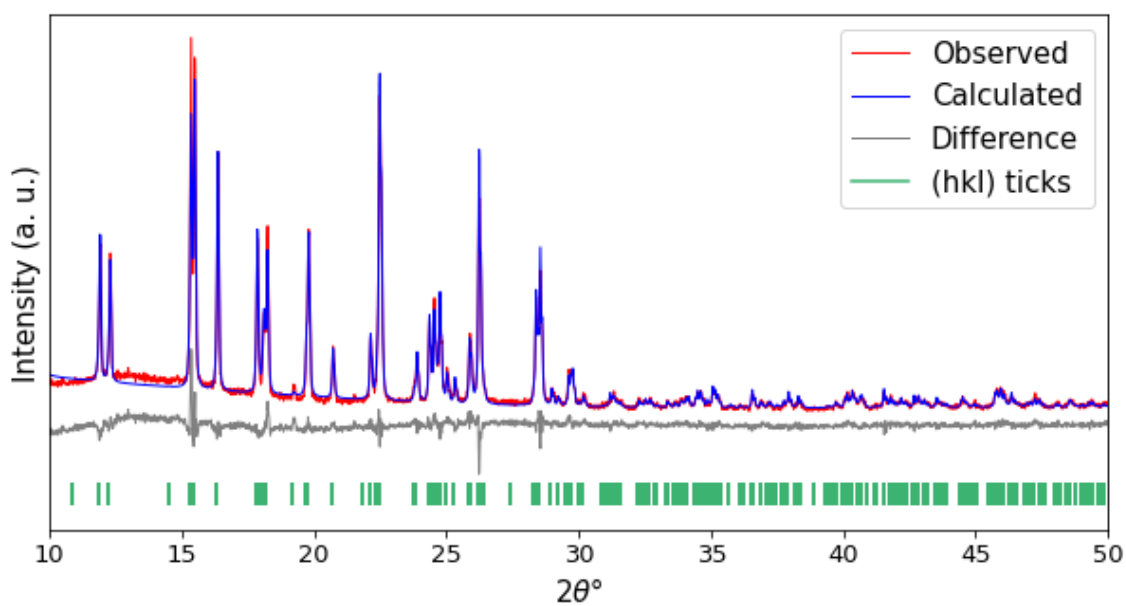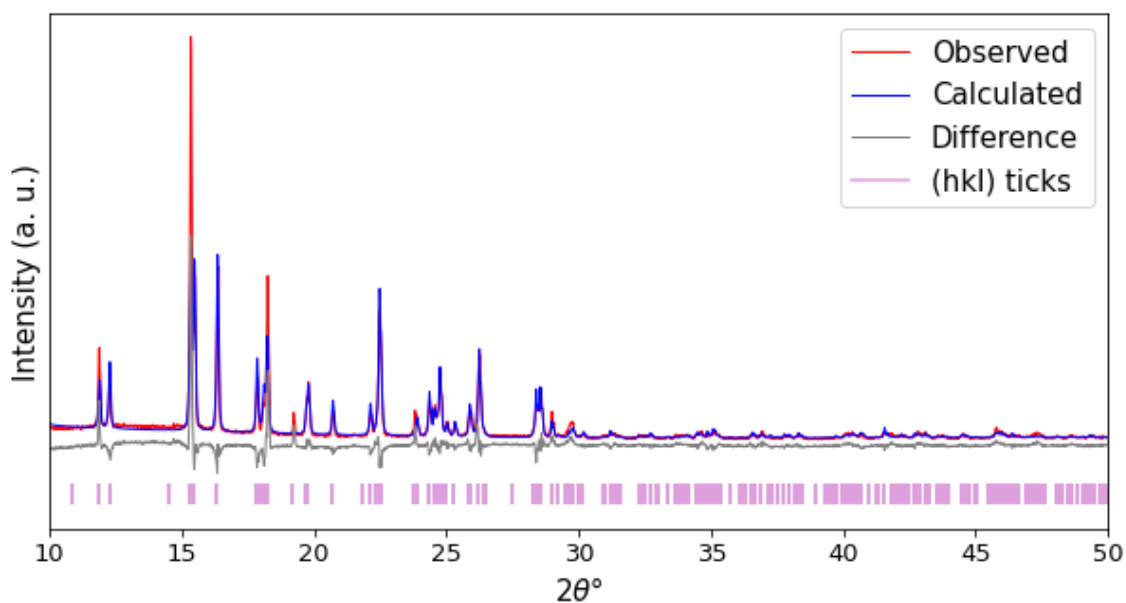

Figure A.3: X-ray diffractogram of C2-50 crystals showing the observed data from XRD, calculated fit from Rietveld refinement, difference between observed and calculated data, and hkl-ticks for the $P6_3mc$ and $Pnna$ phase.
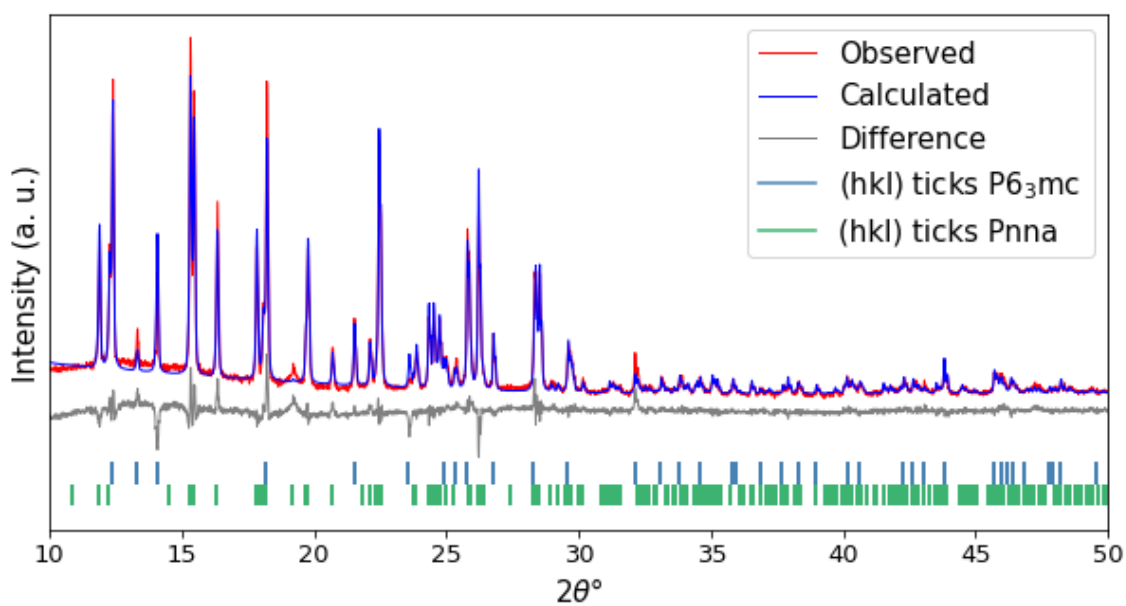
Figure A.4: X-ray diffractogram of C2-25 crystals showing the observed data from XRD, calculated fit from Rietveld refinement, difference between observed and calculated data, and hkl-ticks for the $P6_3mc$ and $Pnna$ phase.

Figure A.5: X-ray diffractogram of C2-15 crystals showing the observed data from XRD, calculated fit from Rietveld refinement, difference between observed and calculated data, and hkl-ticks for the $P6_3mc$ and $Pnna$ phase.

Figure A.6: X-ray diffractogram of C2-10 crystals showing the observed data from XRD, calculated fit from Rietveld refinement, difference between observed and calculated data, and hkl-ticks for the $P6_3mc$ and $Pnna$ phase.

Figure A.7: X-ray diffractogram of C2-5 crystals showing the observed data from XRD, calculated fit from Rietveld refinement, difference between observed and calculated data, and hkl-ticks for the $P6_3mc$ and $Pnna$ phase.

Figure A.8: X-ray diffractogram of C2-TBA crystals showing the observed data from XRD, calculated fit from Rietveld refinement, difference between observed and calculated data, and hkl-ticks for the *Pnna* phase.

Figure A.9: X-ray diffractogram of C-TBA crystals showing the observed data from XRD, calculated fit from Rietveld refinement, difference between observed and calculated data, and hkl-ticks for the *Pnna* phase.

B   Lattice parameters from Rietveld refinement

Table B.1 shows the lattice parameters of the $P6_3mc$ and $Pnna$ phases with corresponding errors from Rietveld refinement of $TEA_xTBA_{1-x}FeBrCl_3$ compounds with x = 0, 0.05, 0.1, 0.15, 0.25, 0.5, 0.75, and 1.

Table B.1: Lattice parameters of the $P6_3mc$ and $Pnna$ phases with corresponding errors from Rietveld refinement of $TEA_xTBA_{1-x}FeBrCl_3$ compounds with x = 0, 0.05, 0.1, 0.15, 0.25, 0.5, 0.75, and 1. C2 indicates that the sample was annealed at 220 °C. A parenthesis is given around the first uncertain digit in TOPAS [61, 62].

Sample	a [Å]	b [Å]	c [Å]
		$P6_3mc$ phase	
C-TEA	8.2598(4) ± 0.0004306	8.2598(4) ± 0.0004306	13.3166(7) ± 0.0006963
C2-75	8.2629(2) ± 0.0002492	8.2629(2) ± 0.0002492	13.3195(4) ± 0.0004403
C2-50	8.2626(2) ± 0.0002445	8.2626(2) ± 0.0002445	13.3209(6) ± 0.0005653
C2-25	8.2614(2) ± 0.0002142	8.2614(2) ± 0.0002142	13.3182(5) ± 0.0005468
C2-15	8.2624(3) ± 0.0002960	8.2624(3) ± 0.0002960	13.3207(7) ± 0.0007021
C2-10	8.2622(5) ± 0.0004964	8.2622(5) ± 0.0004964	13.3223(16) ± 0.0015593
C2-5	8.2615(8) ± 0.0008114	8.2615(8) ± 0.0008114	13.3216(18) ± 0.0018419
		$Pnna$ phase	
C2-75	18.494(2) ± 0.0023753	11.5851(11) ± 0.0011319	11.4778(11) ± 0.0011362
C2-50	18.4976(14) ± 0.0014101	11.5826(7) ± 0.0007222	11.4767(7) ± 0.0007138
C2-25	18.4970(7) ± 0.0007088	11.5797(4) ± 0.0003840	11.4756(4) ± 0.0003658
C2-15	18.4964(6) ± 0.0005755	11.5798(3) ± 0.0003491	11.4765(4) ± 0.0003514
C2-10	18.4969(7) ± 0.0007248	11.5804(4) ± 0.0004390	11.4771(4) ± 0.0004080
C2-5	18.4947(5) ± 0.0004984	11.5812(3) ± 0.0003088	11.4756(3) ± 0.0003018
C2-TBA	18.5021(6) ± 0.0005934	11.5828(4) ± 0.0003585	11.4782(4) ± 0.0003577
C-TBA	18.4838(11) ± 0.0010501	11.5708(7) ± 0.0006512	11.4638(7) ± 0.0007226

C Individual DSC results

Individual DSC results of the second thermal cycle between 65 and 175 °C for sample C2-TBA, C2-5, C2-10, C2-15, C2-25, C2-50, and C2-75 is given in Figures C.1-C.7. Each peak presents a phase transition, and the onset temperature for these transitions is marked with a dashed, grey line. The corresponding temperature is noted in red on heating and in blue on cooling.
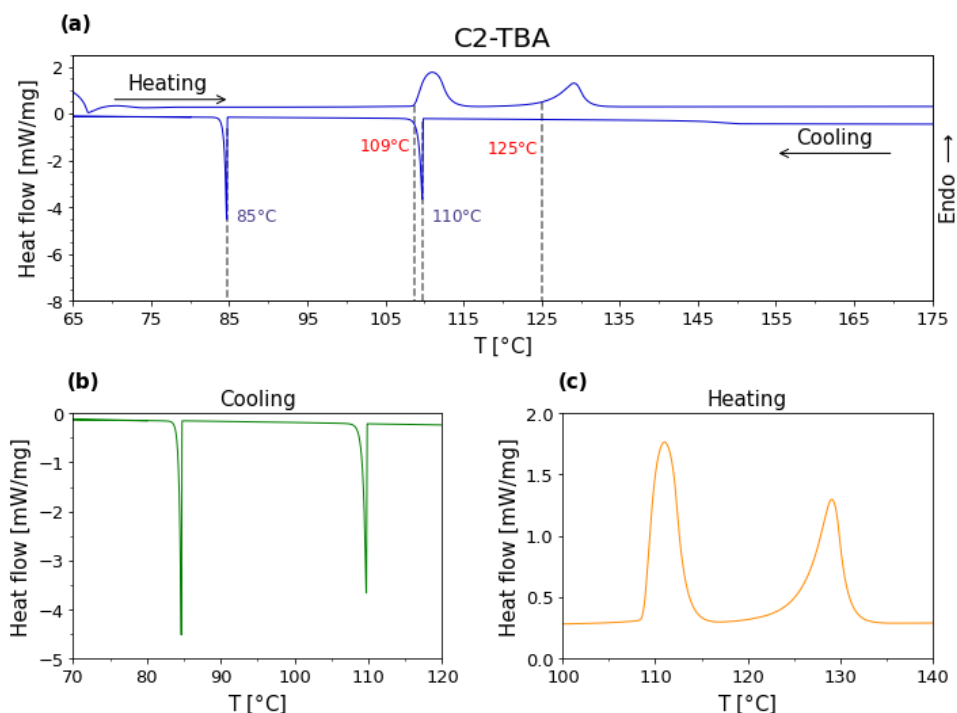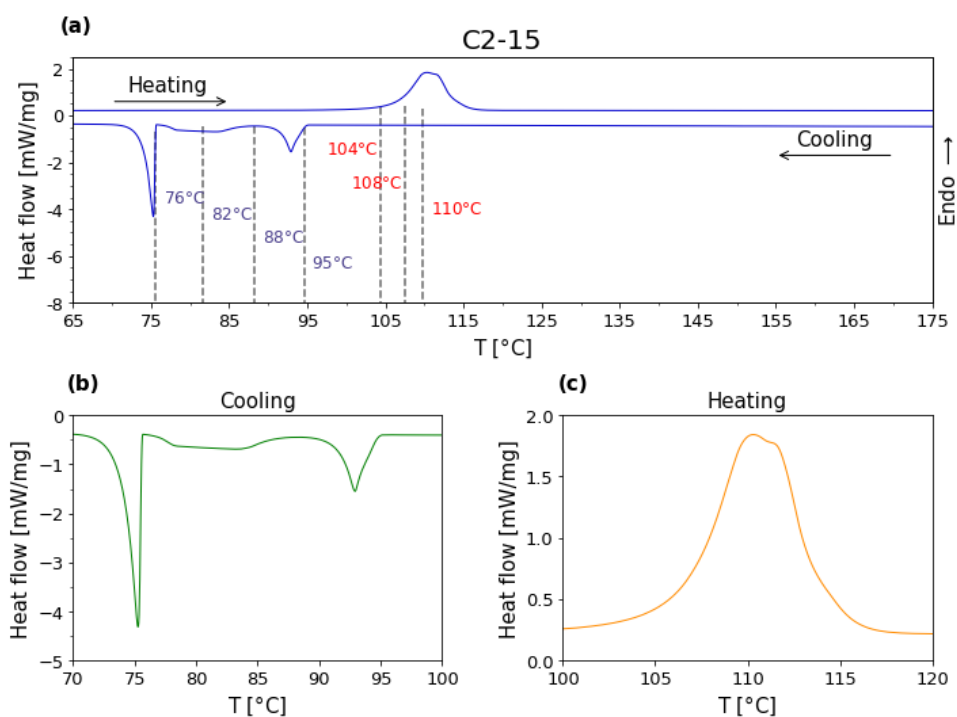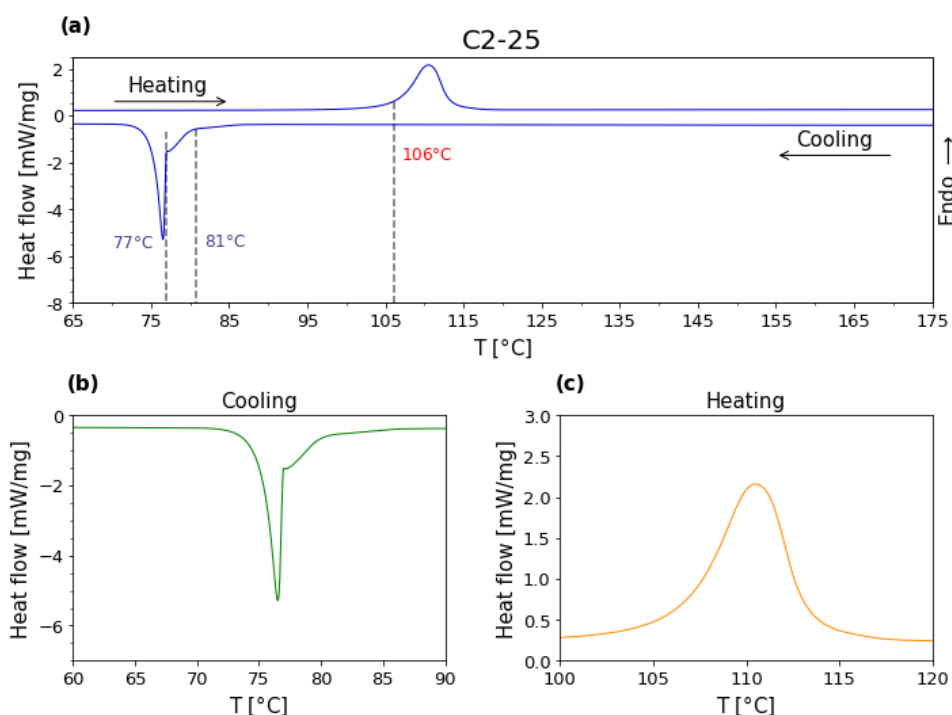

Figure C.1: **(a)** DSC measurement of C2-TBA crystals from 65 to 175 °C. The dashed, grey lines mark the onset temperature for the phase transition on heating and cooling. The temperatures are noted in red on heating and in blue on cooling. The results on cooling are not accurate, as the cooling rate was not controlled for this sample. The uneven line at the beginning of the heating, and the bump observed on cooling, are both due to this uncontrolled cooling. **(b)** Peaks indicating phase transitions on cooling. **(c)** Peaks indicating phase transitions on heating
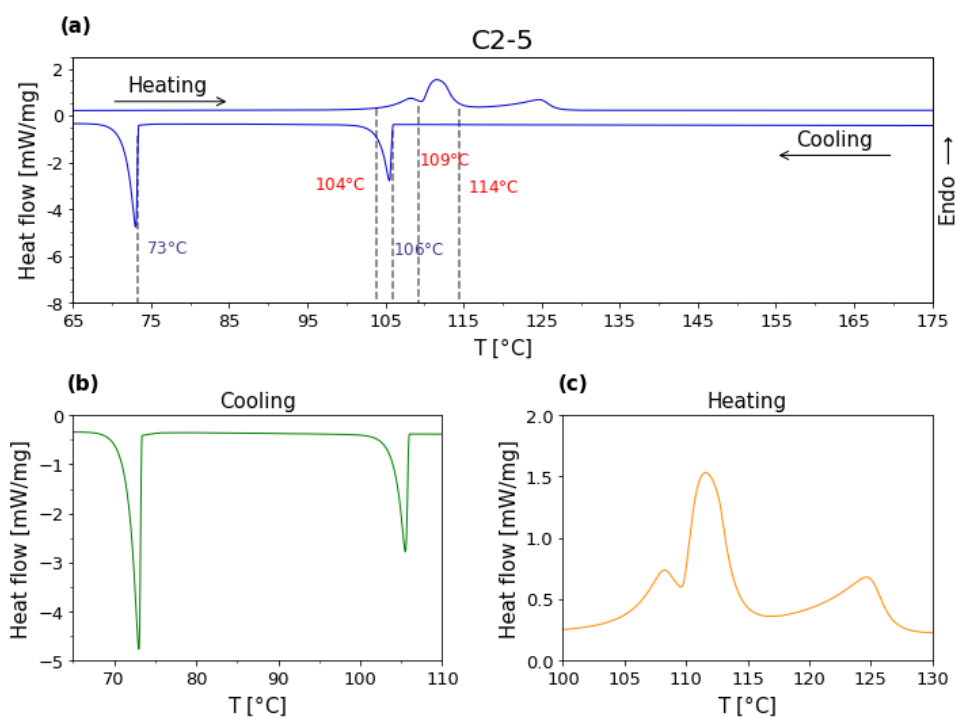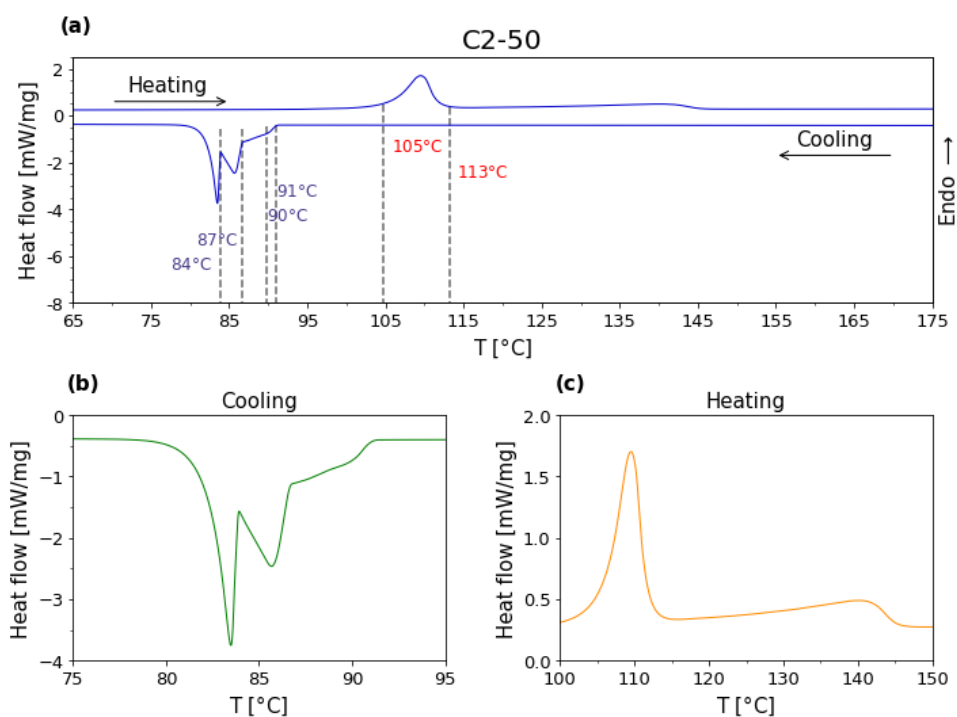
Figure C.2: **(a)** DSC measurement of C2-5 crystals from 65 to 175 °C. The dashed, grey lines mark the onset temperature for the phase transition on heating and cooling. The temperatures are noted in red on heating and in blue on cooling. **(b)** Peaks indicating phase transitions on cooling. **(c)** Peaks indicating phase transitions on heating
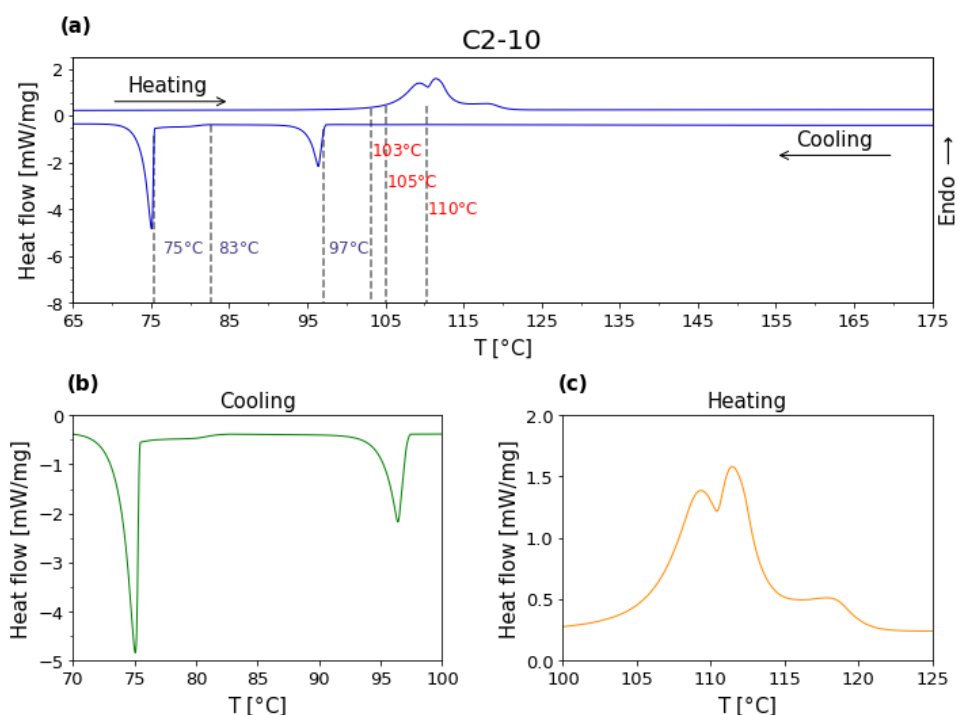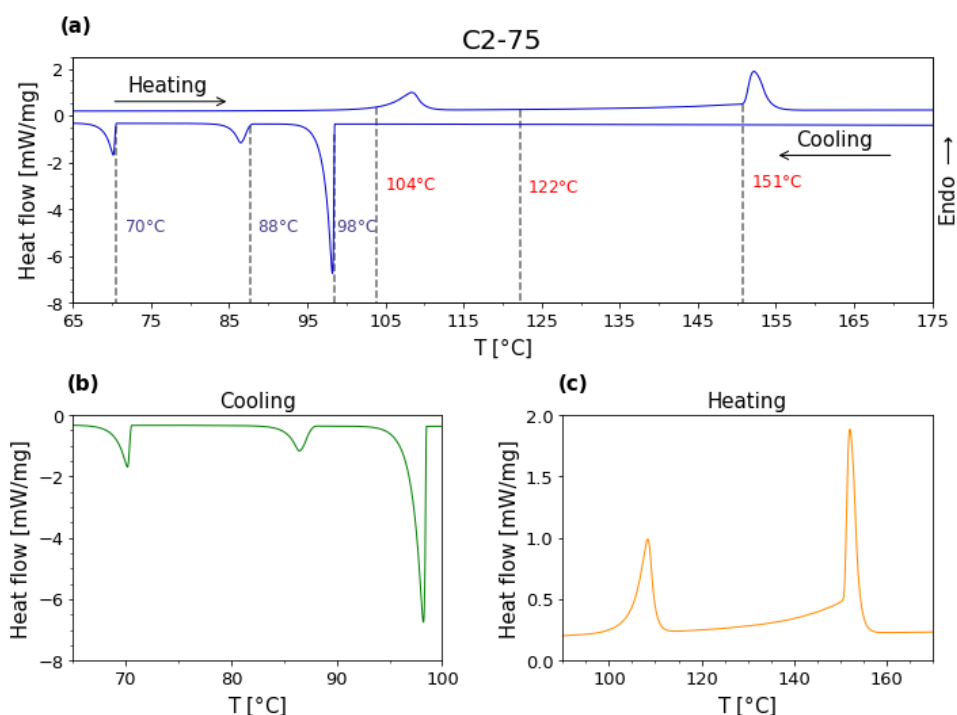

Figure C.3: **(a)** DSC measurement of C2-10 crystals from 65 to 175 °C. The dashed, grey lines mark the onset temperature for the phase transition on heating and cooling. The temperatures are noted in red on heating and in blue on cooling. **(b)** Peaks indicating phase transitions on cooling. **(c)** Peaks indicating phase transitions on heating

Figure C.4: **(a)** DSC measurement of C2-15 crystals from 65 to 175 °C. The dashed, grey lines mark the onset temperature for the phase transition on heating and cooling. The temperatures are noted in red on heating and in blue on cooling. **(b)** Peaks indicating phase transitions on cooling. **(c)** Peaks indicating phase transitions on heating

Figure C.5: **(a)** DSC measurement of C2-25 crystals from 65 to 175 °C. The dashed, grey lines mark the onset temperature for the phase transition on heating and cooling. The temperatures are noted in red on heating and in blue on cooling. **(b)** Peaks indicating phase transitions on cooling. **(c)** Peaks indicating phase transitions on heating

Figure C.6: **(a)** DSC measurement of C2-50 crystals from 65 to 175 °C. The dashed, grey lines mark the onset temperature for the phase transition on heating and cooling. The temperatures are noted in red on heating and in blue on cooling. **(b)** Peaks indicating phase transitions on cooling. **(c)** Peaks indicating phase transitions on heating

Figure C.7: **(a)** DSC measurement of C2-75 crystals from 65 to 175 °C. The dashed, grey lines mark the onset temperature for the phase transition on heating and cooling. The temperatures are noted in red on heating and in blue on cooling. **(b)** Peaks indicating phase transitions on cooling. **(c)** Peaks indicating phase transitions on heating

D Error estimates for DSC-values

There are four main sources of error related to the values of the enthalpy, entropy, and FWHM in Table 4.4 and 4.5. These are the onset and end temperatures, the shape of the peaks obtained from deconvolution, the numerical methods used to calculate integrals, and the sampling frequency of the DSC instrument. The errors for the onset and end temperatures in Table 4.4 and 4.5 were estimated directly from the DSC curves on heating and cooling in Figure 4.13 and 4.14. The sharper or broader the peak is, the smaller or larger the error of the onset and end temperatures become, respectively. The errors of the enthalpy and entropy displayed in the tables are derived from the errors in the onset and end temperatures. To calculate the enthalpy error, the maximum and minimum values of the enthalpy were calculated based on the errors in the onset and end temperatures (i.e. the maximum and minimum enthalpy allowed by the error in the onset and end temperatures). Hence, the sharpest peaks (small FWMH values), which are particularly prevalent during cooling, have large errors because even small changes in the onset and end temperatures will affect the enthalpy significantly. The final enthalpy error is given as the average difference between the enthalpy value, and the maximum and minimum enthalpy,

$$E_{\Delta H} = \frac{|\Delta H - \Delta H_{max}| + |\Delta H - \Delta H_{min}|}{2}.$$

(5)

Similarly, the final entropy error is given as the average difference between the entropy value, and the maximum and minimum entropy, which are based on the maximum and minimum enthalpy and onset temperatures,

$$E_{\Delta S} = \frac{|\Delta S - \Delta S_{max}| + |\Delta S - \Delta S_{min}|}{2} = \frac{|\Delta S - \frac{\Delta H_{max}}{T_{o,\,min}}| + |\Delta S - \frac{\Delta H_{min}}{T_{o,\,max}}|}{2}.$$

(6)

One can assume that the error is larger for peaks that are estimated as single peaks via deconvolution, which are marked with * in Table 4.4 and 4.5. However, this deconvolution error is difficult to quantify and is therefore omitted. The trapezoidal rule was used to calculate the enthalpy. This method has an error of $O(h^2)$, where h is the stepsize, and is thus negligible. The error in the FWHM values does not depend on the errors in the onset and end temperatures. Instead, the FWHM error is based on the error due to the sampling frequency. By moving the FWHM one data point up and one data point down, one slightly smaller and one slightly larger FWHM value is found. The final FWHM error is given as the average difference between the FWHM value, and the smaller and larger FWHM values,

$$E_{FWHM} = \frac{|FWHM - FWHM_{above}| + |FWHM - FWHM_{below}|}{2}.$$

(7)

E   Deconvolution of overlapping peaks in DSC data

An example of how the deconvolution of overlapping peaks in the DSC results was performed is shown in Figure E.1 for the C2-10 sample on heating. The three merged peaks were approximated into three single peaks using LIPRAS [63].
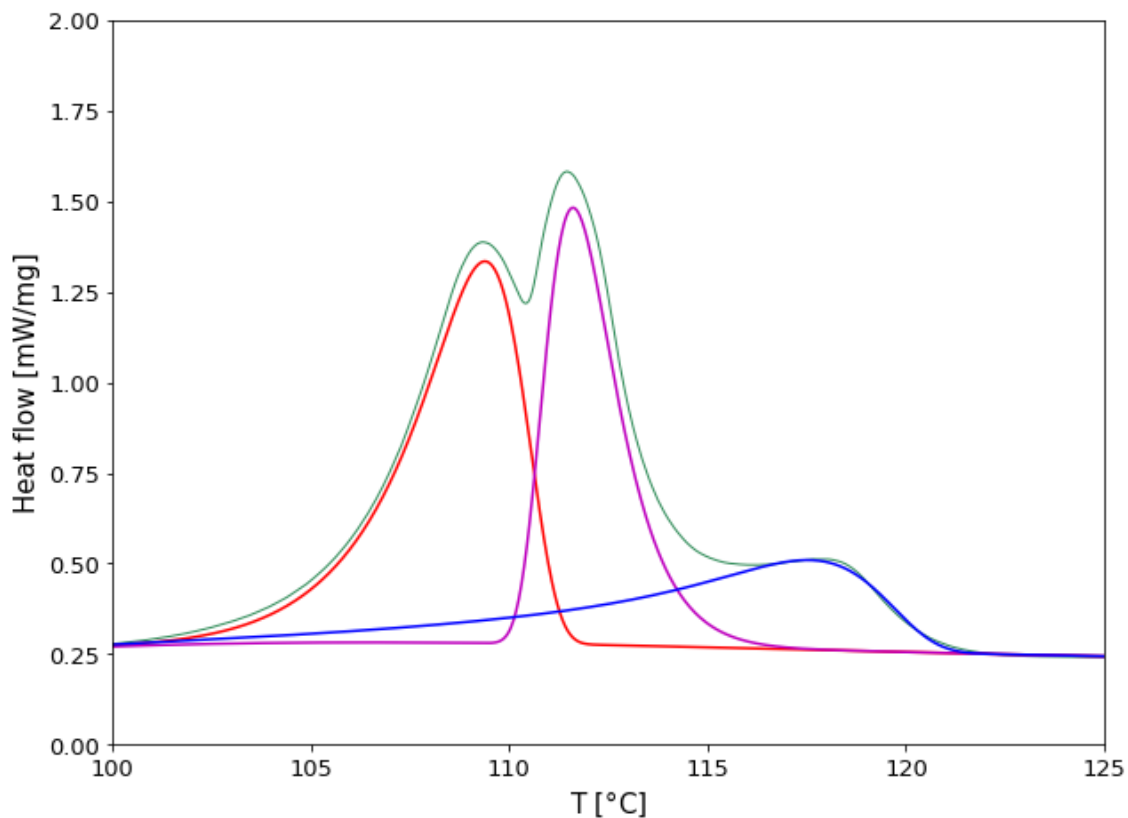

Figure E.1: Example of how overlapping peaks in the DSC results were approximated into single peaks using deconvolution in LIPRAS [63]. The data shown here are from the heating part of the second thermal cycle for the C2-10 sample.

F DSC results from three heating and cooling cycles

Figures F.1-F.6 show how the DSC results varied between the three heating and cooling cycles for sample C-TEA, C2-75, C2-25, C2-15, C2-5, and C-TBA.
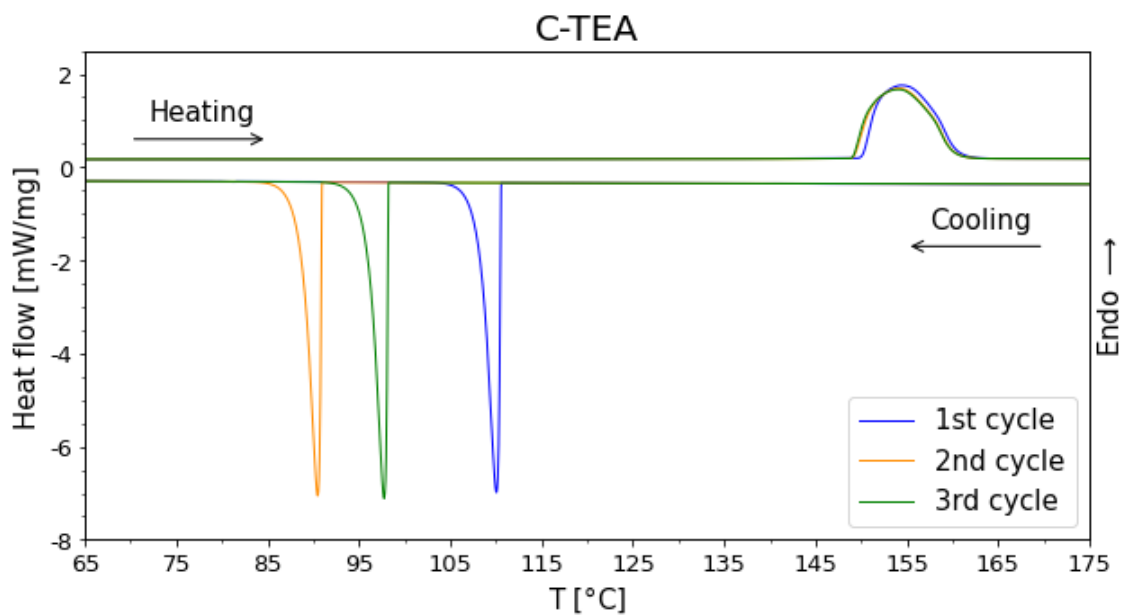
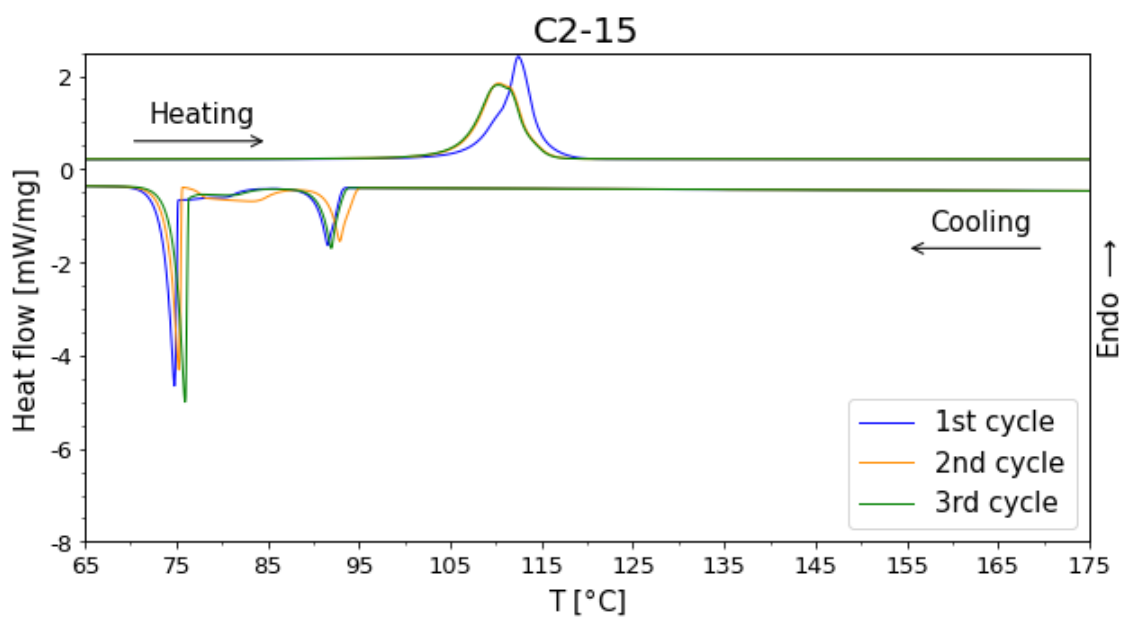Figure F.1: Heat flow as a function of temperature for three thermal cycles for the C-TEA sample.
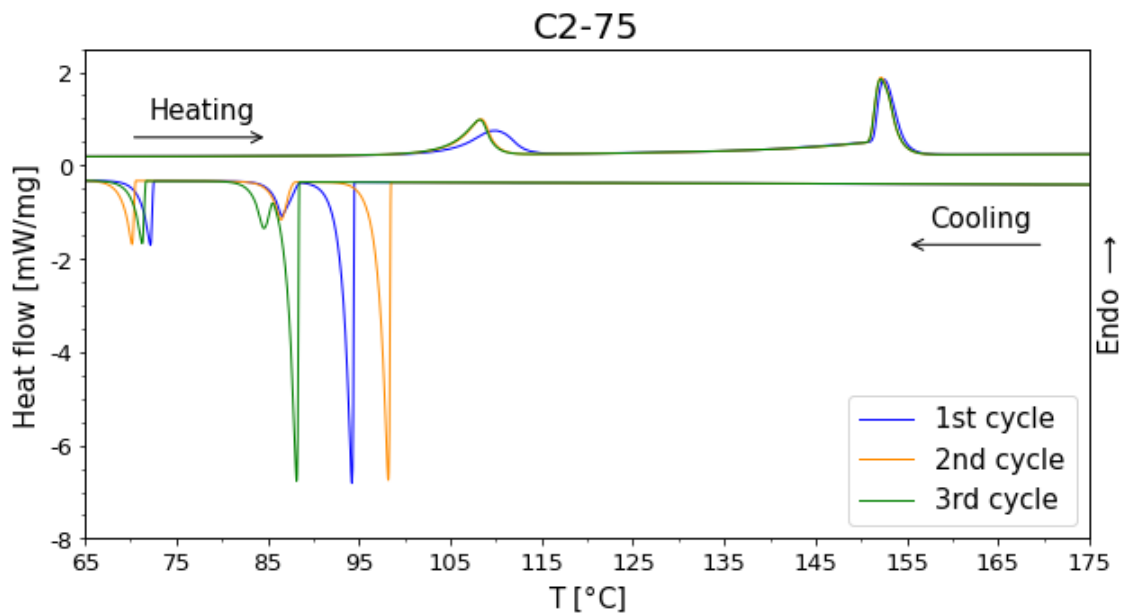
Figure F.2: Heat flow as a function of temperature for three thermal cycles for the C2-75 sample, which contains 75 mol% TEAFeBrCl$_3$.
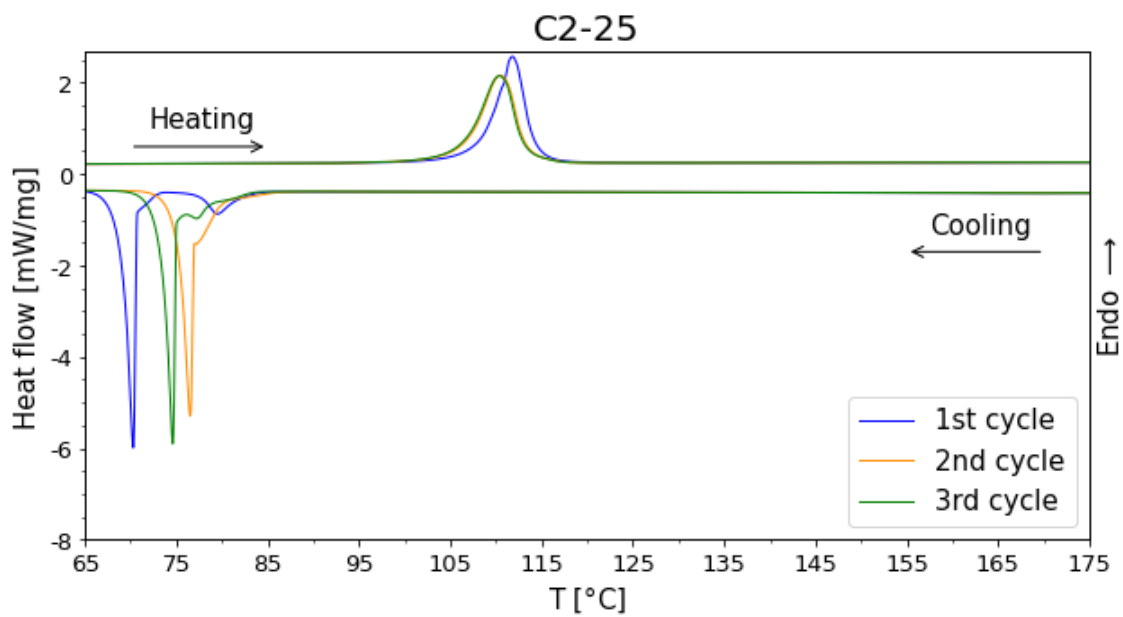
Figure F.3: Heat flow as a function of temperature for three thermal cycles for the C2-25 sample, which contains 25 mol% TEAFeBrCl$_3$.

Figure F.4: Heat flow as a function of temperature for three thermal cycles for the C2-15 sample, which contains 15 mol% TEAFeBrCl$_3$.
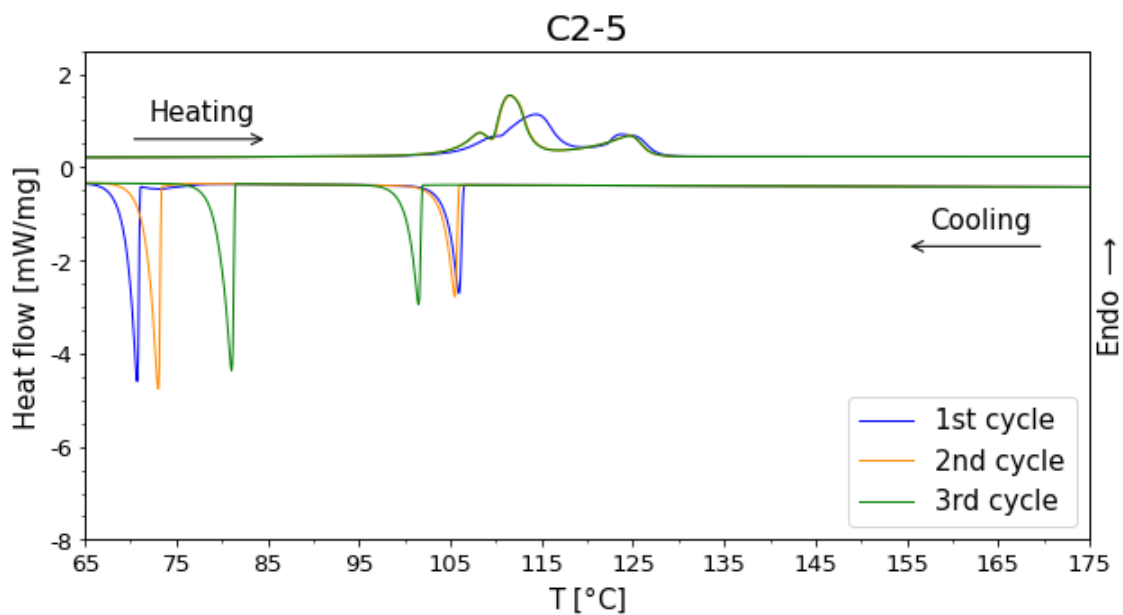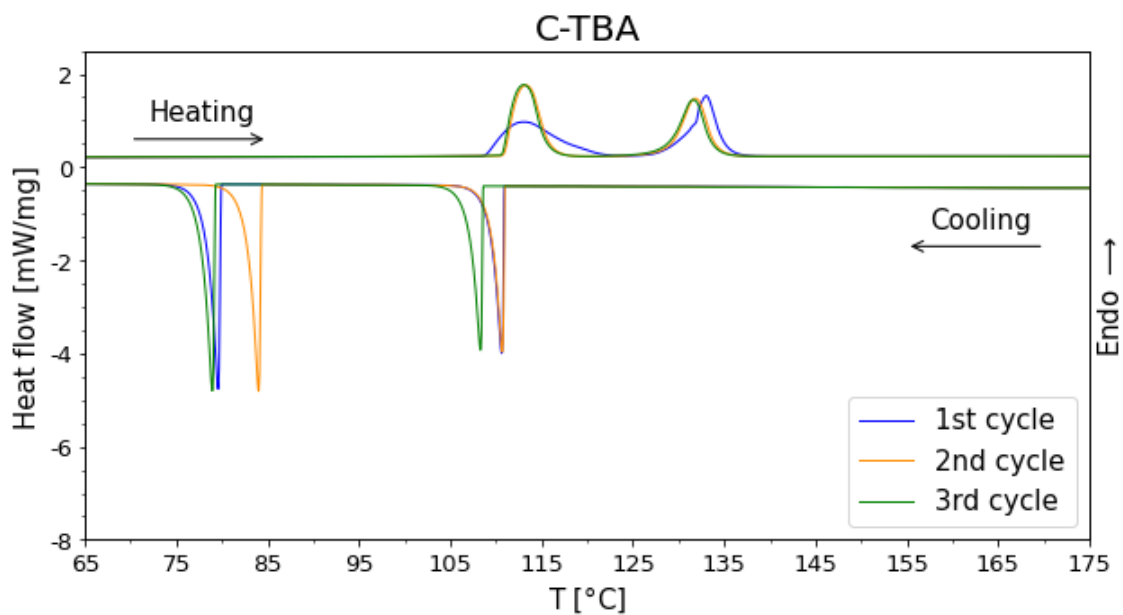
Figure F.5: Heat flow as a function of temperature for three thermal cycles for the C2-5 sample, which contains 5 mol% TEAFeBrCl$_3$.

Figure F.6: Heat flow as a function of temperature for three thermal cycles for the C-TBA sample.

G Comparison of XRD diffractograms to the diffractogram of C-TBA

Comparison between the normalised X-ray diffraction data set of C-TBA and other samples in the TBAFeBrCl$_3$-rich region. A difference in the background intensity between the annealed compounds and the as crystallised TBAFEBrCl$_3$ can be observed at lower 2θ-values, which may indicate decreased crystallinity in annealed samples. The results are shown in Figures G.1-G.4.
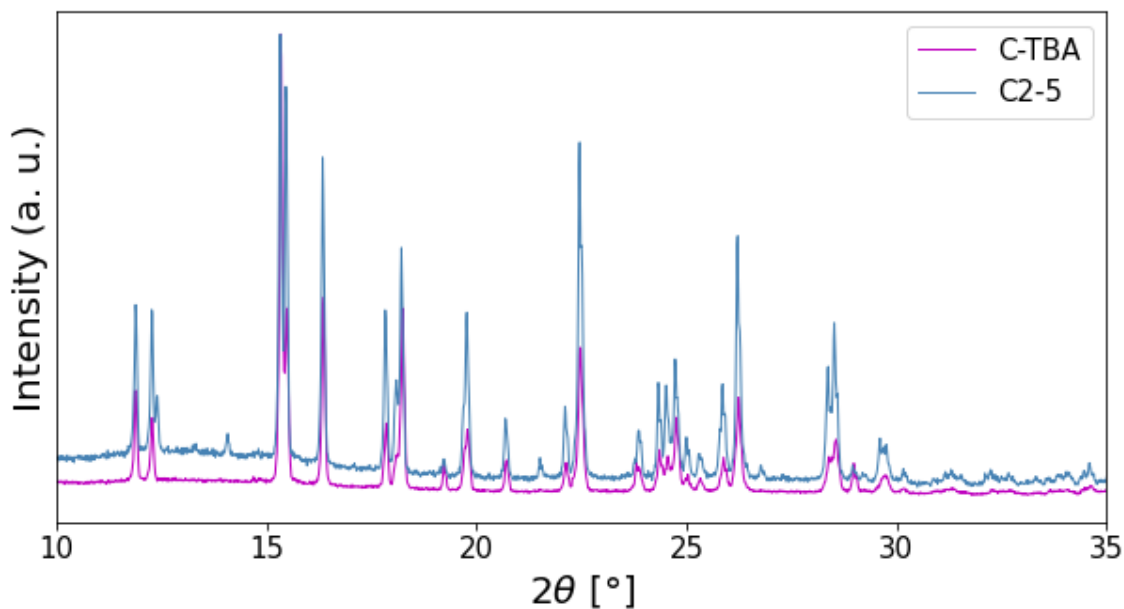

Figure G.1: X-ray diffractograms of C-TBA and C2-5. C2 indicates that the sample was annealed at 220 °C. Both diffractograms are normalised, giving relative intensities.
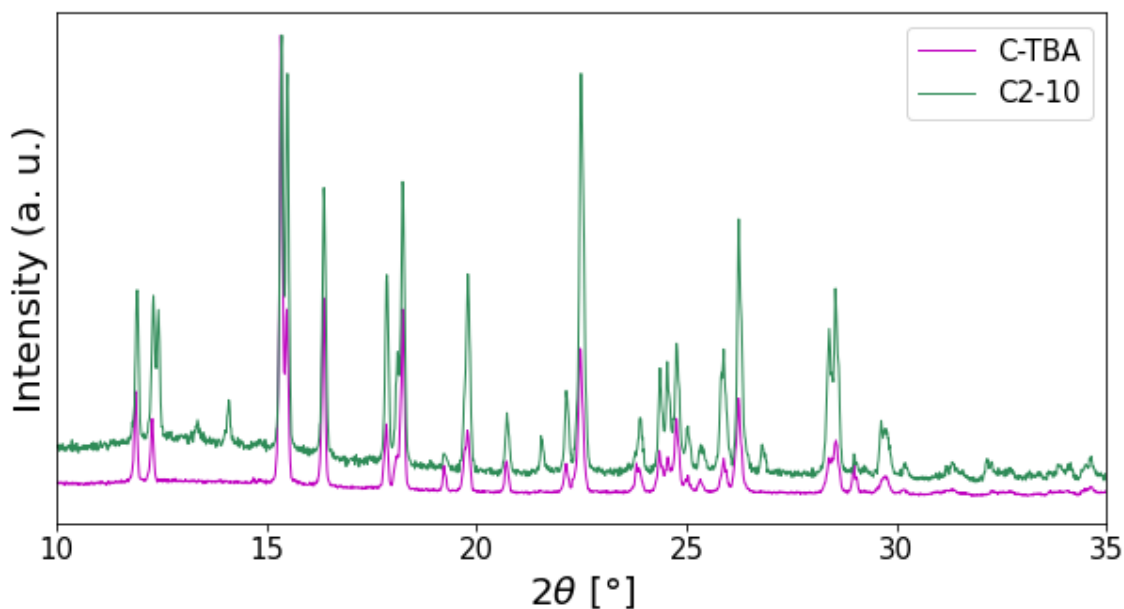

Figure G.2: X-ray diffractogram of C-TBA and C2-10. C2 indicates that the sample was annealed at 220 °C. Both diffractograms are normalised, giving relative intensities.
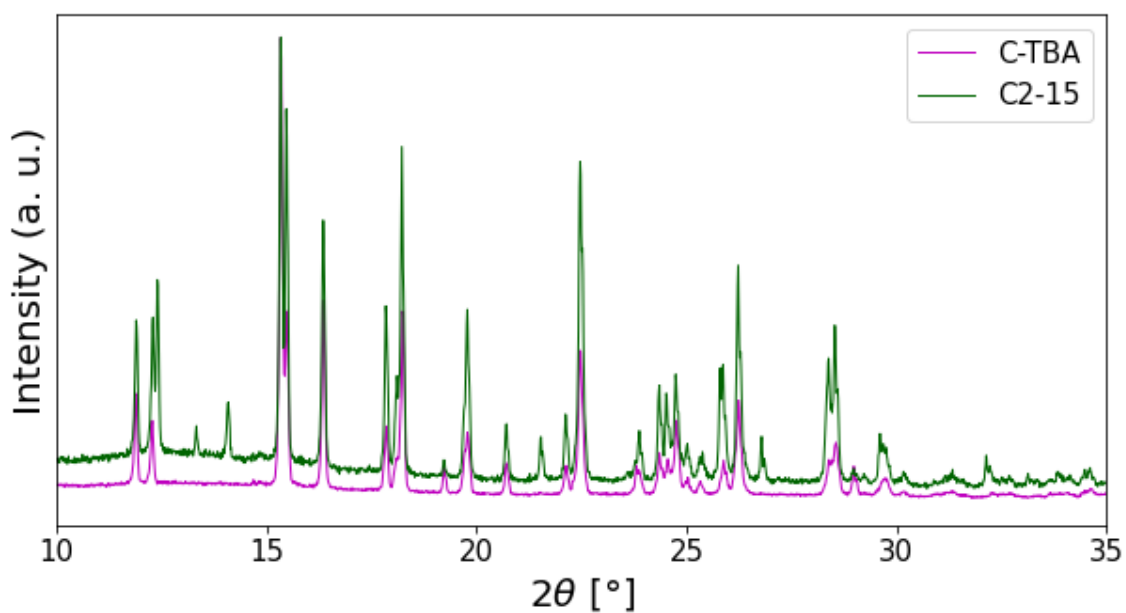
Figure G.3: X-ray diffractogram of C-TBA and C2-15. C2 indicates that the sample was annealed at 220 °C. Both diffractograms are normalised, giving relative intensities.
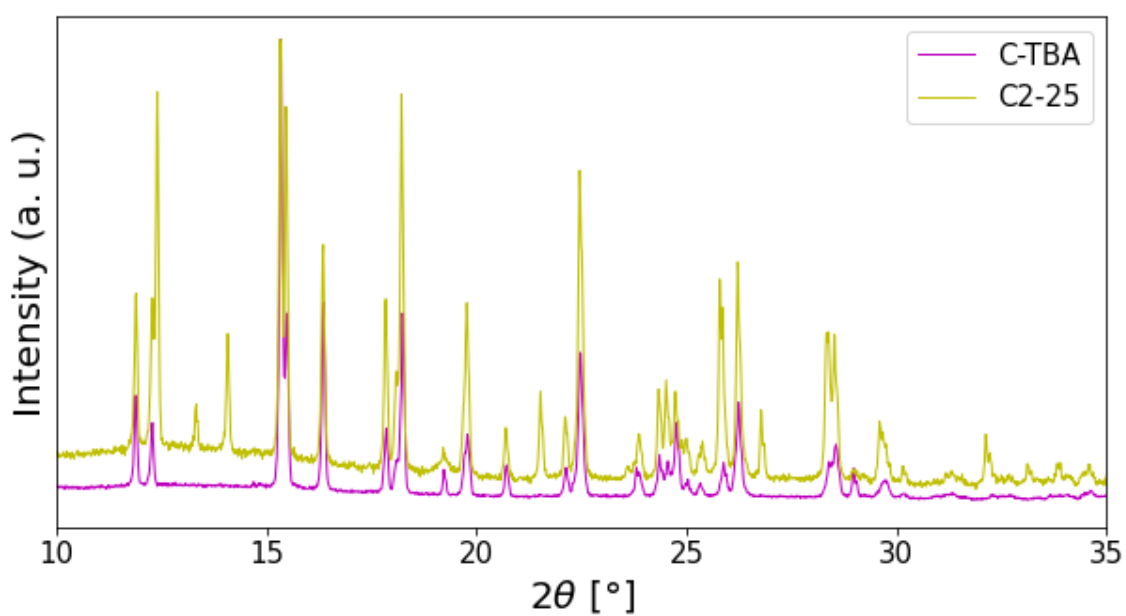

Figure G.4: X-ray diffractogram of C-TBA and C2-25 samples. C2 indicates that the sample was annealed at 220 °C. Both diffractograms are normalised, giving relative intensities.

H Synthesis of quincorine tetrachloroferrate(III)

Originally, this master's thesis aimed to synthesise and analyse quincorine tetrachloroferrate(III). However, the synthesis was not successful, as a gel resulted instead of crystals, making it difficult to analyse the material further. As the amount of the quincorine cation available was limited, multiple synthesis attempts were not possible, and a new aim was set for the master's thesis, which is treated in this report up until now. Here is a summary of the synthesis method that was tried out to make quincorine tetrachloroferrate(III), to ensure that this knowledge is available in the future if someone want to try another synthesis route.

Quincorine tetrachloroferrate(III), $[C_{10}H_{17}NO][FeCl_4]$, was synthesised from an evaporation crystallisation using the chemicals listed in Table H.1.

Table H.1: Chemicals used during the synthesis of quincorine tetrachloroferrate(III).

Chemical	Chemical formula	Manufacturer	Purity [%]
Iron(III) chloride hexahydrate	$FeCl_3 \cdot 6\,H_2O$	Sigma-Aldrich	99
Hydrochloric acid	HCl	Sigma-Aldrich	100
Deionized water	H_2O	NTNU	-
Quincorine	$C_{10}N_{17}NO$	UCT Prague	100

To synthesise the $FeCl_4^-$ anions, a solution of $FeCl_3 \cdot 6\,H_2O$ (0.6532 g), DI water (6 mL), and HCl (197 µL) was made and stirred with a magnetic stirrer for a few min to ensure complete dissolution and homogenisation of the solution. To avoid evaporation, the beaker was covered with parafilm. A solution of quincorine (approximately 400 mg) and DI water (2 mL) was made and stirred for a few min to ensure mixing of the emulsion. The solution with quincorine was added to the solution with $FeCl_4^-$, and mixed for a few min, before being transferred to a larger beaker for evaporation crystallisation of $[C_{10}H_{17}NO][FeCl_4]$. The solution was left in a fume hood, covered by aluminium foil with holes, until all the DI water had evaporated, which took about a week. A dark orange gel resulted.